10-24-2017

Model Reduction and Dynamic Adaptive Hybrid Integration for Efficient Combustion Simulations

Yang Gao
University of Connecticut - Storrs, yang.gao@uconn.edu

Model Reduction and Dynamic Adaptive Hybrid Integration for Efficient Combustion Simulations

Yang Gao, Ph.D.

University of Connecticut, 2017

Large-scale high-fidelity numerical simulation with detailed chemistry is an important approach to the study of combustion problems, which may involve turbulence and complex chemical reactions. However, detailed chemistry can involve a large number of species and reactions as well as severe chemical stiffness, resulting in high computational cost. This thesis presents a systematic study on reducing the computational cost of reacting flow simulations when detailed chemistry is involved. The effort includes reduction of chemical kinetic models and molecular diffusion, as well as development of advanced stiff chemistry solvers. First, a reduced kinetic model for ethylene/air with polycyclic aromatic hydrocarbons (PAHs) is developed for sooting flame simulations; reduced kinetic models are developed for *n*-dodecane as a jet fuel surrogate and for real jet fuels from detailed HyChem models by using a two-stage reduction method. Second, in addition to chemical kinetics, molecular diffusion is another important process in flames, and the mixture-averaged diffusion (MAD) model is frequently used in high-fidelity combustion simulations. However, the computational cost of the MAD model is typically a quadratic function of the number of species and can be high for large reaction models, necessitating the reduction of the MAD. Different approaches are therefore proposed to obtain small and accurate reduced models for the MAD. Third, in addition to model reduction, efficient stiff chemistry solvers can also substantially reduce the computation cost of combustion simulations. However, it is shown in the present study that the widely used operator splitting schemes can fail

in error control for flames where significant radical sources are present in the transport term. Therefore, an advanced stiff chemistry solver, namely the dynamic adaptive hybrid integration (AHI), is developed as a substitute of the operator-splitting schemes to achieve higher accuracy and computational efficiency for such flame simulations.

Model Reduction and Dynamic Adaptive Hybrid Integration for Efficient Combustion Simulations

Yang Gao

B.E., Xi'an Jiaotong University, 2013

A Dissertation

Submitted in Partial Fulfillment of the

Requirements for the Degree of

Doctor of Philosophy

At the

University of Connecticut

2017

APPROVAL PAGE

Doctor of Philosophy Dissertation

Model Reduction and Dynamic Adaptive Hybrid Integration for Efficient Combustion Simulations

Presented by

Yang Gao, B.E.

Major Advisor _____
Dr. Tianfeng Lu

Associate Advisor _____
Dr. Baki M. Cetegen

Associate Advisor _____
Dr. Xinyu Zhao

University of Connecticut

2017

ACKNOWLEDGMENT

Every time when I saw the acknowledgment part of other people's thesis, I could feel how they earned the degree, and how they survived during their Ph.D. study. There is a saying, if you have never thought of quitting your Ph.D., you are not really experiencing the Ph.D. I think I'm lucky to reach this point without quitting my Ph.D. because of the support from many people. Now it is the time for me to write down my acknowledgments with mixed feelings, and many memories emerge in my mind. Actually, I don't like the idea of listing all the names in the acknowledgments. There are so many people I should thank, but a list must have an end and an order. Nevertheless, I'm truly grateful to them and must let them know.

First, I would like to express my sincerest gratitude to my advisor, Dr. Tianfeng Lu, for his generous support and invaluable guidance during my entire Ph.D. study at the University of Connecticut. I still remember the moment I knocked his office door five years ago to seek a research opportunity, and then he opened the door, the door of research, for me. Without his continuous support, I could not have reached this point, I could not have learned so much invaluable knowledge. I would never regret to have pursued my Ph.D. with him. Besides, I would also like to thank Dr. Baki M. Cetegen and Dr. Xinyu Zhao, for serving in my thesis committee and providing invaluable comments and help.

I would like to thank my colleagues Chao Xu, Yunchao Wu, Yufeng Liu, Cong Li, Mike Kuron, and Brian Magda for their discussions and help in research. I would especially thank my two seniors Dr. Zhaoyu Luo and Dr. Ruiqin Shan. Thanks so much for providing many helpful advices not only to my research but also to my career. Also, I'm especially grateful to Ji-Woong Park for the happy time spending with him both in the lab and in the life.

Beyond the lab and research, I would like to thank my friends at UCONN, Fengyu Qian, Yanping Gong, Chenglu Jin, Ruhua Jiang, Shanglong Zhang, *etc*. I'm really proud and lucky to have these excellent friends, thank them for making my life full of fun when I'm out of the lab. They let me know research is not the only thing in my life. Whenever I experience the lows and the highs, they always stay beside me, listen to me, and give me the sincerest help and support.

Most importantly, I would like to thank my family for their unconditional support, love, and encouragement. My family is always my anchor wherever I go, which makes me feel safe and fearless.

This research has been supported by the Air Force Office of Scientific Research, National Aeronautics and Space Administration, Federal Aviation Administration, and the King Abdullah University of Science and Technology.

List of Figures

Figure 2-1. Auto-ignition delays (left panels) and extinction temperature of PSR (right panels) for *n*-dodecane/air mixtures at equivalence ratios of 0.5, 1.0 and 1.5 and pressures of 1 and 10 atm, calculated with the detailed JetSurF 1.0 (solid lines), the lumped-detailed model (dashed lines) and the 24-species reduced model (symbols), respectively. 19

Figure 2-2. Normalized total mass fraction of C_4 species and larger, denoted as C_{4+}, as a function of temperature in auto-ignition and PSRs for *n*-dodecane/air mixtures at equivalence ratios of 0.5, 1.0 and 1.5, and pressures of 1 and 10 atm, calculated with the detailed JetSurF 1.0 (solid lines) and the 24-species reduced model (symbols). 21

Figure 2-3. Laminar flame speed as a function of equivalence ratio for *n*-dodecane/air mixtures at an initial temperature of 300 K and pressures of 1 and 10 atm. 21

Figure 2-4. Comparison of predicted results (lines) and experimentally measurements (symbols) for *n*-dodecane/air: (a) ignition delay at $\phi = 0.5$, p = 20 atm, (b) laminar flame speed as function of equivalence ratio at atmospheric pressure and freestream temperature of 403 K. 23

Figure 2-5. (a) Comparison of the maximum temperature $T\max$ in counterflow non-premixed flames as a function of the strain rate, calculated with the detailed, lumped-detailed and 24-species reduced models; (b) Normalized total mass fraction of C_{4+} species, and that of the primary fuel cracking products, including CH_4, C_2H_4 and C_3H_6, at three different strain rates as predicted by the detailed model. The flames are at atmospheric pressure and an inlet temperature of 300 K with the fuel jet comprised of 50% (mol) *n*-dodecane in N_2 and air at 300 K as the oxidizer jet. 24

Figure 2-6. (a) Comparison of maximum temperature $T\max$ in counterflow premixed flames as a function of the strain rate, calculated with the detailed, lumped-detailed and 24-species reduced models; (b) Normalized total mass fraction of C_{4+} species, and that of the primary fuel cracking

products, including CH_4, C_2H_4 and C_3H_6, at three different strain rates as predicted by the detailed model. The flames are at atmospheric pressure and an inlet temperature of 300 K with the twin jets composed of an *n*-dodecane/air mixture at ϕ = 0.7. 26

Figure 2-7. Ignition delays, PSR extinction and laminar flame speed for *n*-butane/air mixtures at equivalence ratios of ϕ = 0.6 - 0.9 and pressures of 1 and 5 atm, calculated with the detailed, skeletal, and reduced models. 28

Figure 2-8. (a) Initial temperature isocontour for the 2-D DNS of *n*-butane/air, and (b) location of the DNS case on the Borghi diagram (Ka = 250, Re_t = 1000), courtesy of Dr. S. Lyra. 30

Figure 2-9. Left panels: Isocontour of fuel mass fraction (red: fresh mixture, blue: hot products), and right panels: scatter plots of mass fractions of fuel and primary cracking products vs. temperature, for DNS of a turbulent premixed flame of *n*-butane/air at different time instances. The white isolines on the left panels show the flame zone identified using CEMA. The solid lines on the right panels are solutions from 1-D steady state premix flame with the same fresh mixture condition as that in the DNS. 32

Figure 3-1. Accumulative worst-case errors in the target parameters in sensitivity analysis as function of the number of retained species in the skeletal model for A2, C1 and C5, respectively. 37

Figure 3-2. Ignition delay (left panel) and temperature profiles of PSR (right panel) for stoichiometric mixtures at pressure of 0.5, 1, 5, and 30 atm for A2, C1, and C5, calculated with the detailed (solid lines), skeletal (dashed lines), and reduced (symbols) models, respectively. Similar agreement is observed for ϕ = 0.5 and 1.5.....40

Figure 3-3. Laminar flame speed as function of equivalence ratio at an initial temperature of 300 K and pressure of 0.5, 1, 5, and 30 atm for A2, C1, and C5, calculated with the detailed (solid lines), skeletal (dashed lines), and reduced (symbols) models, respectively. 41
Figure 3-4. Comparison of the maximum temperature T_{max} in counterflow non-premixed (left panel) and premixed flames (right panel) as function of the reciprocal strain rate, calculated with the detailed (solid lines) and reduced (symbols) models, respectively. 43
Figure 3-5. Ignition delay (left panel) and temperature profiles of PSR (right panel) for stoichiometric mixtures at pressure of 0.5, 1, 5, and 30 atm, calculated with the detailed (solid lines) and reduced (symbols) models, respectively. Similar agreement is observed for ϕ = 0.5 and 1.5. 44
Figure 3-6. Laminar flame speed as function of equivalence ratio at an inlet temperature of 300 K and pressure of 0.5, 1, 5, and 30 atm, calculated with the detailed (solid lines) and reduced (symbols) models, respectively. 45
Figure 3-7. Comparison of NO mole fractions in (a) PSR and (b) 1-D laminar premixed flame for A2/air mixture at stoichiometric condition for pressures of 0.5, 1, 5, and 30 atm. Solid lines: detailed HyChem model for A2 with the complete NO sub-model. Dashed lines: 45-species universal reduced model with NO. 46
Figure 3-8. Left panels: Temperature profiles of PSR for A2, C1, and C5 under the four conditions listed in Table 3-3, calculated with the detailed (solid lines) and fuel-specific reduced (symbols) models, respectively. Right panels: Important reactions for the LBO of PSR based on the BI values for the four conditions in Table 3-3 for A2, C1, and C5. 50
Figure 3-9. Temperature profiles of PSR as function of equivalence ratios for A2 with different residence time τ under the four conditions given in Table 3-3, calculated with the detailed (solid

lines) and fuel-specific reduced (symbols) models, respectively. Similar agreement is observed for C1 and C5. 51

Figure 3-10. Fuel sensitivities in auto-ignition (top panel), temperature profiles of PSR (middle panel), and laminar flame speed (bottom panel) for detailed (left panel, solid lines) and reduced (right panel, dashed lines), respectively. 54

Figure 3-11. Comparison of the maximum temperature T_{max} in counterflow non-premixed (top panel) and premixed flames (bottom panel) as function of the reciprocal strain rate, calculated with the detailed (left panel, solid lines) and reduced (right panel, dashed lines) models, respectively. 55

Figure 4-1. Ignition delay time as a function of initial temperature for ethylene/air mixture at pressures of 0.1, 1, and 10 atm, and equivalence ratios of 0.5, 1, 2, and 5, respectively. Solid lines: detailed. Dashed lines: skeletal. Symbols: reduced. 60

Figure 4-2. Temperature profiles in PSRs with inlet temperature 300 K for ethylene/air mixture at pressures of 0.1, 1, and 10 atm, and equivalence ratios of 0.5, 1, 2, and 5, respectively. Solid lines: detailed. Dashed lines: skeletal. Symbols: reduced. 60

Figure 4-3. Mole fractions of H radical and major soot precursors in PSRs at pressure of 1 atm and equivalence ratio of 5. Solid lines: detailed. Dashed lines: skeletal. Symbols: reduced.....61

Figure 4-4. Mole fractions of H radical and major soot precursors in counterflow diffusion flame. Fuel: C_2H_4, oxidizer: air. Pressure is 1 atm, inlet temperature is 300 K, and velocity is 100 cm/s for both fuel and oxidizer streams. Solid lines: detailed. Dashed lines: skeletal. Symbols: reduced. 62

Figure 5-1. (a) 1-D counterflow extinction responses for non-premixed and (b) twin premixed flames with *n*-dodecane as the fuel. P_1 and P_2 are the sampled reaction states on the curves. RSR: reciprocal strain rate. 65

Figure 5-2. Species Lewis numbers at different grid locations for (a) 1-D non-premixed and (b) premixed counterflow flames, respectively. Standard deviations in species Lewis numbers for (c) non-premixed and (d) premixed counterflow flames, respectively. 66

Figure 5-3. (a) Laminar flame speed as a function of equivalence ratio and (b) maximum temperature as a function of reciprocal strain rate in twin premixed counterflow flames, calculated using the detailed MAD model (solid lines) and unity Lewis number approach (dashed lines), respectively. 67

Figure 5-4. Maximum temperature as a function of reciprocal strain rate for counterflow flames with (a) fuel/air mixture against N_2 and (b) twin premixed jets, calculated using the detailed MAD model with and without perturbed fuel diffusivity, respectively. 69

Figure 5-5. (a) Maximum temperature as a function of reciprocal strain rate for twin premixed counterflow flames at different equivalence ratios, calculated using the detailed MAD model with and without perturbed fuel diffusivity, respectively. (b) Temperature profiles calculated with the detailed MAD for four near extinction states P_1, P_2, P_3, and P_4. 70

Figure 5-6. Patterns for the binary diffusion coefficient matrix of the detailed MAD model (left), bundled model (middle), and Model 1 (right), respectively. Black pixels are the entries that need to be evaluated. 77

Figure 5-7. Patterns for binary diffusion coefficient matrix of the detailed MAD model (left), Model 2 (middle), and Model 3 (right), respectively. Black pixels are the entries that need to be evaluated. 78

Figure 5-8. Laminar flame speed (left *y*-axis) and global extinction strain rate (right *y*-axis) as functions of equivalence ratio, calculated using the detailed MAD, bundled, and Models 1-3, respectively. 79

Figure 5-9. (a) Temperature contour for the 2-D DNS of *n*-butane/air at time of 0.4 ms. (b) Worst-case relative errors in species diffusivities as functions of temperature, calculated with different molecular diffusion models. 81

Figure 5-10. Worst-case error in species diffusivity in Model 2 as a function of the relative discrepancy between the mixture mean molecular weight and the molecular weight of N_2 using the 2-D DNS data at 0.4 ms. Dashed line: a reference line with a slope of 1. 82

Figure 5-11. (a) Maximum temperature as a function of reciprocal strain rate for *n*-dodecane non-premixed counterflow. (b) Worst-case error in species diffusivities calculated using the two conditions, P_1 and P_2, sampled from the solutions using the detailed MAD model. 84

Figure 5-12. Worst-case relative errors in species diffusivities as functions of error thresholds. Dashed line: a reference line with a slope of 1. 85

Figure 6-1. Calculated species concentration profiles for the toy problem with α=2 and τ=10^{-6}. Lines: exact solution; Closed symbols: Strang splitting scheme with Δt=10^{-5}; Open symbols: Strang splitting scheme with Δt=10^{-7}.....92

Figure 6-2. Relative errors in species concentrations for the toy problem with α=2, measured at the time when A = 0.5 in the exact solution, as functions of the splitting time step for the second-order Strang splitting scheme. Dotted line shows the trend line with slope of 2. 94

Figure 6-3. Relative errors in species concentrations for the toy problem, measured at the time A = 0.5 in the exact solution, as functions of α, for the Strang splitting scheme with Δt=10^{-5}.....95

Figure 6-4. Concentrations of B and R calculated with the Strang splitting scheme with $\Delta t=10^{-4}$ for the toy problem with (a) $\alpha=2$ and (b) $\alpha=1$. The solid lines indicate the exact solutions and markers are from the Strang splitting scheme. The dash line indicates the end of integration of Eq. (1-5) and the beginning of the integration of Eq. (1-7). The jump in R results from the integration of Eq. (1-6). 96

Figure 6-5. Temperature profiles of constant-pressure auto-ignition of hydrogen/air mixture, calculated using the fully implicit solver DASAC (solid line), AHI method with $h=10^{-7}$s (circles), and explicit first-order Euler scheme with $h=10^{-8}$s(dots), respectively. The vertical dashed line indicates when the fastest reaction timescale becomes smaller than the explicit integration time step. 101

Figure 6-6. The shortest reaction timescale and temperature profile as functions of time for constant-pressure auto-ignition of hydrogen/air. The vertical dashed line indicates when the fastest reaction timescale becomes smaller than the explicit integration time step.....102

Figure 6-7. (a) Profiles of species mass fractions for constant-pressure auto-ignition of hydrogen/air, calculated using DASAC (solid lines) and the AHI method with $h=10^{-7}$s (symbols), respectively. (b) Relative errors in species mass fractions between AHI and DASAC.....103

Figure 6-8. Ignition delay of constant-pressure auto-ignition as a function of the initial temperature for hydrogen/air, calculated with DASAC (solid line) and the AHI method with $h=10^{-7}$s (circles), respectively. 104

Figure 6-9. Dependence of local relative errors on the integration time step size for constant-pressure auto-ignition of stoichiometric hydrogen/air. Dotted line: trend line with slope of 2. Symbols: measured relative errors. 105

Figure 6-10. (a) Number of fast species in constant-pressure auto-ignition, and (b) CPU time for the integration constant-pressure auto-ignition, normalized by that of fully implicit integration, and for unsteady PSR, normalized by that of the Strang splitting scheme using VODE, for hydrogen-, ethylene- and methane-air mixtures, respectively, at atmospheric pressure. 108

Figure 6-11. Profiles of species concentrations in the toy problem with α=2 and τ=10^{-6}, calculated with the AHI method with h=10^{-5} (open symbols) and the Strang splitting scheme with Δt==10^{-5} (closed symbols), respectively, in comparison with the exact solution (lines). 110

Figure 6-12. Relative errors in *B* for the toy problem, measured at time when *A* = 0.5 in the exact solution, as functions of the time step, i.e. Δt for the Strang splitting scheme and h for AHI, with α=0.5 for cases with different timescales of *R*. Closed symbols: Strang splitting scheme. Open symbols: AHI. Triangles: τ=10^{-8}, circles: τ=10^{-6}. The dotted trend line has slope of 2 and the dashed line has slope of 1. 111

Figure 6-13. (a) Temperature, and (b) mass fraction of H and the fraction of H radical creation rate attributed to transport as functions of time in an unsteady PSR for H_2/air with equivalence ratio of ϕ=0.3. The mixture inlet stream is fresh mixture of H_2/air at ϕ=0.3 and inlet temperature T_{in} = 875 K enriched with 0.1% H radical (in mass). 114

List of Tables

Table 1-1. Computational cost for the evaluation of source terms 3

Table 1-2. Computational cost for the solver components 3

Table 2-1. The skeletal fuel pyrolysis sub-model for *n*-dodecane 17

Table 3-1. Summary of the target fuels in the present study 35

Table 3-2. Sizes of the detailed, skeletal and reduced models 37

Table 3-3. Near-LBO conditions for PSR 49

Table 5-1. Speedup factors of reduced MAD models 86

Table 5-2. Major features of reduced MAD models 86

Table 7-1. Summary of reduced kinetic models developed in this study 119

Table of Contents

ACKNOWLEDGMENT ..... **iv**

List of Figures ..... **vi**

List of Tables ..... **xiv**

Table of Contents ..... **xv**

Chapter 1 Introduction **1**

1.1 Motivation 1

1.2 Background 2

1.2.1 Computational cost analysis 2

1.2.2 Kinetic model reduction 4

1.2.3 Reduced molecular diffusion models 6

1.2.4 Advanced stiff chemistry solvers 8

1.3 Organization of the dissertation 11

1.4 List of peer-reviewed publications 12

Chapter 2 A Reduced High-Temperature Kinetic Model of *n*-Dodecane with Lumped Fuel Cracking Steps **13**

2.1 Introduction 13

2.2 Development and validation of a reduced model for *n*-dodecane with lumped fuel cracking steps 15

2.2.1 Development of the reduced model 15

2.2.2 Comprehensive model validations 18

2.3 Fuel cracking in DNS of a turbulence premixed flame 27

2.4 Concluding remarks.....33

Chapter 3 Reduced High-Temperature Kinetic Models of Real Jet Fuels Based on HyChem Models.....34

3.1 Introduction.....34

3.2 Model reduction for the detailed HyChem models 36

3.2.1 Development of fuel-specific reduced models.....36

3.2.2 Development of a universal reduced model 37

3.2.3 A reduced NO sub-model 38

3.3 Results and discussion.....39

3.3.1 Validations of the fuel-specific reduced models.....39

3.3.2 Validation of the universal reduced model.....42

3.3.3 Validation of the universal reduced model with NO.....46

3.3.4 Validation for lean blow-out (LBO) of PSR.....47

3.3.5 Fuel sensitivities of the reduced models.....52

3.4 Concluding remarks.....55

Chapter 4 A Reduced Kinetic Model for Ethylene/Air Combustion with Polycyclic Aromatic Hydrocarbons Formation Pathways.....57

4.1 Introduction.....57

4.2 Development of the reduced model....57
4.3 Validation of the reduced model....58
4.4 Concluding remarks....62
Chapter 5 Efficient Approaches to Mixture-Averaged Diffusion Modeling....63
5.1 Introduction....63
5.2 Effects of molecular diffusion....64
5.2.1 Variations of species Lewis numbers in *n*-dodecane counterflow flames....64
5.2.2 Unity Lewis number and the MAD model in premixed flames....66
5.2.3 Fuel diffusion effects on premixed counterflow flame extinction....67
5.3 Methodologies....70
5.3.1 A brief review of the diffusive species bundling approach....70
5.3.2 A reduced MAD model based reaction states sampling and species bundling ...72
5.3.3 A linear-time reduced MAD model for premixed fuel/air combustion....74
5.4 Results and discussion....76
5.4.1 Structure of the binary diffusion coefficient matrix....76
5.4.2 Validation of global flame responses and a posteriori validation of species diffusivities....78
5.4.3 Model 1 for non-premixed flames....82
5.4.4 Error control study of Model 1....84
5.4.5 Speedup factors and major features of reduced MAD models....85

5.5 Concluding remarks....87

Chapter 6 A Dynamic Adaptive Method for Hybrid Integration of Stiff Chemistry 89

6.1 Introduction....89

6.2 A toy problem with the Strang splitting scheme....90

6.3 A dynamic adaptive method for hybrid integration....97

6.3.1 Identification of fast and slow reactions and species....97

6.3.2 A dynamic adaptive method for hybrid integration....98

6.4 Results and discussion....100

6.4.1 Accuracy and efficiency of the AHI method....100

6.4.2 Comparisons of the AHI method and the Strang splitting scheme....109

6.5 Concluding remarks....115

Chapter 7 Summaries and Future Work....117

References....122

Appendix....129

A. QSS species for deriving the 24-species reduced model for *n*-dodecane....129

B. QSS species for deriving the 25-species reduced model for *n*-butane....130

C. QSS species for deriving the 31-species reduced HyChem model for A2....131

D. QSS species for deriving the 26-species reduced HyChem model for C1....132

E. QSS species for deriving the 31-species reduced HyChem model for C5....133

F. QSS species for deriving the 35-species universal reduced HyChem model....134

G. QSS species for deriving the 45-species universal reduced HyChem model with NOx ……...135

H. QSS species for deriving the 86-species reduced model for C_2H_4 with PAH.....136

Chapter 1 Introduction

1.1 Motivation

Combustion of fossil fuels, such as coal, petroleum, and natural gas constitutes more than 80% of the world energy sources in 2015 [1]. However, combustion is also the major source of pollution emissions, such as carbon monoxide, unburned hydrocarbons, nitrogen oxides, and particular matters. The increasing demand in energy necessitates the research on alternative energy sources as well as higher engine and fuel efficiencies. While experiments have been a major approach for these purposes, computational fluid dynamics (CFD), such as the state-of-the-art direct numerical simulations (DNS) and large eddy simulations (LES), has become another important approach to understanding complex combustion problems by providing detailed information on the underlying physicochemical processes, where detailed chemistry is of great importance for accurate prediction of complex flame behaviors, such as ignition, extinction and flame propagation [2, 3]. A major challenge in the incorporation of detailed chemistry in combustion CFD simulations is attributed to the large sizes of detailed reaction models, in which thousands of species and reactions can be involved, especially for large hydrocarbons, such as gasoline, diesel, and jet fuels. Chemical stiffness resulting from the short timescales associated with highly reactive radicals and fast reactions imposes another challenge to CFD with detailed chemistry. In the following, the most time-consuming components in reacting flow simulations will be discussed in detail.

1.2 Background

1.2.1 Computational cost analysis

After spatial discretization of the equations for a multi-dimensional unsteady reacting flow, the problem is governed by a set of ordinary differential equations (ODEs), with the right-hand side involving the chemical source term, the diffusion source term, and others.

Based on the analysis in Ref. [2], evaluation of the chemical source term is typically a linear function of the number of reactions, I, where I is statistically a linear function of the number of species, K. As such, the cost is a linear function of K and is moderate compared with other components to be discussed in the following, even for large reaction models.

The evaluation of the diffusion source term with detailed molecular diffusion models incurs a cost of $O(K^2)$ when the mixture-averaged diffusion (MAD) is used [4], due to the evaluation of the $K \times K$ binary diffusion coefficient matrix. The cost can even become $O(K^3)$ if the multi-component diffusion (MCD) is used [5], due to the expensive matrix inversion operations. Although some methods have been proposed to reduce the computational cost of the MCD model [6-9], the MAD model is more widely used in practical flame simulations [10] due to its satisfactory accuracy and substantially lower computational cost compared with the MCD model in many cases. However, the MAD model can still be time-consuming when the reaction model is large.

In addition to the evaluation of the source terms, a significant portion of the computational cost can be attributed to the solver components. To time-integrate the governing equations involving detailed chemistry, the low-cost explicit solvers are typically inapplicable due to the chemical stiffness mentioned earlier, particularly when relatively large integration time steps are adopted. As such, implicit solvers that can handle the chemical stiffness, such as VODE [11] and

DASAC [12], are typically required to maintain the numerical stability in time integrations with reasonably large time steps. In such cases, the time-consuming Jacobian matrix evaluation and LU decomposition are involved, and thus the computational cost is typically $O(K^2)$ for small to moderately large reaction models where the Jacobian evaluation dominates the computational cost, and is $O(K^3)$ for large reaction models where the LU decomposition becomes the most time-consuming operation.

The asymptotic computational costs for different components are summarized in Table 1-1 and Table 1-2. From the above analysis, several approaches can be employed to enable efficient application of detailed chemistry in CFD simulations: to reduce the number of species and reactions such that the number of equations and the complexity of the source terms can be reduced, to reduce the high computational cost of the detailed molecular diffusion models, and to develop efficient stiff chemistry solvers. This dissertation will be focused on these three approaches, which are to be sequentially discussed in the following.

Table 1-1. Computational cost for the evaluation of source terms

	Chemical source term	Diffusion source term
Evaluation of source terms	$O(K)$	$O(K^2)$ with MAD $O(K^3)$ with MCD

Table 1-2. Computational cost for the solver components

	Explicit solver	Implicit solver
Solver components	$O(K)$, no expensive Jacobian operations	$O(K^2)$-$O(K^3)$ due to Jacobian evaluation and LU decomposition
	Time step typically limited by the stiffness	Can handle the stiffness with larger steps

1.2.2 Kinetic model reduction

An important approach to accommodating detailed chemistry in CFD simulations is to reduce the sizes of the detailed reaction models for specified accuracy requirements through, for example, skeletal reduction and time-scale based reduction.

Skeletal reduction is achieved through the elimination of unimportant species and reactions from the detailed reaction models. A variety of methods have been proposed for skeletal reduction, such as sensitivity analysis [13-16], Jacobian based methods [17, 18], directed relation graph (DRG) [19-22], and other DRG-based methods such as DRG with expert knowledge (DRG-X) [23], DRG with error propagation (DRGEP) [24], and path flux analysis (PFA) [25] *etc.* Among these methods, DRG and DRG-based methods are highly efficient and have been applied in dynamic adaptive chemistry (DAC) [26-29].

DRG is based on the observation that many species are only weakly coupled during the combustion processes, such that the species that do not significantly affect the reaction rates of the major species can be eliminated from the detailed reaction model. In DRG, the couplings of species are abstracted to a directed graph, where each species is uniquely mapped to a vertex. A pair-wise error, r_{AB}, which represents the direct impact on species *A* by removing species *B*, is defined as:

$$r_{AB} \equiv \frac{\max_i \left|\nu_{A,i}\omega_i\delta_{Bi}\right|}{\max_i \left|\nu_{A,i}\omega_i\right|}, \delta_{Bi} = \begin{cases} 1, & \text{if the } i\text{th reaction involves } B, \\ 0, & \text{otherwise.} \end{cases} \tag{1-1}$$

where the subscript *i* indicates the *i*th reaction, $\nu_{A,i}$ is the stoichiometric coefficient of species *A* in the *i*th reaction, and ω_i is the net production rate. If and only if $r_{AB} > \varepsilon$, where ε is a user-specified error threshold, there is a directed edge from species *A* to *B*. Starting from one or more major species, such as the fuel or H radical, an efficient linear-time graph search is performed to discover

the species coupled with the starting species [19]. The species that are not strongly coupled with the starting species are eliminated from the detailed model to obtain a smaller skeletal model.

DRG-X [23] is a direct derivative of DRG. While DRG only allows for a uniform error threshold in the edge truncation, DRG-X allows for species-specific error tolerances, such that DRG-X is more suitable to reduce reaction models with disparate uncertainties in different reaction pathways. DRGEP models the error propagation in the directed graph [24], where geometric decay is assumed along the graph searching paths, such that species further away from the starting species are prone to be eliminated. A more detailed comparison of DRG-based methods can be found in [30].

The DRG-based methods are highly efficient and thus suitable to be applied as the first step to reduce large detailed models followed by more time-consuming reduction methods. In contrast, sensitivity analyses are typically computationally expensive and can be used as the last step in the reduction to obtain skeletal models of minimal sizes. DRG-aided sensitivity analysis (DRGASA) [13, 16] and DRGEP with sensitivity analysis (DRGEPSA) [31] are examples of sensitivity analyses expedited by exploiting the output information from the DRG-based methods. In DRGASA, the species coupling information obtained from DRG is utilized to reduce the number of species to be tested compared with the brute-force sensitivity analysis on every species. After the skeletal reduction with DRG and DRGASA, reactions with negligible contributions to every retained species can be further removed to obtain a skeletal model with a smaller set of reactions [22].

In addition to the skeletal reduction that eliminates unimportant species and reactions, time-scale based reduction can replace some differential equations with algebraic equations by assuming the fast chemical processes are exhausted. Such methods include, for example, quasi-

steady state (QSS) approximation (QSSA) [14, 32-34], partial equilibrium (PE) approximation (PEA) [35, 36], computational singular perturbation (CSP) [37-41], and intrinsic low dimensional manifold (ILDM) [42-44]. While CSP and ILDM can handle QSS species and PE reactions in a systematic way, eigen-decomposition is involved in such methods such that the computational cost is high for large reaction models. In contrast, PEA and QSSA methods, when appropriately applied, may be computationally efficient and thus can be exploited on-the-fly in flame simulations. The globally valid QSS species can typically be removed from the transported equations and solved internally by using the resulting algebraic equations. Lu and Law developed a CSP-based method to identify QSS species [32] and a linearized QSSA (LQSSA) method to solve the algebraic equations analytically with high efficiency and robustness [45].

In the present study, a two-stage reduction approach [2, 22] integrating the skeletal reduction with DRG and sensitivity analysis and the time-scale based reduction with LQSSA is employed to derive compact CFD-amenable reduced reaction models for a variety of fuels in Chapter 2, Chapter 3, and Chapter 4.

1.2.3 Reduced molecular diffusion models

Compared with the extensive study of kinetic model reduction, reduction of molecular diffusion models has received less attention. Rather than tracking the detailed molecular diffusion, the unity Lewis number approach is often used in practical simulations due to its great simplicity. However, this simple approach will fail when differential diffusion effects are important. Prescribing constant but non-unity species Lewis numbers can alleviate the problem [46] with the Lewis numbers obtained from numerical simulations of 1-D premixed or non-premixed flames. This approach can account for some differential diffusion effects but may still fail where the constant Lewis number assumption does not apply, as shown in some non-premixed flames [47].

In addition to detailed chemistry, accurate modeling of molecular diffusion has also been found important to predict many combustion problems, such as near-limit flame behaviors and premixed flame propagation [2, 48, 49]. Even for turbulent flames at high Reynolds numbers, differential molecular diffusion was found to play important roles through both experimental measurements [50-54] and numerical simulations [47, 49, 55, 56]. In a recent study, Bruno *et al.* [55] compared three molecular diffusion models, namely the unity Lewis number model, the MAD model and the MCD model, in a DNS of a partially premixed turbulent syngas/air flame. It was found that unity Lewis number model is far less accurate compared with MAD and MCD, and can yield unphysical results, while MAD and MCD are quite close to each other under the tested conditions. Therefore, it is important to investigate detailed or reduced molecular diffusion models for efficient flame simulations, and the present study is focused on the widely used MAD model.

The species diffusion velocity, $\boldsymbol{V}$, evaluated with the MAD model without thermal diffusion (Soret effect) or other correction effects can be written as

$$\boldsymbol{V}_i = \bar{D}_i \frac{\nabla X_i}{X_i}, \tag{1-2a}$$

$$\bar{D}_i = \frac{1 - Y_i}{\sum_{j \neq i}^{K} \frac{X_j}{D_{i,j}}}, \tag{1-2b}$$

where the subscript i indicates the ith species, $\bar{D}$ is the mixture-averaged species diffusivity, Y is the species mass fraction, and X is the mole fraction. $D_{i,j}$ is the binary diffusion coefficient between the ith and jth species, and is typically fitted with an Nth order polynomial in simulations [57]:

$$pD_{i,j} = \exp(\sum_{n=0}^{N} a_{n,i,j}(\ln T)^n), \quad (1\text{-}3)$$

where $a_{n,i,j}$ is the polynomial coefficient, and p is pressure.

The computational cost of the MAD model is typically dominated by the expensive evaluation of the binary diffusion coefficients in Eq. (1-3), which is a quadratic function of the number of species. Furthermore, the evaluation of species diffusivities can be computationally intensive when it is called at every grid point and time step as reported in [47].

To reduce the computational cost of the MAD model, Lu and Law [58] developed a systematic method to bundle the diffusive species with similar binary diffusion coefficients into groups, such that the computational cost of evaluating the binary diffusion matrix is reduced from $O(K^2)$ to $O(KG^2)$, where KG is the number of bundled groups and is smaller than K. In Chapter 5 of the present study, the diffusive species bundling approach is extended. Three new methods are proposed to obtain efficient and accurate reduced MAD models.

1.2.4 Advanced stiff chemistry solvers

In DNS of some compressible reacting flows, the Courant-Friedrichs-Lewy (CFL) condition may limit the integration time step to a rather small value, say, 10 *ns* [3]. In such cases, chemical stiffness can be removed on-the-fly to enable low-cost explicit solvers without significant overhead due to the sparse coupling of the fast chemical processes [2]. However, stiffness removal for simulations with significantly larger time steps remains a challenge due to the densely-coupled fast chemical processes and the presence of PE reactions. In such cases, implicit solvers that can deal with stiffness effectively are required.

The computational overhead of conventional implicit solvers is primarily attributed to the Jacobian evaluation and LU decomposition, which scales as $O(K^2)$ and $O(K^3)$, respectively. Evaluation of the Jacobian matrix can typically be expedited through analytic techniques [2], and the high computational cost associated with LU decomposition can be reduced by preconditioning [59] and sparse matrix techniques [60-64]. However, in multi-dimensional flow simulations, due to the large number of spatial grid points involved, fully implicit integration schemes induce tremendous computational costs for simulations of and are thus infeasible. Semi-implicit methods have been widely adopted in such cases including, for example, the Implicit-Explicit (IMEX) schemes [65-67] that combine implicit and explicit discretizations for stiff and non-stiff source terms respectively, operator-splitting schemes [68-75] that integrate chemistry and transport in different sub-steps with tailored solvers, the semi-implicit iterative methods with preconditioned chemical Jacobian [76], *etc*. Among these methods, operator-splitting schemes are frequently used due to their good accuracy in many cases and easy implementation, such that the expensive implicit solvers are only invoked for the integration of local chemistry, while efficient flow solvers can be employed to integrate the non-chemical source terms. In particular, the Strang splitting scheme [74, 75] is among the most widely used operator splitting schemes for reacting flows involving stiff chemistry, for which the spatially discretized governing equations can be expressed as:

$$\frac{d\boldsymbol{\Phi}}{dt} = \boldsymbol{M}(\boldsymbol{\Phi}) + \boldsymbol{S}(\boldsymbol{\Phi}) \tag{1-4}$$

where $\boldsymbol{\Phi}$ is the vector of the thermo-chemical compositions, including, *e.g.* temperature and species mass fractions. The operators, $\boldsymbol{M}$ and $\boldsymbol{S}$, are for the transport and chemistry terms, respectively. To solve Eq. (1-4) using the second-order Strang splitting scheme [74, 75], the time domain is discretized into uniform intervals of size Δt, which are referred to as the splitting time

steps. In each splitting time step, time-integration can be performed in the following sequence, namely the $\boldsymbol{S}/2-\boldsymbol{M}-\boldsymbol{S}/2$ scheme:

$$\frac{d\boldsymbol{\Phi}^{(1)}}{dt}=\boldsymbol{S}\left(\boldsymbol{\Phi}^{(1)}\right),\qquad \boldsymbol{\Phi}^{(1)}(0)=\boldsymbol{\Phi}^{n}\ on\ [0,\Delta t/2\ ] \tag{1-5}$$

$$\frac{d\boldsymbol{\Phi}^{(2)}}{dt}=\boldsymbol{M}\left(\boldsymbol{\Phi}^{(2)}\right),\qquad \boldsymbol{\Phi}^{(2)}(0)=\boldsymbol{\Phi}^{(1)}(\Delta t/2\ )\ on\ [0,\Delta t] \tag{1-6}$$

$$\frac{d\boldsymbol{\Phi}^{(3)}}{dt}=\boldsymbol{S}\left(\boldsymbol{\Phi}^{(3)}\right),\qquad \boldsymbol{\Phi}^{(3)}(0)=\boldsymbol{\Phi}^{(2)}(\Delta t)\ on\ [0\ ,\Delta t/2] \tag{1-7}$$

where $\boldsymbol{\Phi}^{n}$ is the composition at the beginning of the n^{th} splitting time step. The initial conditions of Eqs. (1-6) and (1-7) are the solutions of their previous sub-steps Eqs. (1-5) and (1-6), respectively, and $\boldsymbol{\Phi}^{(3)}(\Delta t/2)$ is the solution at the end of the splitting time step. The transport sub-step Eq. (1-6) can typically be explicitly integrated in one step if the splitting time step is sufficiently small to resolve the transport term, while the chemistry sub-steps in Eqs. (1-5) and (1-7) typically require multiple implicit steps using stiff ODE solvers. The above scheme features second-order accuracy for sufficiently small splitting time steps and is rather straightforward to implement. Note that one can build a $\boldsymbol{M}/2-\boldsymbol{S}-\boldsymbol{M}/2$ scheme in a similar manner, which is nevertheless less accurate than the $\boldsymbol{S}/2-\boldsymbol{M}-\boldsymbol{S}/2$ scheme as discussed in [71].

However, in Chapter 6 of the present study, it is found that splitting stiff chemistry and transport may incur significant errors when significant radical sources are present in the transport term. An advanced chemistry solver for stiff chemistry, namely the dynamic adaptive hybrid integration (AHI), is thereby proposed as a substitute of operator splitting schemes for such cases. In AHI, the chemical source term is evaluated semi-implicitly while the transport term is evaluated explicitly, such that expensive implicit ODE solvers are only invoked for the local chemistry, and chemistry and transport are integrated together to eliminate the splitting errors. In addition, by

identifying fast/slow species and reactions on-the-fly with an efficient CSP criterion, only fast species are solved implicitly to reduce the size of the implicit core and consequently the high computational cost associated with expensive Jacobian operations, while slow species are solved using the low-cost explicit solvers.

1.3 Organization of the dissertation

Chapter 2 presents a 24-species reduced model with lumped fuel cracking steps for high-temperature (high-T) combustion of *n*-dodecane as a jet fuel surrogate. To facilitate the DNS study of fuel cracking behaviors, a 25-species reduced model for *n*-butane/air combustion is further developed. The fast fuel cracking assumption under high-T conditions are validated in 0-D, 1-D, and a 2-D DNS.

In Chapter 3, highly compact reduced models with approximately 30 species are developed for high-T combustion of several representative real jet fuels based on the HyChem models [77, 78] which consist of lumped fuel cracking steps and a detailed oxidation core for small molecules.

In Chapter 4, an 86-species reduced model and a 99-species skeletal model for ethylene/air combustion with polycyclic aromatic hydrocarbons (PAHs) are developed for efficient CFD simulations of sooting flames.

In Chapter 5, the previous developed species bundling approach is extended, and three new approaches are proposed to further reduce the computational cost of the MAD model.

In Chapter 6, a failing scenario of the operator-splitting schemes is identified and demonstrated. A new stiff chemistry solver, namely AHI, is proposed and compared with the Strang splitting scheme.

Summary of the dissertation and recommendations for future work are given in Chapter 7.

1.4 List of peer-reviewed publications

- **Y. Gao**, Y. Liu, Z. Ren, T. Lu, "A dynamic adaptive method for hybrid integration of stiff chemistry", *Combustion and Flame* 162 (2) (2015) 287-295.
- A. Vié, B. Franzelli, **Y. Gao**, T. Lu, H. Wang, M. Ihme, "Analysis of segregation and bifurcation in turbulent spray flames: A 3D counterflow configuration", *Proceedings of the Combustion Institute* 35 (2) (2015) 1675-1683.
- **Y. Gao**, R. Shan, S. Lyra, C. Li, H. Wang, J. H. Chen, T. Lu, "On lumped-reduced reaction model for combustion of liquid fuels", *Combustion and Flame* 163 (2016) 437-446.
- P. Selvaraj, P. G. Arias, B. J. Lee, H. G. Im, Y. Wang, **Y. Gao**, S. Park, S. M. Sarathy, T. Lu, S. H. Chung, "A computational study of ethylene–air sooting flames: Effects of large polycyclic aromatic hydrocarbons", *Combustion and Flame* 163 (2016) 427-436.
- Z. Ren, Z. Lu, **Y. Gao**, T. Lu, L. Hou, "A kinetics-based method for constraint selection in rate-controlled constrained equilibrium", *Combustion Theory and Modelling* (2016) 1-24.
- C. Xu, **Y. Gao**, Z. Ren, T. Lu, "A sparse stiff chemistry solver based on dynamic adaptive integration for efficient combustion simulations", *Combustion and Flame* 172 (2016) 183-193.

Chapter 2 A Reduced High-Temperature Kinetic Model of *n*-Dodecane with Lumped Fuel Cracking Steps

2.1 Introduction

The emissions from hydrocarbon combustion have been impacting the environment continuously. Although aviation only contributes to approximately 2% of the global anthropogenic greenhouse emissions and 11% of the US transportation sector's share, aircraft emissions at the cruise altitudes can significantly affect the atmosphere compared with the emissions on the surface [79].

However, kinetic modeling of jet fuel combustion is a challenging task. Practical jet fuels typically contain a large number of components with wide varying molecular structures. In addition to the multicomponent nature, the high complexity of practical fuel combustion chemistry is also attributed to the myriad intermediate species generated during the pyrolysis and oxidation processes. While developments employing detailed modeling and surrogate fuel approaches are advancing rapidly, challenges abound in the application of the chemistry model in turbulent flame simulations. Both the underlying chemical complexities, which lead to model inaccuracy, and the large model size, which imposes infeasible computational expense, are some of the fundamental factors that limit the broader utilization of the chemistry efforts.

Fuel cracking is slow and rate-limiting at low-temperature conditions, and thus typically needs to be resolved [80-82]. However, fuel cracking through beta-scission occurs rather fast at high temperatures compared to the subsequent oxidation of the resulting small molecules. In a previous work, You *et al.* [83] examined the reaction chemistry of *n*-dodecane combustion under a wide range of conditions. The primary conclusion of that study is that in high-T combustion, *n*-dodecane undergoes complete pyrolysis, yielding methane, ethylene, propene, butene, and

molecular hydrogen, before these smaller molecular weight fragments are oxidized. The oxidation of these fragments is rate-limiting for all conditions tested. These conclusions are consistent with experimental observations made later in shock tubes [84, 85]. For these reasons, the fuel cracking processes may be approximated by a few semi-global reaction steps [83], which can subsequently be grafted on to a detailed C_1-C_4 model core, *e.g.* the USC-Mech II [86], to obtain compact hybrid models for high-T combustion [83, 87]. The resulting models can further be reduced.

Nevertheless, in the work of You *et al.* [83], most of the combustion properties considered are those with negligible back mixing of burned or unburned mixtures. What was also not adequately studied was the near-limit phenomena, notably the extinction and ignition states in perfectly stirred reactors (PSRs), which are typically turning points of the *S*-curve response [48]. In this chapter, the potential of using combined hybrid model development and model reduction to obtain highly efficient reduced models with less than 30 species for large hydrocarbon fuel combustion at high-T conditions is investigated.

First, a 24-species reduced model for high-T combustion of a jet fuel surrogate, *n*-dodecane, is developed from a version of JetSurF with lumped fuel cracking reaction steps [87] using the two-stage reduction method. Second, the hybrid model is assessed in a variety of reactors and flames, including auto-ignition, PSR, premixed flame propagation, and extinction of premixed and non-premixed counterflow flames. The results of the hybrid model are compared with the detailed models. Third, a 25-species reduced *n*-butane model is derived from the detailed USC-Mech II. The reduced model has been employed by Dr. S. Lyra at Sandia in a 2-D DNS of a lean turbulent premixed flame for *n*-butane/air. The validity of the assumption of fast fuel cracking at high-T conditions is subsequently investigated with the DNS data.

2.2 Development and validation of a reduced model for *n*-dodecane with lumped fuel cracking steps

2.2.1 Development of the reduced model

An approach to lump the fuel cracking reactions has been demonstrated in [83, 87]. This approach assumes that the intermediates of the fuel cracking are all in quasi-steady state. It reduces the chemical complexity of the reaction processes and the model size in an efficient manner. For *n*-dodecane, the resulting lumped model contains only three species, namely, *n*-dodecane, 1-pentene and 1-hexene and approximately one and a half dozen reactions. The rate coefficients of the lumped reaction model are based on JetSurF 1.0 [88]. The lumped pyrolysis model was combined with USC-Mech II [86] to obtain a complete model of 123 species and 977 reactions, referred to as JetSurF 1.0-l, which has been validated against the detailed model and experiments over a wide range of conditions [87]. Subsequently, this lumped-detailed reaction model was reduced to 24 species.

The three steps taken in the above model reduction are described here. The DRG-based methods, including DRG and DRGASA, were employed to remove unimportant species and reactions first from a range of combustion responses over the pressure range of 1 to 10 atm, initial temperatures from 1000 to 1600 K for auto-ignition, inlet temperature of 300 K for PSRs, and equivalence ratios from 0.5 to 1.5. The H atom was selected as the starting species in the graph searching in DRG and the obtained skeletal model consists of 47 species and 359 reactions. After skeletal reduction with DRG, the model was further reduced with DRGASA to obtain a smaller model. The worst-case error in target parameters induced by removing a single species was first tested and then sorted in ascending order. The species were then eliminated one by one until the worst-case error in the target parameters reaches the given error tolerance. In DRGASA, auto-

ignition delay with initial temperature from 1000 to 1600 K and extinction residence time of PSRs with inlet temperature of 300 K over the pressure range of 1 to 10 atm and equivalence ratio from 0.5 to 1.5, were selected as the target responses with an error tolerance of 20%. The final skeletal model is comprised of 193 reactions and 31 species: N_2, H, O, OH, HO_2, H_2, H_2O, H_2O_2, O_2, CH_2, CH_2*, CH_3, CH_4, HCO, CH_2O, CH_3O, CO, CO_2, C_2H_2, C_2H_3, C_2H_4, C_2H_5, C_2H_6, CH_2CHO, aC_3H_5 (allyl), C_3H_6, *n*C_3H_7, C_2H_3CHO, C_4H_8-1 (1-butene), *n*$C_{12}H_{26}$ (*n*-dodecane), and C_6H_{12} (1-hexene). Reactions of any eliminated species were also removed. The skeletal sub-model for fuel pyrolysis is provided in Table 2-1. In the last step, this skeletal model was further reduced with the LQSSA method. Seven global QSS species, namely CH_2, CH_2*, HCO, CH_3O, C_2H_3, C_2H_5, and *n*C_3H_7, were identified by excluding all species with nontrivial projection to the slow chemical subspace, thus resulting in a 24-species model. The QSS species are eliminated from the transport equations and can be solved with a set of internal algebraic equations. The QSSA equations are evaluated analytically using a graph-based method [45] to ensure high accuracy and robustness.

Table 2-1. The skeletal fuel pyrolysis sub-model for *n*-dodecane

No.	Reaction	A	n	E_a
1	*n*-$C_{12}H_{26}$ => C_6H_{12}+C_2H_4+*n*-C_3H_7+CH_3	8.53×10^{23}	-2.03	90034
2	*n*-$C_{12}H_{26}$ => C_6H_{12}+2*n*-C_3H_7	5.64×10^{26}	-2.68	88171
3	*n*-$C_{12}H_{26}$ => C_4H_8-1+C_2H_4+2*n*-C_3H_7	7.88×10^{25}	-2.65	88391
4	*n*-$C_{12}H_{26}$ => 2C_3H_6+2*n*-C_3H_7	4.00×10^{26}	-2.66	88392
5	*n*-$C_{12}H_{26}$ +H => C_6H_{12}+C_3H_6+*n*-C_3H_7+H_2	1.30×10^{6}	2.54	6756
6	*n*-$C_{12}H_{26}$ +H => C_6H_{12}+C_3H_6+*n*-C_3H_7+H_2	5.20×10^{6}	2.40	4471
7	*n*-$C_{12}H_{26}$ +O => C_6H_{12}+C_3H_6+*n*-C_3H_7+OH	2.50×10^{6}	2.40	5504
8	*n*-$C_{12}H_{26}$ +O => C_6H_{12}+C_3H_6+*n*-C_3H_7+OH	4.60×10^{5}	2.60	1768
9	*n*-$C_{12}H_{26}$ +OH => C_6H_{12}+C_3H_6+*n*-C_3H_7+H_2O	1.40×10^{7}	1.80	974
10	*n*-$C_{12}H_{26}$ +OH => C_6H_{12}+C_3H_6+*n*-C_3H_7+H_2O	4.00×10^{6}	2.00	-596
11	*n*-$C_{12}H_{26}$ +CH_3 => C_6H_{12}+C_3H_6+*n*-C_3H_7+CH_4	9.03×10^{-1}	3.65	7153
12	*n*-$C_{12}H_{26}$ +CH_3 => C_6H_{12}+C_3H_6+*n*-C_3H_7+CH_4	6.00	3.46	5480
13	*n*-$C_{12}H_{26}$ +O_2 => C_6H_{12}+C_3H_6+*n*-C_3H_7+HO_2	4.00×10^{13}	0.00	50930
14	*n*-$C_{12}H_{26}$ +O_2 => C_6H_{12}+C_3H_6+*n*-C_3H_7+HO_2	1.60×10^{14}	0.00	47590
15	*n*-$C_{12}H_{26}$ +HO_2 => C_6H_{12}+C_3H_6+*n*-C_3H_7+H_2O_2	4.76×10^{4}	2.55	16490
16	*n*-$C_{12}H_{26}$ +HO_2 => C_6H_{12}+C_3H_6+*n*-C_3H_7+H_2O_2	3.80×10^{4}	2.60	13910

Rate coefficient expressed as $k = AT^n\exp(-E_a/RT)$. Units are mole, cm, s, cal, and *K*.

2.2.2 Comprehensive model validations

The reduced model is first compared with the detailed JetSurF 1.0 and the lumped-detailed model, in which the elementary fuel cracking reactions of JetSurF 1.0 are replaced by lumped semi-global steps, for ignition delay and PSR extinction over a wide range of pressures, temperatures and equivalence ratios. Figure 2-1 shows excellent agreement of the three models despite some minor discrepancies between the detailed and lumped-detailed models.

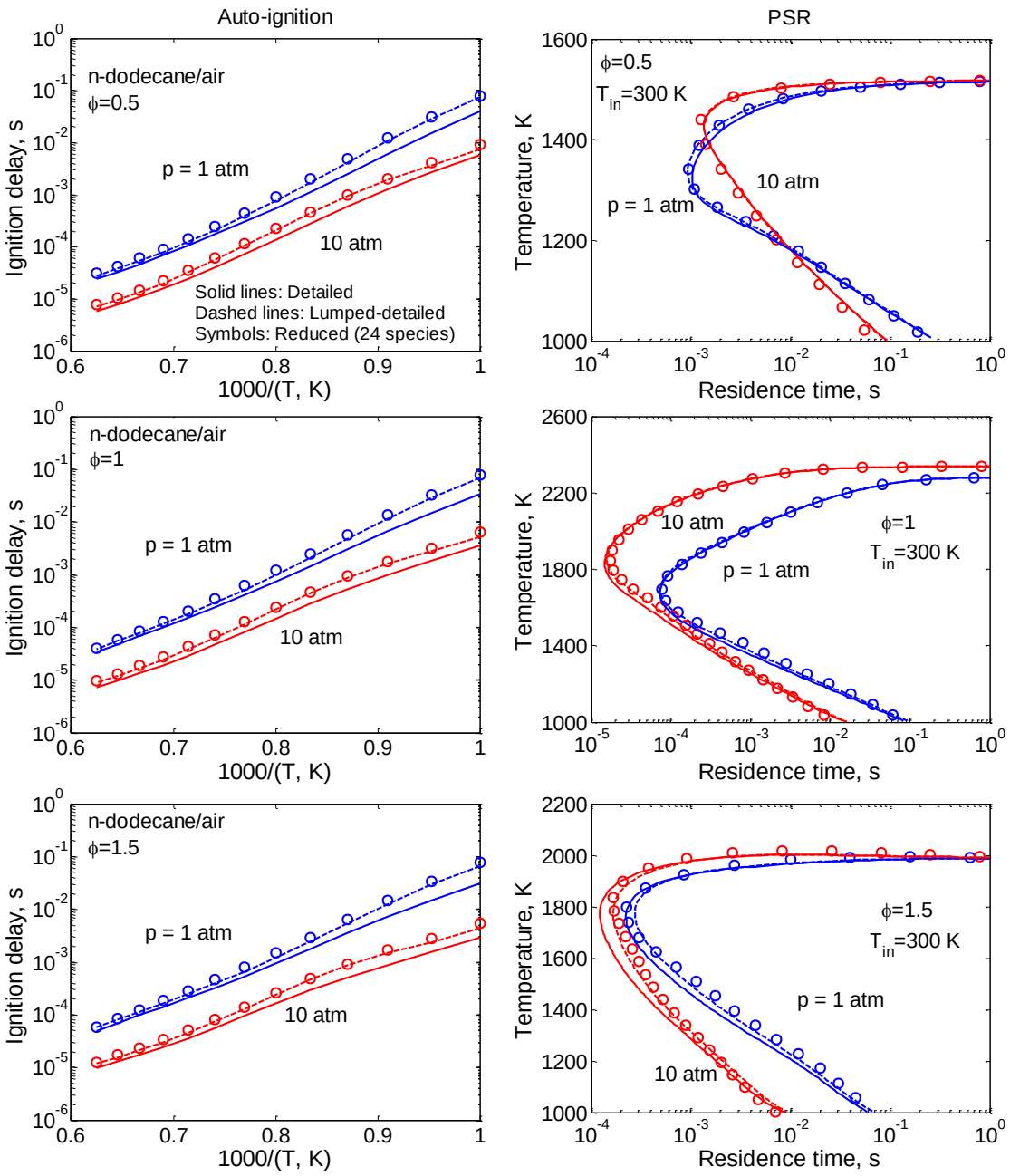

Figure 2-1. Auto-ignition delays (left panels) and extinction temperature of PSR (right panels) for *n*-dodecane/air mixtures at equivalence ratios of 0.5, 1.0 and 1.5 and pressures of 1 and 10 atm, calculated with the detailed JetSurF 1.0 (solid lines), the lumped-detailed model (dashed lines) and the 24-species reduced model (symbols), respectively.

The normalized total mass fraction of the species with four or more carbon atoms, denoted by C_{4+}, are plotted in Figure 2-2 as a function of temperature in auto-ignition and PSRs for different equivalence ratios and pressures. It is noted that, the PSR profiles in Figure 2-2(c) and Figure 2-2(d) are plotted against temperature, which are corresponding to different residence time along the *S*-curve. It is seen that the total mass fraction of C_{4+}, that is the molecules with four or more carbon atoms, decreases rapidly as temperature increases, and the fuel cracking is essentially complete by 1500 K in both the no-mixing (auto-ignition) and fully mixed (PSR) limits. In the context of flames and as will be discussed later, laminar premixed flames or flamelets involve some back mixing due to molecular diffusion. The fact that the fuel cracking process is mostly complete before 1500 K suggests that (a) fuel cracking always occurs in the preheat zone and (b) the fragments that enters the flame zone are primarily $C_{\leq 4}$ species.

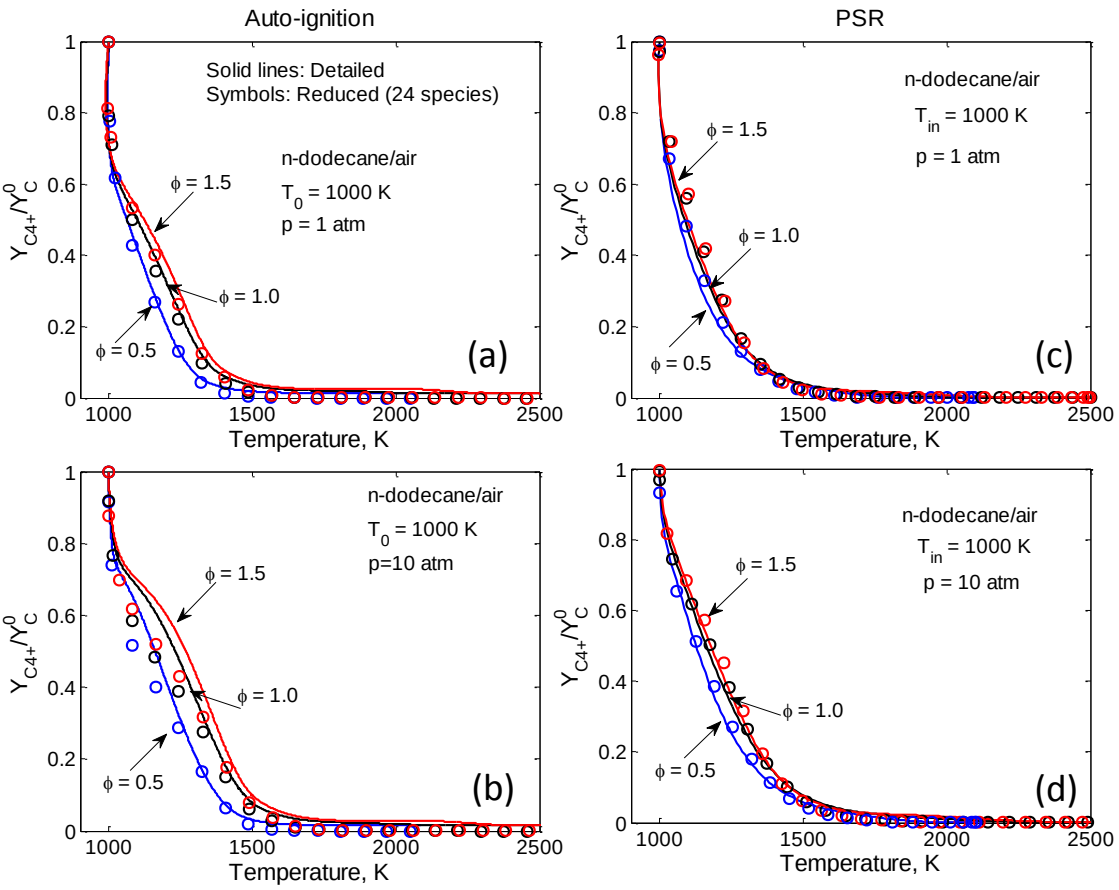

Figure 2-2. Normalized total mass fraction of C_4 species and larger, denoted as C_{4+}, as a function of temperature in auto-ignition and PSRs for *n*-dodecane/air mixtures at equivalence ratios of 0.5, 1.0 and 1.5, and pressures of 1 and 10 atm, calculated with the detailed JetSurF 1.0 (solid lines) and the 24-species reduced model (symbols).

Figure 2-3 compares the laminar premixed flame speed calculated with the reduced, detailed and lumped-detailed models. The reduced model under-predicts the flame speed slightly. In the worst case, the discrepancy between the detailed and lumped-detailed, or lumped-detailed and reduced models is approximately 3 cm/s, occurring near the stoichiometric condition.

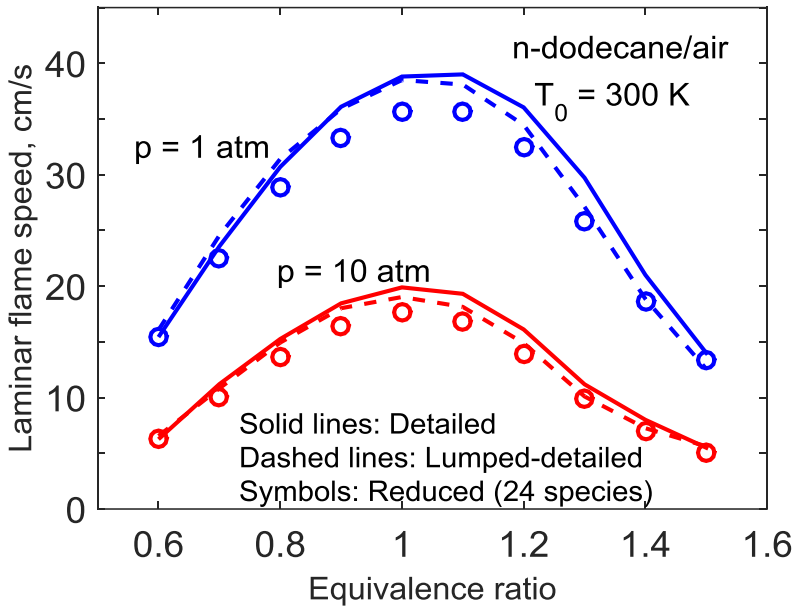

Figure 2-3. Laminar flame speed as a function of equivalence ratio for *n*-dodecane/air mixtures at an initial temperature of 300 K and pressures of 1 and 10 atm.

Figure 2-4 compares simulation results, calculated using the detailed, lumped-detailed and reduced models, and experimental data for auto-ignition delay and laminar flame speed. Figure 2-4(a) shows the calculated ignition delays of *n*-dodecane/air mixture at p = 20 atm and ϕ = 0.5

compared with experimental data in Ref. [89]. Figure 2-4(b) compares calculated laminar flame speed and experimental data [90, 91] for *n*-dodecane/air as function of equivalence ratio at atmospheric pressure and freestream temperature of 403 K. It is seen that, compared with detailed and lumped-detailed models, the reduced model under-predicts the flame speed with a worst-case error of approximately 5 cm/s near the stoichiometric condition.

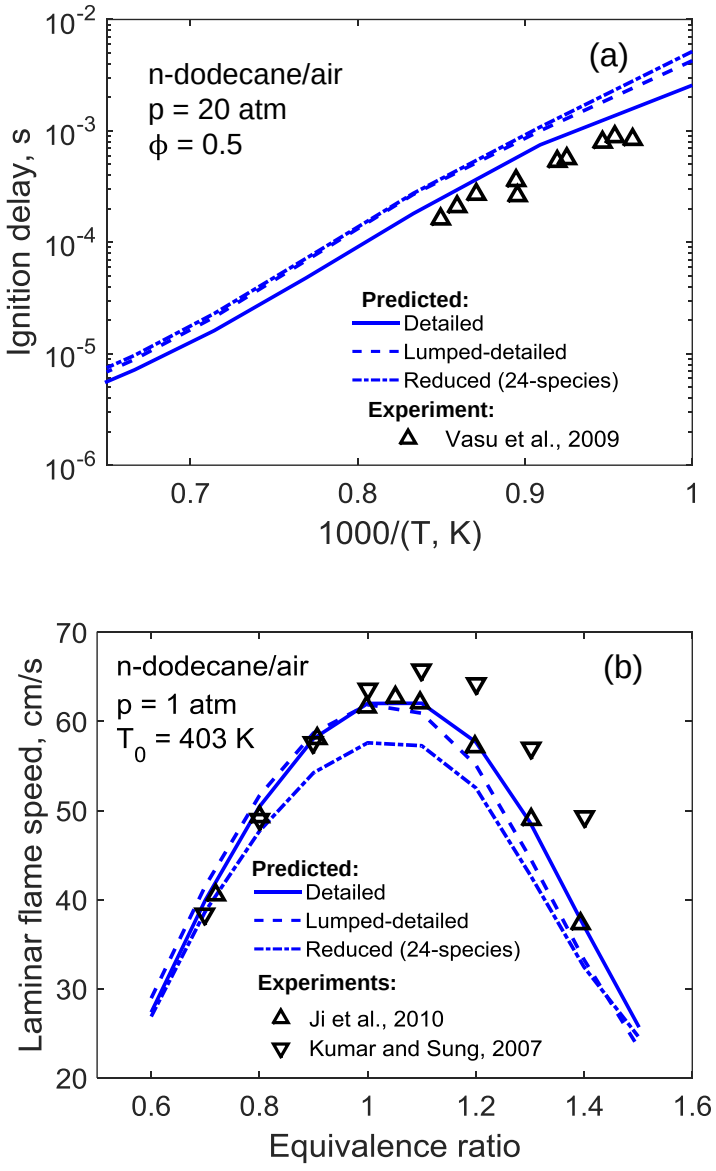

Figure 2-4. Comparison of predicted results (lines) and experimentally measurements (symbols) for *n*-dodecane/air: (a) ignition delay at ϕ = 0.5, p = 20 atm, (b) laminar flame speed as function of equivalence ratio at atmospheric pressure and freestream temperature of 403 K.

To further investigate the validity of the model reduction approaches, the flame response to flow strain was tested in both non-premixed and premixed one-dimensional counterflow flames, comparing predictions made by three models. For non-premixed flames, the fuel jet is comprised of 50% (mol) *n*-dodecane in N_2, and the oxidizer jet is air, both of which are at 300 K and 1 atm. Figure 2-5(a) shows the maximum temperature, $T_{\max}$, computed for the non-premixed counterflow flames as a function of the strain rate a_2, defined in Ref. [92] as

$$a_2 = \frac{2|V_2|}{L}\left(1 + \frac{|V_1|\sqrt{\rho_1}}{|V_2|\sqrt{\rho_2}}\right) \tag{2-1}$$

where the subscripts 1 and 2 denote the fuel and oxidizer boundaries, respectively, V is the axial component of the inlet velocity, ρ is density, and L is the burner separation distance which is 2 cm in the present study. It is seen in Figure 2-5 that the lumped model agrees well with the detailed model over the entire $T_{\max}$-vs.-1/a curves, including the turning point, which corresponds to the extinction state of the flame. In the worst case, the 24-species reduced model gives an error of ~20% in the extinction strain rate. Figure 2-5(b) further shows the normalized total mass fraction of C_{4+} species and those of CH_4, C_2H_4 and C_3H_6. The three profiles shown in Figure 2-5(b) are calculated with rather different strain rates that span from strongly burning to near-extinction conditions. The fuel cracking behaviors are quite similar for all three strain rates and they are also similar to those computed for auto-ignition and PSR as shown in Figure 2-2. Specifically, the C_{4+} species primarily vanish by about 1500 K, indicating that the fuel cracking process is completed in the preheat zone before the main flame zone.

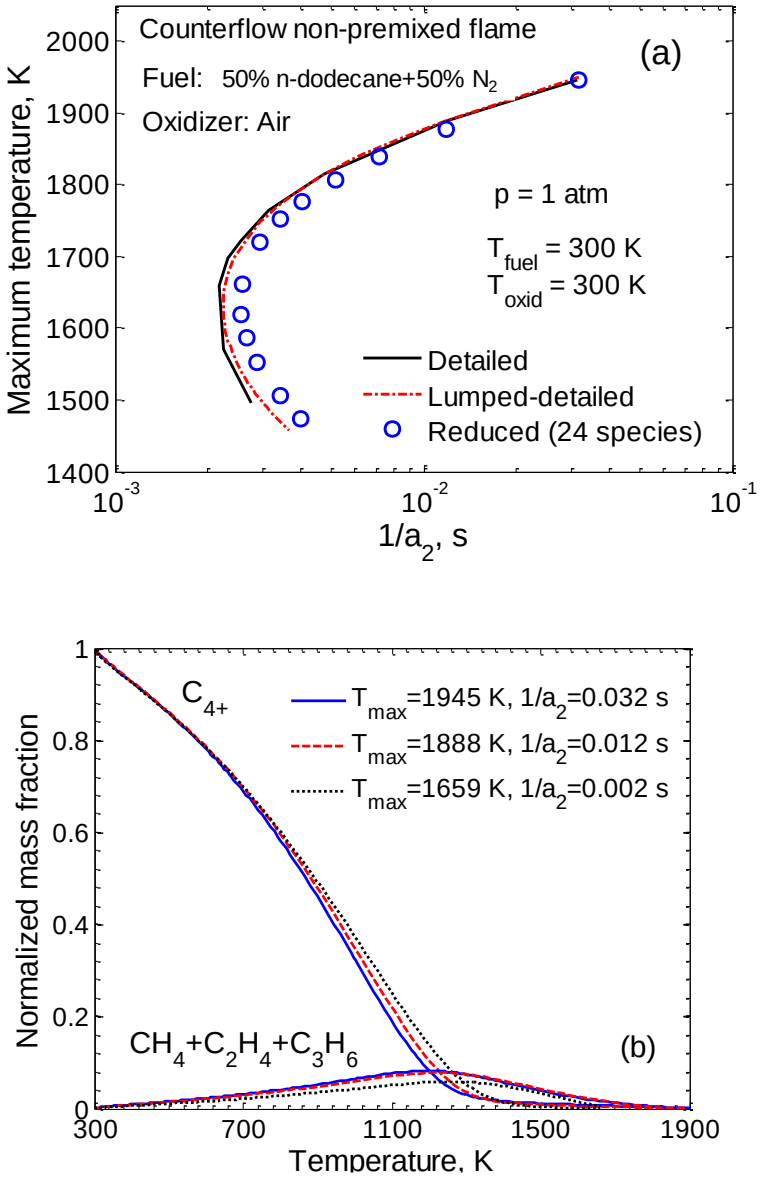

Figure 2-5. (a) Comparison of the maximum temperature T_{max} in counterflow non-premixed flames as a function of the strain rate, calculated with the detailed, lumped-detailed and 24-species reduced models; (b) Normalized total mass fraction of C_{4+} species, and that of the primary fuel cracking products, including CH_4, C_2H_4 and C_3H_6, at three different strain rates as predicted by the detailed model. The flames are at atmospheric pressure and an inlet temperature of 300 K with the fuel jet comprised of 50% (mol) *n*-dodecane in N_2 and air at 300 K as the oxidizer jet.

In the premixed counterflow flames studied, the twin jets are comprised of an *n*-dodecane/air mixture with an equivalence ratio of 0.7 at a temperature of 300 K and atmospheric pressure. Figure 2-6 shows the variation of the maximum temperature as a function of strain rate. Again, predictions using both the lumped-detailed and 24-species reduced models are close to that of the detailed model, including those near the extinction state. The largest discrepancies are observed at low strain rates due to the high sensitivity of flame temperature to the location of the flames and consequently the heat loss rate to the burner inlets. The normalized mass fraction of species C_{4+} and that of the primary fuel cracking products including CH_4, C_2H_4 and C_3H_6 are shown in Figure 2-6(b) as a function of temperature for three strain rates. Comparison of the premixed and non-premixed results shows similar features. In all cases, fuel cracking is complete before 1500 K. Overall, the lumping approach is valid in predicting combustion responses of *n*-dodecane under near-extinction conditions.

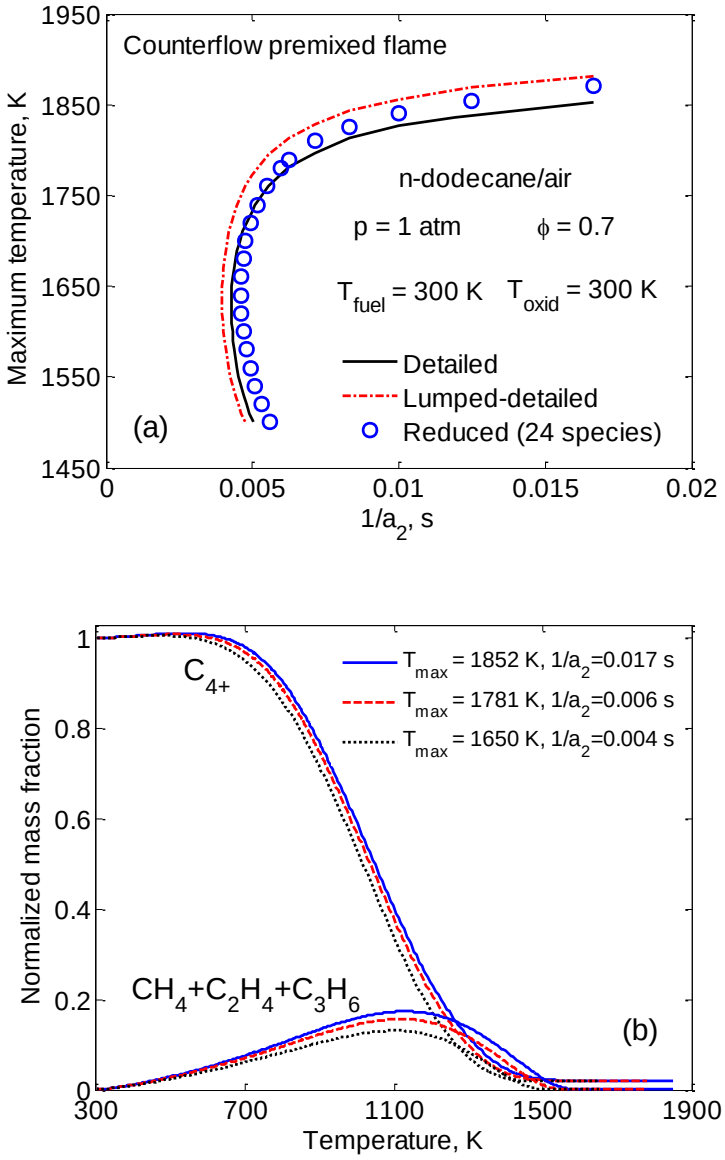

Figure 2-6. (a) Comparison of maximum temperature T_{max} in counterflow premixed flames as a function of the strain rate, calculated with the detailed, lumped-detailed and 24-species reduced models; (b) Normalized total mass fraction of C_{4+} species, and that of the primary fuel cracking products, including CH_4, C_2H_4 and C_3H_6, at three different strain rates as predicted by the detailed model. The flames are at atmospheric pressure and an inlet temperature of 300 K with the twin jets composed of an *n*-dodecane/air mixture at $\phi = 0.7$.

Lastly, it is noted that the C_0-C_3 core of the current 24-species reduced model differ from the 22-species reduced model of ethylene combustion [93] by only three species, namely HCCO, CH_2CO and CH_3CHO that are replaced by CH_2CHO and C_2H_3CHO in the current *n*-dodecane model. The implication is clear, in that it is reasonable to expect that the present model reduction approach is applicable to the high-T oxidation of most of the large hydrocarbons and their mixtures. The resulting reduced models will have sizes comparable to that of ethylene oxidation that involves only 20 to 30 species. With this model size large-scale turbulent flame simulations are well within our reach for practical liquid fuels.

2.3 Fuel cracking in DNS of a turbulence premixed flame

To further investigate the fuel cracking effects in a turbulent environment, 2-D DNS is performed by Dr. S. Lyra at Sandia for a '2D-turbulent' premixed flame of *n*-butane/air. *n*-Butane is selected because it is the smallest *n*-alkane that features similar fuel cracking behavior exhibited in large *n*-alkanes, while the model size is suitable for DNS. To facilitate the DNS, a 25-species reduced model for *n*-butane/air is developed in the present study from the 111-species detailed USC-Mech II using a similar procedure for the reduced *n*-dodecane model. Specifically, the detailed model was first reduced to a 36-species skeletal model using DRG and DRGASA. The skeletal model was further reduced to a 25-species reduced model with the LQSSA method. The reduction was performed for fuel lean conditions spanning an equivalence ratio range, ϕ = 0.6-0.9, pressures of 1-5 atm, initial temperatures of 1000 to 1600 K for auto-ignition, and an inlet temperature of 300K for PSR. In DRGASA, auto-ignition delay and extinction residence time of PSRs were selected as the target responses with an error tolerance of 20%. Validations of the reduced model against the skeletal and detailed models are shown in Figure 2-7, including ignition delay, PSR extinction, and the laminar flame speed.

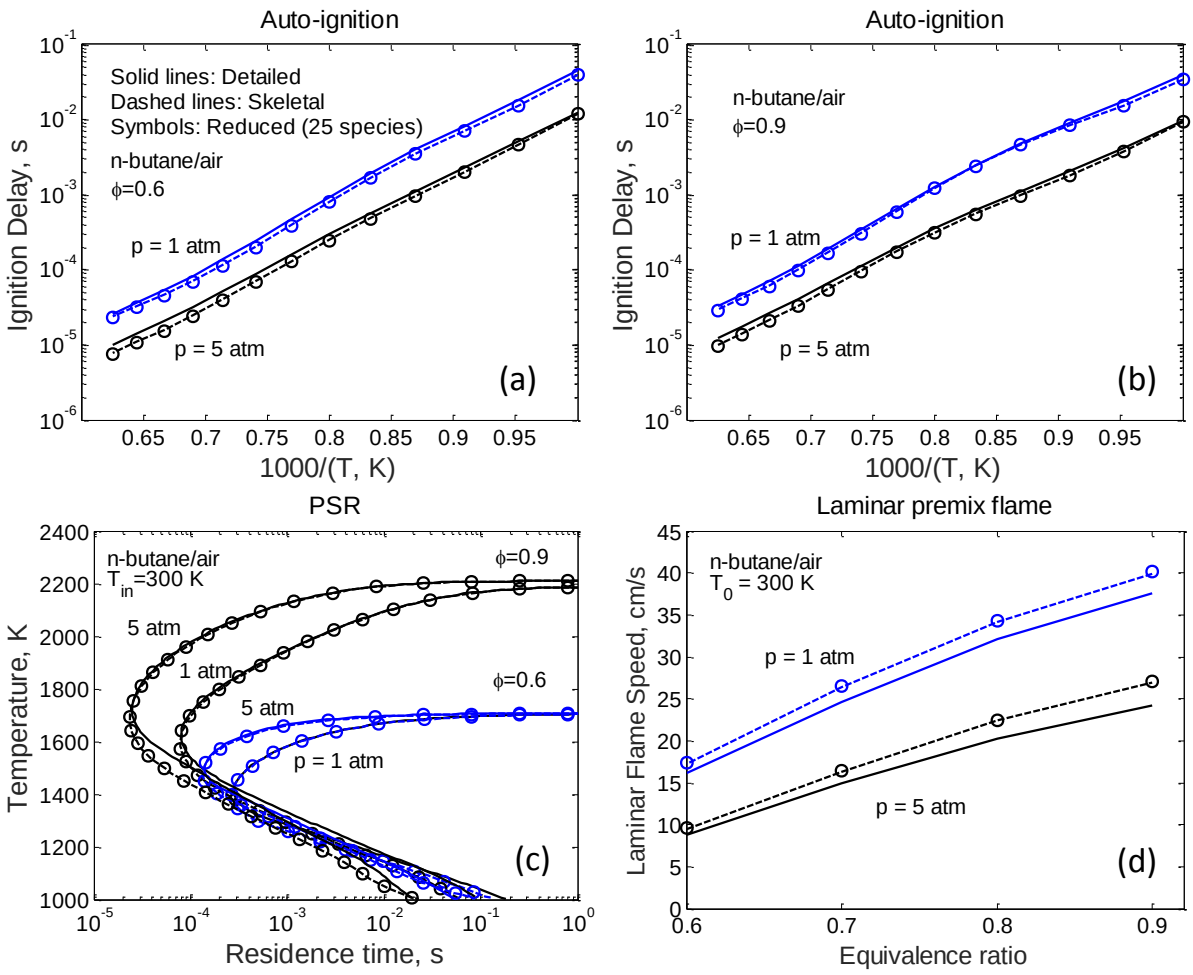

Figure 2-7. Ignition delays, PSR extinction and laminar flame speed for *n*-butane/air mixtures at equivalence ratios of ϕ = 0.6 - 0.9 and pressures of 1 and 5 atm, calculated with the detailed, skeletal, and reduced models.

The 25-species reduced model is then applied in DNS of a 2-D turbulent premixed flame of *n*-butane/air using Sandia's DNS code, S3D [3], which solves the compressible Navier-Stokes, total energy and species conservation equations using a high order, low-dissipative finite difference scheme. A fourth-order explicit Runge-Kutta scheme [94] is used for time integration with chemical stiffness removed on-the-fly [95]. An eighth-order central differencing scheme is applied for spatial discretization, and a tenth-order filter is employed to remove high-frequency

waves in the spatial profiles [29]. The CHEMKIN subroutines are employed to evaluate reaction rates, thermodynamic properties and mixture-averaged transport [57, 96]. The computational domain is 10 mm (x) by 15 mm (y) discretized with a uniform grid size of 5 μm. Periodic boundary conditions are applied in the x-direction and non-reflecting outflow boundary conditions are applied in the y-direction. The flame is propagating into fresh mixtures of an equivalence ratio ϕ = 0.6 at a temperature of 500 K and pressure of 5 atm. The flow field is initialized with a 1-D premixed flame solution with a laminar flame speed of 29.9 cm/s and thermal flame thickness of 0.14 mm. The initial flame configuration is shown in Figure 2-8(a). A spectrum of isotropic turbulence is imposed on the initial flow field with an integral length of l = 2.1 mm and velocity fluctuation u' = 20.9 m/s, resulting in a turbulence Reynolds number of Re_t = 1000 and a Karlovitz number of Ka = 250 as denoted in the Borghi diagram in Figure 2-8(b).

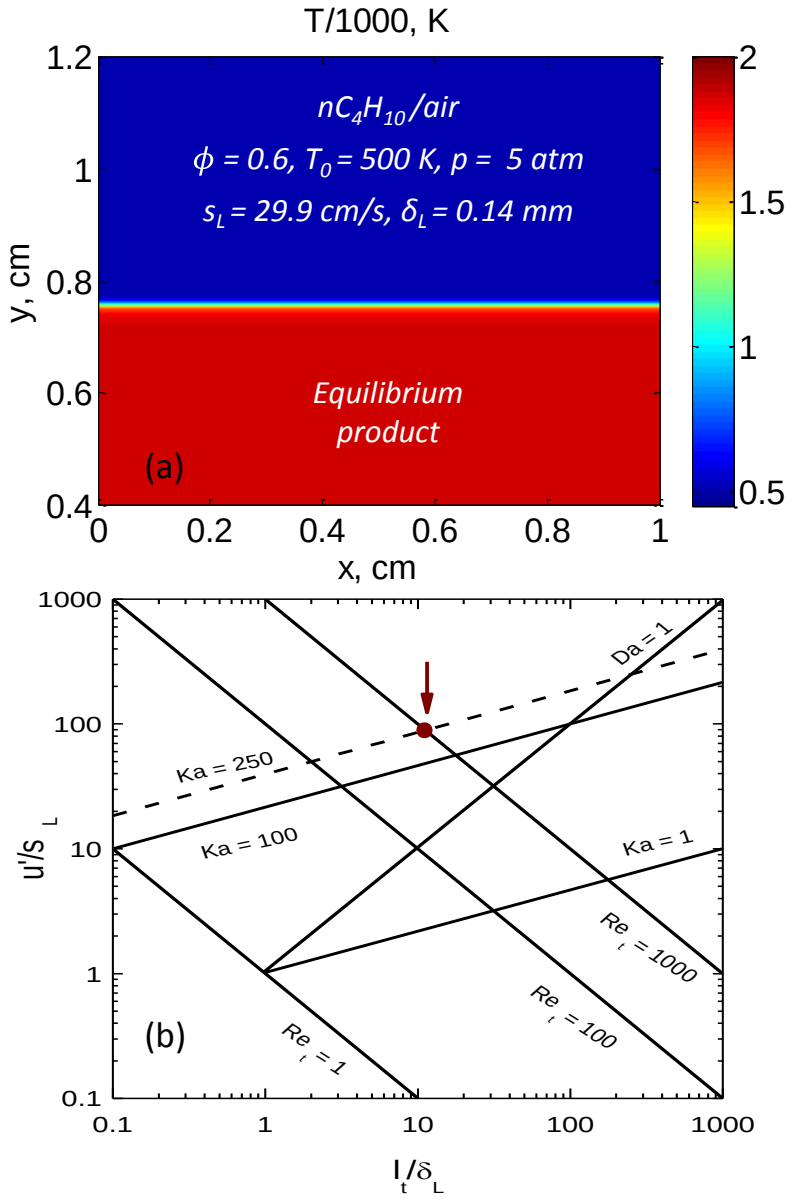

Figure 2-8. (a) Initial temperature isocontour for the 2-D DNS of *n*-butane/air, and (b) location of the DNS case on the Borghi diagram (Ka = 250, Re_t = 1000), courtesy of Dr. S. Lyra.

Although the DNS was performed in two dimensions for computational efficiency, the flame structure obtained is consistent in the energy-containing scales with three-dimensional turbulent simulations. The fine-scale mixing is likely to differ between the 2-D and 3-D turbulence; however, heat release and viscous dissipation effects will dampen the intensity of eddies,

particularly small eddies in the dissipative end of the turbulent kinetic energy spectrum as demonstrated from earlier flame-vortex simulations [97] such that wrinkling of the flame will be achieved predominantly by energy-containing eddy scales. The flame structure at different time instances are shown in Figure 2-9, with the left panels showing the isocontour of fuel mass fraction. The white isolines indicate the flame zone location identified using chemical explosive mode analysis (CEMA) [93, 98, 99], which is a systematic approach to detect ignition, extinction and premixed flame fronts locations in complex flow fields. It is seen that the flame fronts are significantly disturbed by the strong turbulence at the different time instances. However, a buffer is always present between the flame zone and the regimes with high concentration of fuel, indicating that the concentration of fuel molecules that enter into the flame zone is negligible even in the highly turbulent environment. The scatter plots of mass fractions of fuel and primary fuel cracking products, C_2H_4 and C_3H_6, in the right panels show that the fuel cracking behavior at the intense turbulence condition resembles that in 1-D laminar flames indicated by the solid lines, and the fuel cracking is essentially completed by approximately 1500 K, before reaching the flame zone. Note that, CH_4 is not present in the reduced *n*-butane model. This observation on fuel cracking is consistent with that obtained from the lower-dimensional 0-D and 1-D systems.

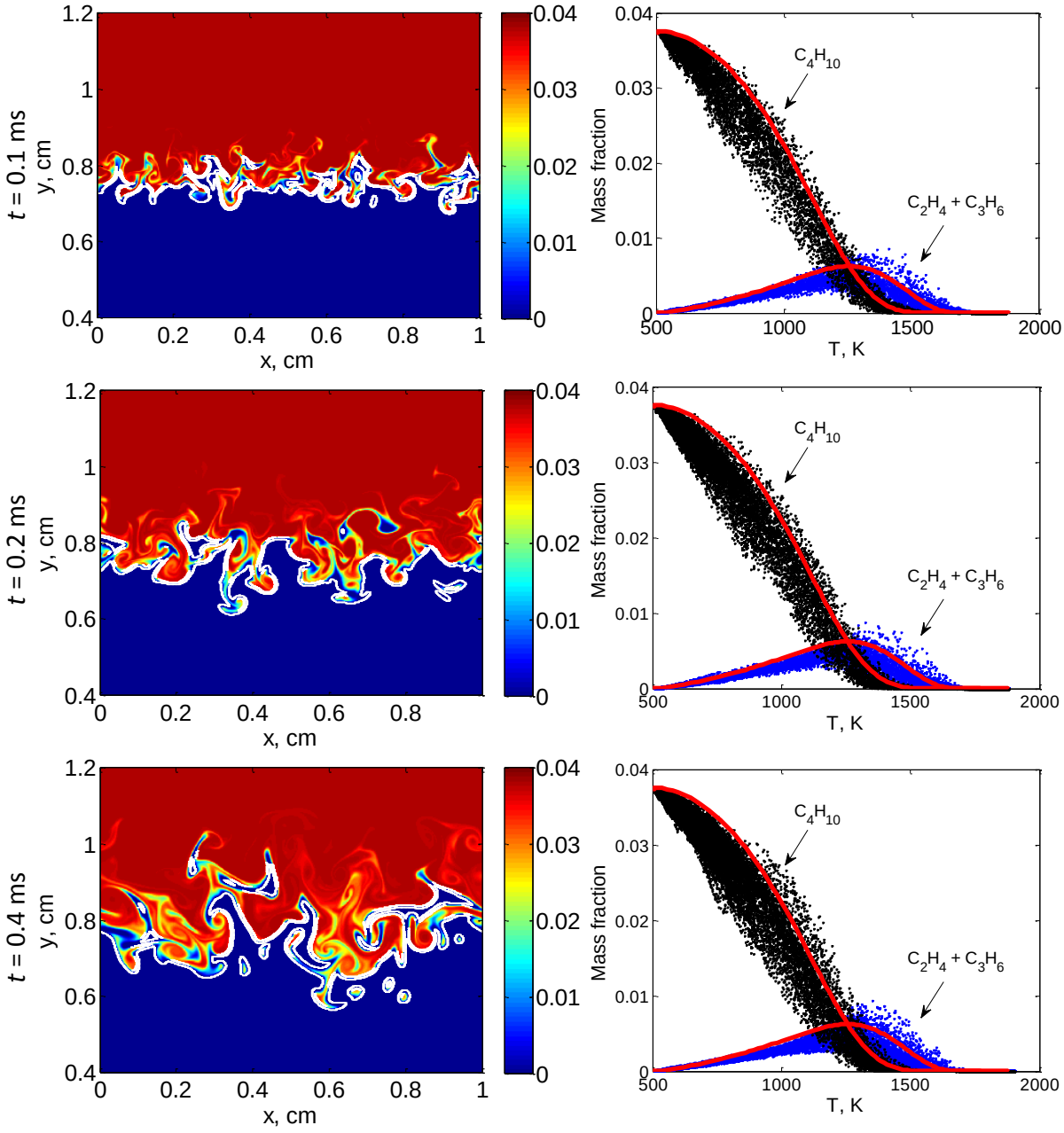

Figure 2-9. Left panels: Isocontour of fuel mass fraction (red: fresh mixture, blue: hot products), and right panels: scatter plots of mass fractions of fuel and primary cracking products vs. temperature, for DNS of a turbulent premixed flame of *n*-butane/air at different time instances. The white isolines on the left panels show the flame zone identified using CEMA. The solid lines

on the right panels are solutions from 1-D steady state premix flame with the same fresh mixture condition as that in the DNS.

2.4 Concluding remarks

In this chapter, a 24-species reduced model with lumped fuel cracking steps for high-T oxidation of *n*-dodecane is developed. The reduced model yields satisfactory results compared to the detailed model, and the lumped approach is shown to work well for predicting key combustion responses, including auto-ignition, PSR extinction, laminar flame speed, and laminar premixed and non-premixed flame extinction.

A 25-species reduced model for *n*-butane is developed for a DNS study of turbulent flames. Analysis of the 2-D DNS shows that an insignificant amount of fuel molecules enters the flame zone, even at the strongly turbulent environment, and thus the flame zone behavior is primarily controlled by oxidation of the fuel cracking products.

The above observations all support the approach of lumping fuel cracking into a few short steps as the means to reduce the chemical complexity of the model and to reduce the model size efficiently. Coupled with a detailed foundational fuel model of H_2, CO, and $C_{\leq 4}$ species, the resultant hybrid model can accurately predict the important high-T combustion behaviors.

Chapter 3 Reduced High-Temperature Kinetic Models of Real Jet Fuels Based on HyChem Models

3.1 Introduction

In Chapter 2, the fast fuel cracking assumption has been extensively investigated and shown to be valid in 0-D systems including auto-ignition and PSR, 1-D laminar flames, and a 2-D turbulent premixed flame. Recently, a hybrid approach, "HyChem," was proposed by the Stanford team by Prof. Hai Wang to model high-temperature combustion of real jet fuels [100-102], and HyChem models have been developed for multiple real jet fuels. In the HyChem models, the fuel cracking process is described by a "1-species" lumped model and coupled with a detailed foundation fuel chemistry model to describe the oxidation of the cracked fragments. Therefore, the HyChem approach reduces not only the size of jet fuel reaction models but also the underlying chemical complexities and uncertainties.

To utilize the chemistry efforts in large scale high-fidelity CFD simulations, model reduction is a bridge in between. In previous studies, various reduced and skeletal models for jet fuel surrogates, *e.g.* neat *n*-dodecane, have been developed in previous studies. A skeletal *n*-dodecane model with 105 species was developed for spray combustion applications [103], a 24-species lumped-reduced *n*-dodecane model was developed for high-T combustion based on a lumped-detailed JetSurF model in Chapter 2, and a compact 54-species skeletal model for *n*-dodecane with optimized semi-global low-temperature chemistry was developed for diesel engine simulations [104].

The emphasis of this chapter is the reduction of the foundational fuel chemistry model in HyChem models for real jet fuels. In particular, compact reduced models are developed based on the HyChem models for three real jet fuels to obtain CFD-amenable models for more efficient

simulations. Three target fuels are included in this study, including a conventional petroleum-derived Jet-A fuel (POSF10325, Cat A2), and two alternative jet fuels: one (POSF11498, Cat C1) features a low derived cetane number (DCN) and is composed of highly branched *iso*-alkanes, and the other (POSF12345, Cat C5) features similar chemical properties but vastly different physical properties (flat boiling curve) with Cat A2. The key aspects of these three fuels are listed in Table 3-1. More details of the fuels can be found in Refs. [105, 106]. For simplicity, the three fuels are designated as A2, C1, and C5 henceforth.

Table 3-1. Summary of the target fuels in the present study

Fuel ID	Key aspects	Fuel composition
A2/POSF10325	average/nominal, Jet A	$C_{11}H_{22}$
C1/POSF11498	highly-branched *iso*-paraffinic kerosene, extremely low cetane, unusual boiling range	$C_{13}H_{28}$
C5/POSF12345	very “flat” boiling range	$C_{10}H_{19}$

The remainder of this chapter is organized as follows. The development of fuel-specific reduced models and a universal reduced model for the target fuels are presented in details. In the following, the reduced models are validated comprehensively in 0-D and 1-D flames, and a bifurcation analysis is performed to identify the important reactions controlling lean blow-out (LBO) of PSR. Furthermore, the ability of capturing fuel sensitivities with the reduced models is demonstrated.

3.2 Model reduction for the detailed HyChem models

3.2.1 Development of fuel-specific reduced models

The reduction is based on reaction states sampled from auto-ignition and PSR. The reduction parameter range covers pressure of 0.5-30 atm, equivalence ratio of 0.5 to 1.5, initial temperature of 1000-1600 K for auto-ignition, and inlet temperature of 300 K for PSR.

Skeletal reduction with DRG [19-22] and DRGASA [13, 16] is first applied to eliminate unimportant species and reactions from the detailed HyChem models. In DRG, H radical is selected as the starting species and an error threshold of 0.3 is specified for all the three target fuels. After the skeletal reduction with DRG, the resulting skeletal models consist of 93, 90, and 96 species for A2, C1, and C5, respectively. The skeletal models are further reduced with sensitivity analysis with ignition delay and extinction residence time of PSR as target parameters. Figure 3-1 shows the accumulative worst-case errors in the target parameters in sensitivity analysis as function of the number of retained species in the skeletal models, with the vertical dashed lines indicating the error thresholds. To ensure the minimum size of the skeletal model with a given error threshold, the threshold is chosen where rapid increase in error starts to occur, that is 20% for A2 and C5, and 35% for C1. The final skeletal models consist of 41, 34, and 41 species for A2, C1, and C5, respectively. Noted that the skeletal model for C1 is smaller than the other two because C1 is primarily comprised of *iso*-alkanes, such that it is not necessary to retain aromatic species as fuel cracking products. As the last step in the skeletal reduction, reactions unimportant for all the remaining species are eliminated by comparing the contribution of each reaction to each species using an error threshold of 20% [22].

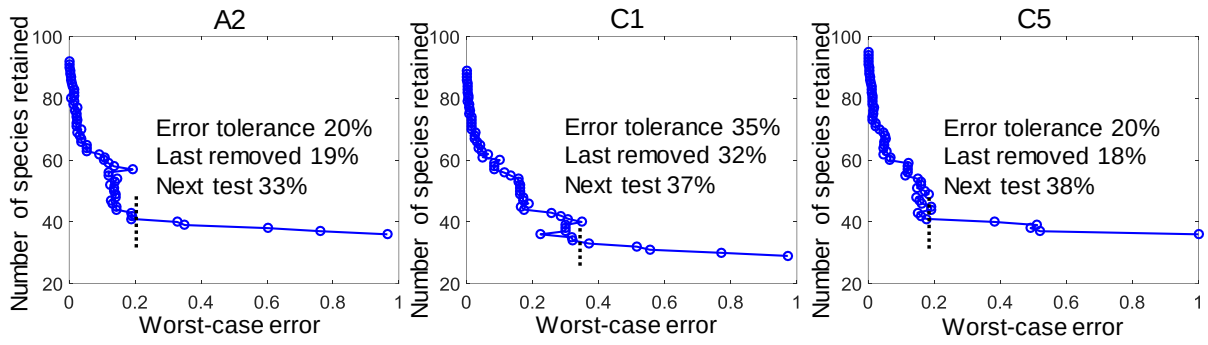

Figure 3-1. Accumulative worst-case errors in the target parameters in sensitivity analysis as function of the number of retained species in the skeletal model for A2, C1 and C5, respectively.

In the second-stage of the reduction, LQSSA [45] are further applied on 10, 8, and 10 global QSS species for A2, C1, and C5, respectively. The QSS species are removed from the transport equations and analytically solved using internal algebraic equations using a graph-based method [45]. Table 3-2 provides the summary of the detailed, skeletal, and reduced models for the three target fuels.

Table 3-2. Sizes of the detailed, skeletal and reduced models

	A2		C1		C5	
	Species	Reactions	Species	Reactions	Species	Reactions
Detailed	119	843	119	843	119	843
Skeletal	41	202	34	182	41	200
Reduced	31	202	26	182	31	200

3.2.2 Development of a universal reduced model

Because the oxidation cores for different jet fuel models are largely identical, a universal skeletal model is proposed by combining the oxidation cores of the target fuels and using programmable fuel properties and fuel cracking reactions. Procedurally, the three skeletal models

are first merged to obtain a universal skeletal oxidation core with 47 species and 263 reactions after removing 37 reactions that are unimportant for all the three fuels. The three target fuels and their fuel-specific cracking reactions are replaced with 1 nominal fuel species and 7 nominal fuel cracking reactions, resulting in a universal skeletal model with 48 species and 270 reactions. The fuel thermal and transport properties, as well as the rates and stoichiometric coefficients of the nominal fuel cracking reactions are evaluated using a special subroutine. Among the 48 species in the universal skeletal model, 13 are identified to be global QSS species, and a 35-species universal reduced model is finally obtained.

3.2.3 A reduced NO sub-model

To enable the NO prediction for the jet fuel models, a complete NO sub-model from GRI-Mech 3.0 [107] and updated by Luo *et al.* [108] is added to the 48-species universal skeletal model. Compared with original GRI Mech 3.0, five reactions were updated and three reactions were added to account for the low temperature NO catalytic effect for fuel oxidation [108]. In addition, C and CH, which are not present in the current universal skeletal model, are added back to capture prompt NO formation. Finally, addition 22 species for NO sub-chemistry are added to the 48-species universal skeletal model, which are: N, NH, NH_2, NH_3, NNH, NO, NO_2, N_2O, HNO, CN, HCN, H_2CN, HCNN, HCNO, HOCN, HNCO, NCO, CH_3O_2, CH_3OH, C, CH, and Ar. The final universal skeletal model with NO sub-chemistry consists of 70 species. The universal skeletal model with NO sub-model is further reduced with sensitivity analysis. NO concentration in PSR is selected as the target with an error threshold 20% to identify the important reaction pathways for NO formation. After the skeletal reduction, 7 species are removed, which are: HCNN, HOCN, HCNO, CN, CH_3O_2, CH_3OH, and Ar, resulting in a final universal skeletal model that consists of 63 species. Compared with the 48-species universal skeletal model without NO, the additional 15 species for

NO sub-chemistry include: NH, NH_2, NH_3, NO, NO_2, N_2O, HNO, HCN, HNCO, NCO, N, NNH, H_2CN, C, and CH. In the last step, LQSSA is applied to 18 global QSS species, finally resulting in a 45-species universal reduced model with NO sub-chemistry.

3.3 Results and discussion

3.3.1 Validations of the fuel-specific reduced models

Figure 3-2 compares the reduced, skeletal, and detailed HyChem models for A2, C1, and C5 in 0-D homogeneous reactors for ignition delay and extinction of PSR, while Figure 3-3 compares the laminar flame speed. For the reduced models of A2 and C5, the worst-case error in flame speed is approximately 1.5 cm/s, while for the reduced model of C1, the flame speed is over-predicted by approximately 3 cm/s near the stoichiometric condition at low pressures. In the comparison of detailed HyChem models with experiments for laminar flame speed [109], while the detailed A2 model agrees quite well with the experiments, the detailed C1 model under-predicts the flame speed at the worst-case about 7 cm/s near the stoichiometric condition. The authors in Ref. [109] suggested that the discrepancy between numerically predicted and experimentally measured flame speed for C1 is due to the foundational fuel chemistry model, especially in the reactions involving *iso*-butene and *iso*-butenyl. Detailed comparison of the model predicted ignition delay, laminar flame speed with experiments can be found in Refs. [101, 109].

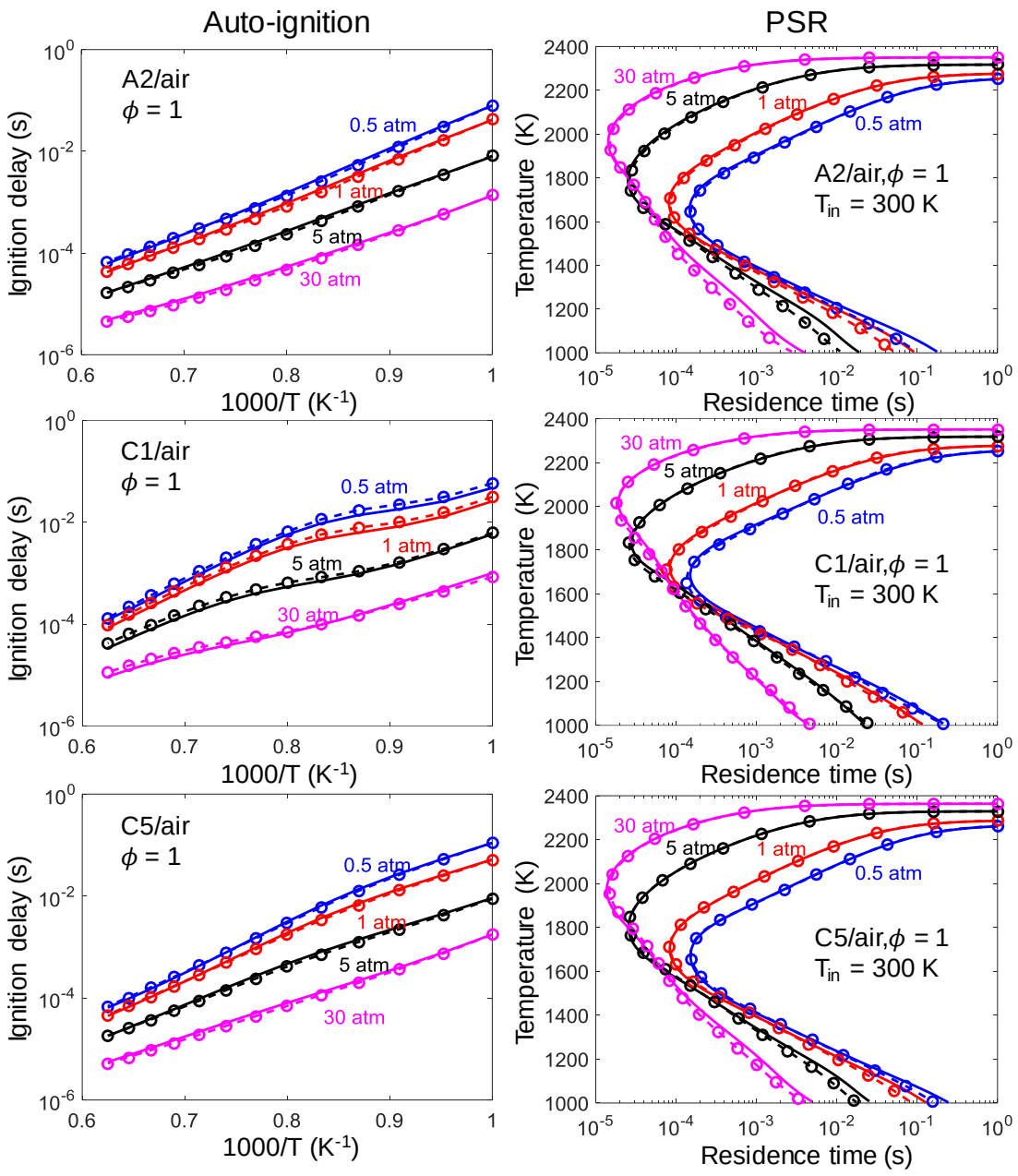

Figure 3-2. Ignition delay (left panel) and temperature profiles of PSR (right panel) for stoichiometric mixtures at pressure of 0.5, 1, 5, and 30 atm for A2, C1, and C5, calculated with the detailed (solid lines), skeletal (dashed lines), and reduced (symbols) models, respectively. Similar agreement is observed for ϕ = 0.5 and 1.5.

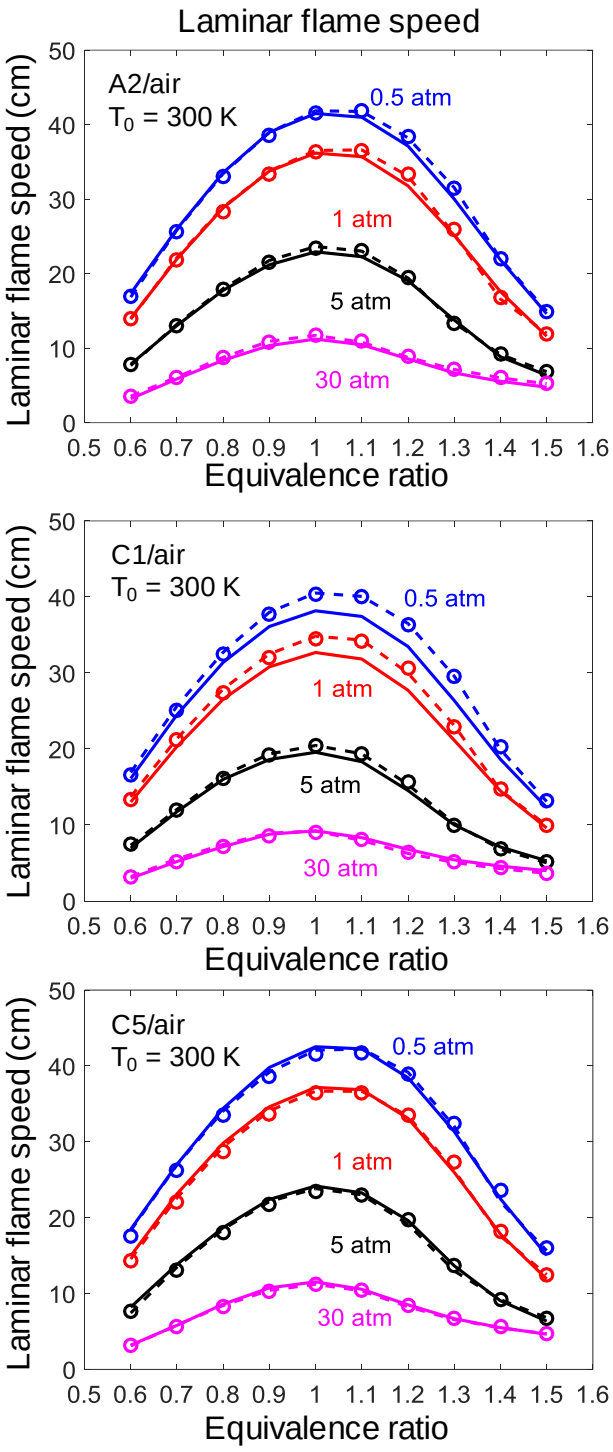

Figure 3-3. Laminar flame speed as function of equivalence ratio at an initial temperature of 300 K and pressure of 0.5, 1, 5, and 30 atm for A2, C1, and C5, calculated with the detailed (solid lines), skeletal (dashed lines), and reduced (symbols) models, respectively.

To further investigate the validity of the reduced models at other flame conditions, flame responses to flow strain are numerically tested in both non-premixed and premixed 1-D counterflow flames. The global strain rate is defined in Eq. (2-1). For non-premixed flames, both inlet streams are at temperature of 300 K and pressure of 1 or 10 atm. The fuel stream is comprised of fuel (50% in mole) and N_2, flowing against the air stream. The premixed counterflow flames involve identical inlet conditions, and thus are symmetric twin flames, at equivalence ratio of 0.7, temperature of 300 K, and pressure of 1 or 10 atm. Figure 3-4 shows the maximum temperature of the flame as function of the reciprocal strain rate for non-premixed flames (left panel) and premixed flames (right panel), respectively. The reduced models agree tightly with the detailed models along the *S*-curves including the turning points, which are the nominal extinction states of the flames, with the worst-case relative error in the extinction strain rate being smaller than 15% for non-premixed flames and approximately 16%, occurring in C1, for premixed flames.

3.3.2 Validation of the universal reduced model

Figure 3-5 shows the validation of the 35-species universal reduced model for A2, C1, and C5 against the detailed models for ignition delay and temperature profiles of PSR. Figure 3-6 compares laminar flame speed. The universal model is seen to be more accurate than the fuel-specific models, particularly for C1 in the prediction of laminar flame speed.

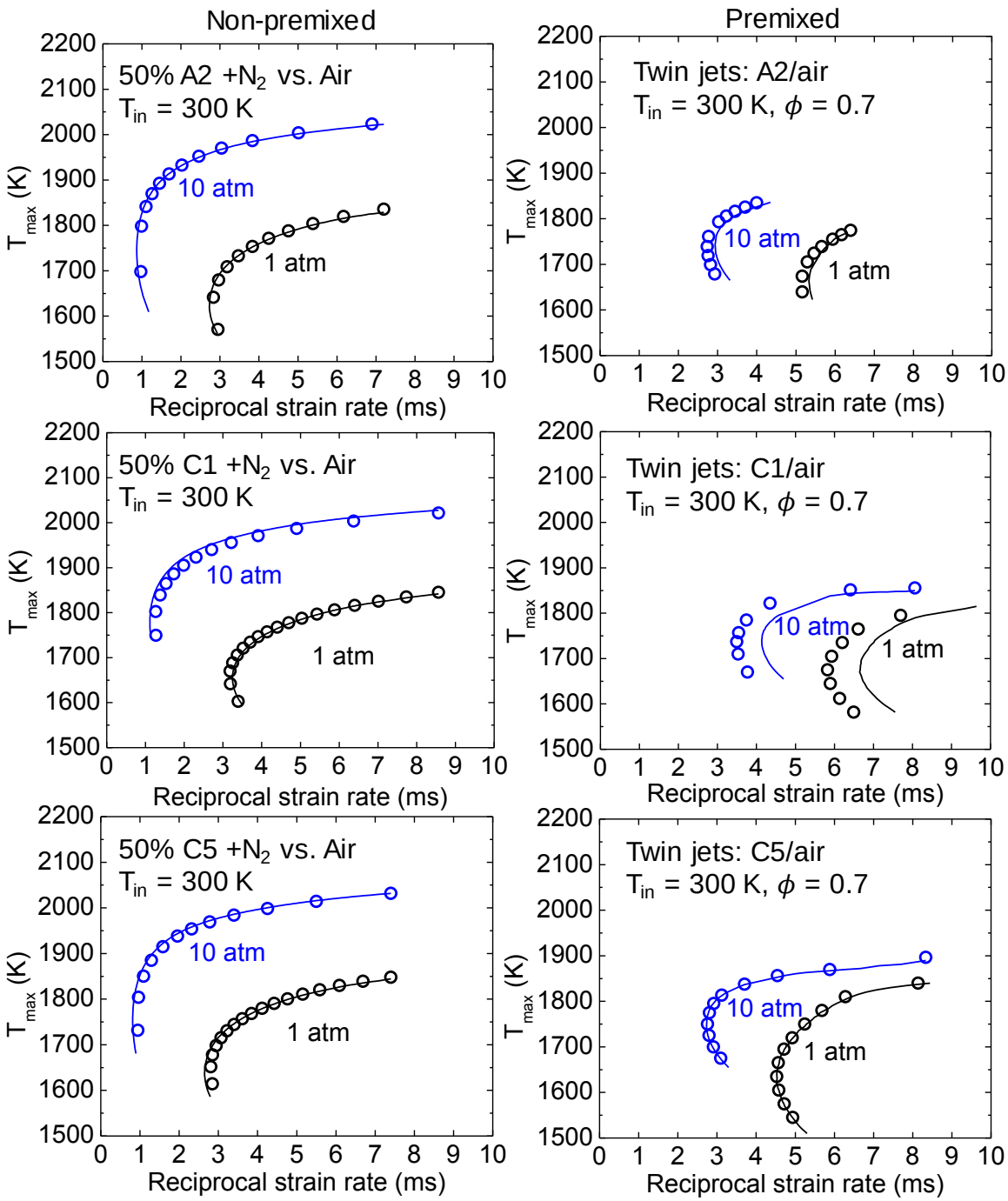

Figure 3-4. Comparison of the maximum temperature T_{max} in counterflow non-premixed (left panel) and premixed flames (right panel) as function of the reciprocal strain rate, calculated with the detailed (solid lines) and reduced (symbols) models, respectively.

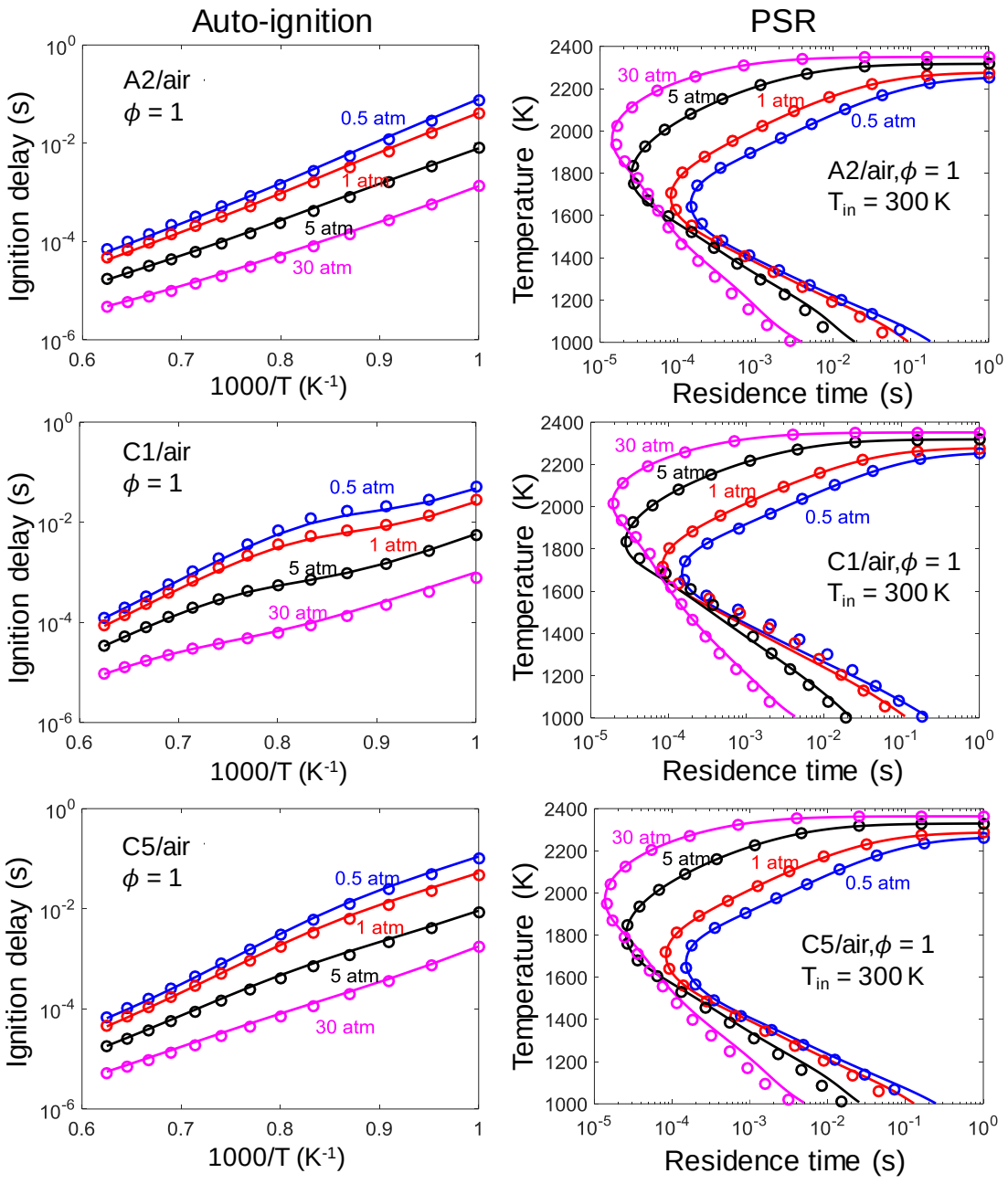

Figure 3-5. Ignition delay (left panel) and temperature profiles of PSR (right panel) for stoichiometric mixtures at pressure of 0.5, 1, 5, and 30 atm, calculated with the detailed (solid lines) and reduced (symbols) models, respectively. Similar agreement is observed for ϕ = 0.5 and 1.5.

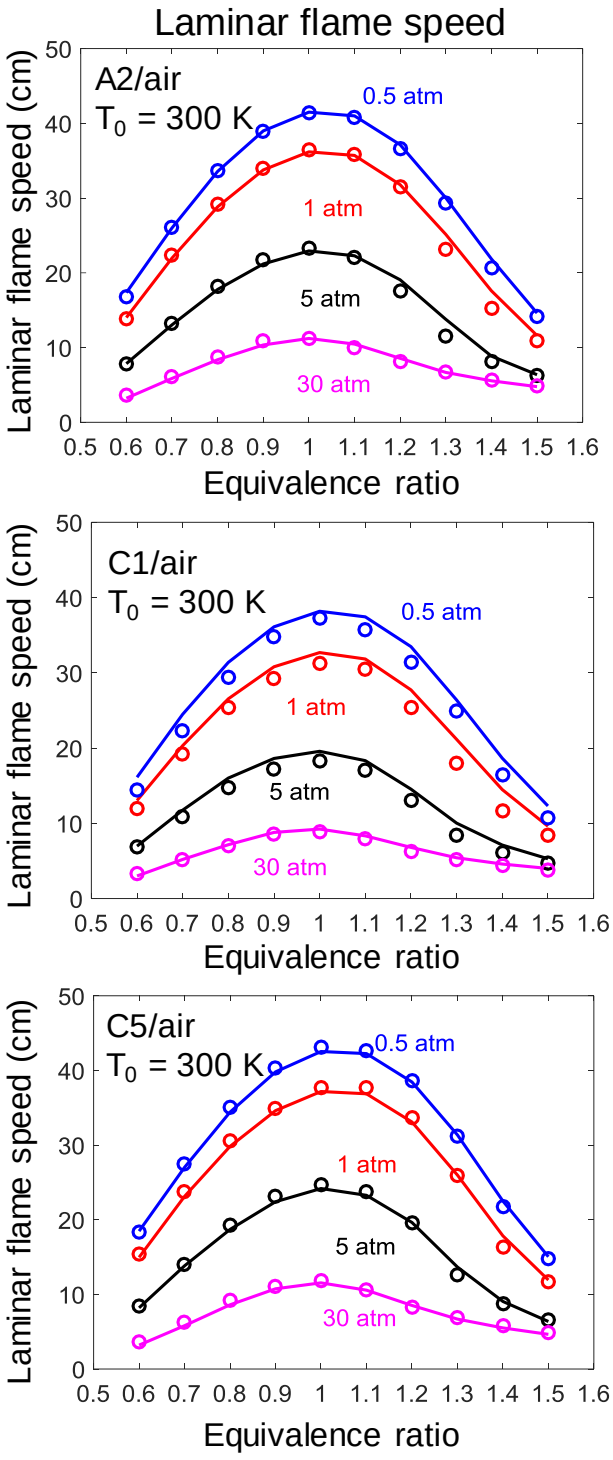

Figure 3-6. Laminar flame speed as function of equivalence ratio at an inlet temperature of 300 K and pressure of 0.5, 1, 5, and 30 atm, calculated with the detailed (solid lines) and reduced (symbols) models, respectively.

3.3.3 Validation of the universal reduced model with NO

In order to validate the universal reduced model with NO sub-chemistry, the complete NO sub-chemistry is also added to the detailed HyChem models for comparison. The 45-species universal reduced model with NO sub-chemistry is validated in PSR and 1-D laminar premixed flames against the detailed HyChem model with the complete NO sub-chemistry. Comparison of NO mole fractions are plotted in Figure 3-7. Good agreements are observed between the universal reduced and detailed models.

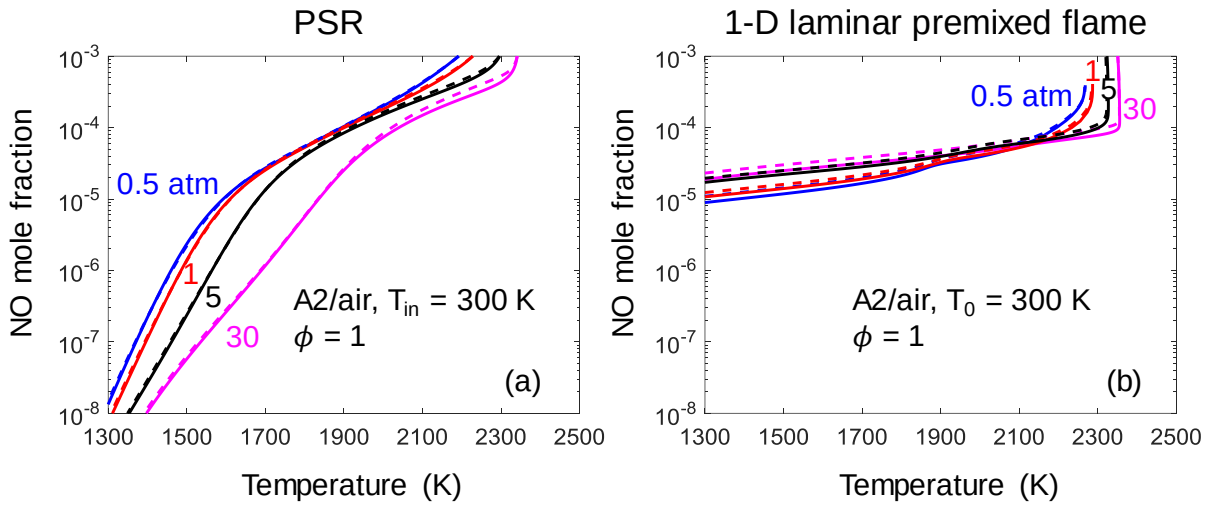

Figure 3-7. Comparison of NO mole fractions in (a) PSR and (b) 1-D laminar premixed flame for A2/air mixture at stoichiometric condition for pressures of 0.5, 1, 5, and 30 atm. Solid lines: detailed HyChem model for A2 with the complete NO sub-model. Dashed lines: 45-species universal reduced model with NO.

3.3.4 Validation for lean blow-out (LBO) of PSR

LBO is a critical issue to jet engine operation and involves complicated physical processes, *e.g.* spray, evaporation, and chemical processes, *e.g.* combustion, and the combustor geometry. Predicting LBO limit through numerical simulations is challenging due to its transient nature.

Some empirical correlations, *e.g.* Lefebvre correlation [110], have been used to estimate and compare the LBO limits. The Lefebvre correlation involves the effects of combustor design, operating conditions, and chemistry which is accounted only through the heat of combustion. The fuel effects on each process are accounted independently, without considering non-linear couplings between physical and chemical processes, and the effects of chemical kinetics are not included. In a recent study by Esclapez *et al.* [111], the fuel effects on LBO in a realistic gas turbine combustor have been studied via LES, the comparative performances of A2, C1, and C5 were investigated under stable combustion conditions near LBO and transient conditions during LBO. While good agreements between measured and predicted LBO trends were obtained for A2 and C5, the LBO limit of C1 predicted by LES differed from the experiments. The authors suggested that further studies to evaluate the sensitivity with respect to the sub-models employed in the study are needed, and the spray is expected to be major source of uncertainty. In the study of Stachler *et al.* [112], LBO of conventional and surrogate jet fuels were investigated in a Well-Stirred Reactor (WSR). The authors found that the LBO for C1 occurs at a higher equivalence ratio and a higher temperature than other test fuels (*e.g.* A2 and C5), indicating C1 is less resistant to LBO. In addition, LBO was found to show the strongest correlation with DCN in the WSR, indicating ignition delay may play a role in LBO under lean premixed conditions.

While discrepancies are found in numerical simulations and experiments [111, 112], fundamental study of LBO in simple reactors without complicated sub-models is necessary to

scrutinize the controlling factors. In the present study, PSR is employed to validate the reduced models under near-LBO conditions taken from Colket *et al.* [113] as listed in Table 3-3, and to examine the controlling processes of LBO. Note that the kinetics effects can be seen clearly with the simple mixing process in PSR. The extinction profiles of PSR under these conditions are shown in the left panels of Figure 3-8 for the detailed and fuel-specific reduced models. Under all the conditions, the reduced models agree very well with the detailed models along the entire curves, including the turning points, which are the extinction states in PSR. The good agreement demonstrates the capability of capturing LBO behaviors accurately with reduced models. In addition, using a bifurcation analysis [114-116] for the extinction states of PSR with the detailed models, the most important reactions controlling the extinction states are identified in the right panels of Figure 3-8 based on the bifurcation index (BI) values, which are the normalized contributions of the reactions/mixing to the zero-crossing of the eigenvalue associated with the extinction states. Note that, all of the important reactions listed are also contained in the reduced models. It is seen in the right panel of Figure 3-8, the LBO for the four different cases and three different fuels are mostly controlled by the same set of reactions involving only small molecules, such as H, OH, O_2, HCO, CO and CO_2, and the competition between two groups of reactions with opposite signs largely determines the extinction state, while mixing only competes with the overall reaction which is weakened by the internal competition between the chain termination reaction, $H+O_2(+M)\rightarrow HO_2(+M)$, the chain branching reaction, $H+O_2\rightarrow O+OH$, and heat release, $CO+OH\rightarrow CO_2+H$. This observation is consistent with the finding for *n*-dodecane in a previous study [117].

Table 3-3. Near-LBO conditions for PSR

LBO conditions	T_{in}, K	p, atm	ϕ
Case 1	394	2.04	0.457
Case 2	394	3.4	0.456
Case 3	450	2.04	0.435
Case 4	450	3.4	0.434

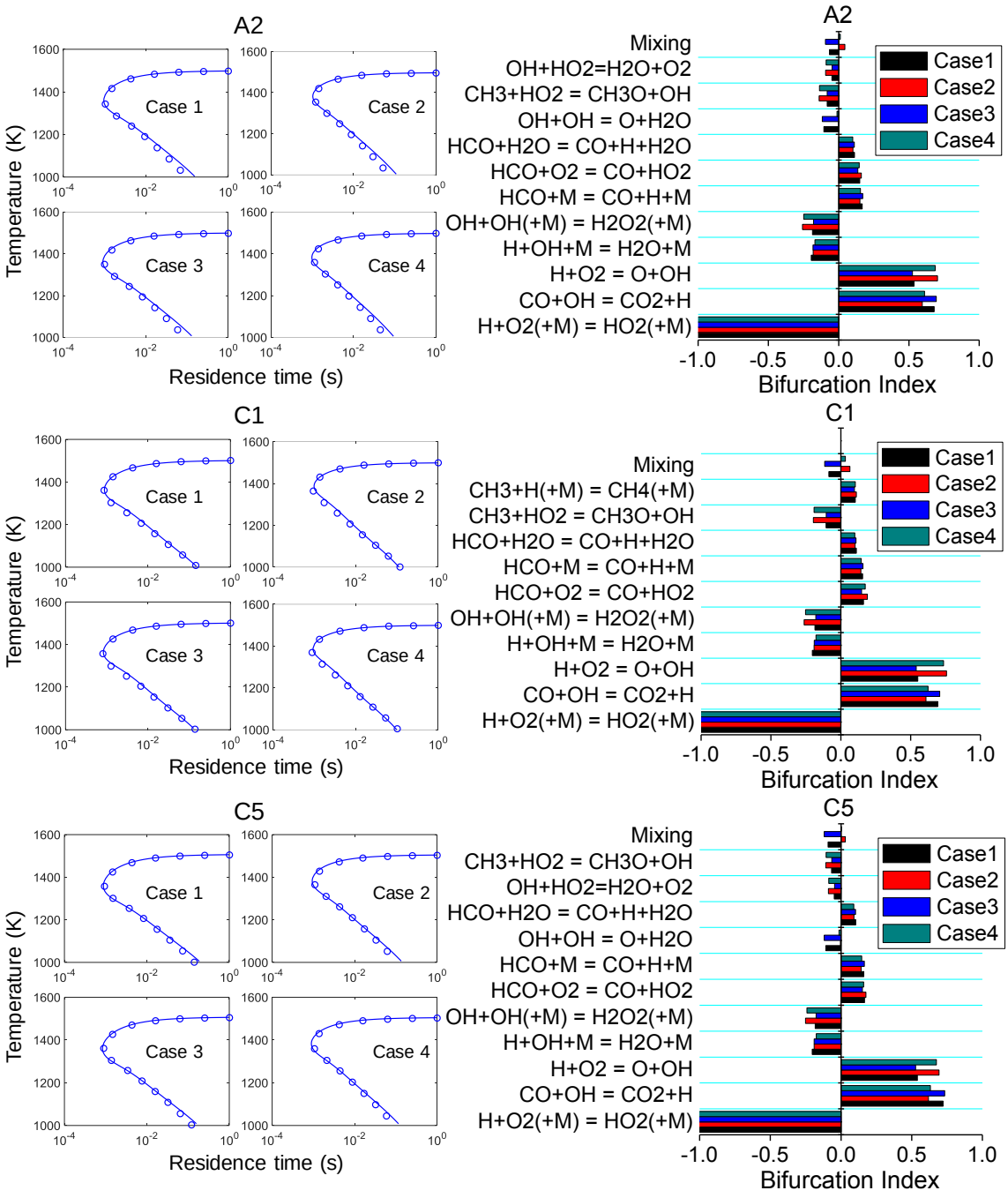

Figure 3-8. Left panels: Temperature profiles of PSR for A2, C1, and C5 under the four conditions listed in Table 3-3, calculated with the detailed (solid lines) and fuel-specific reduced (symbols) models, respectively. Right panels: Important reactions for the LBO of PSR based on the BI values for the four conditions in Table 3-3 for A2, C1, and C5.

Numerically and experimentally, the LBO limit is typically obtained by reducing the equivalence ratio until the flame is extinguished. To mimic this process in PSR, the residence time as well as pressure and inlet temperature are fixed, but vary the equivalence ratio, to obtain the LBO limits of equivalence ratio. Temperature profiles with respect to different equivalence ratios, which are characterized as *O*-curves, are plotted for A2 in Figure 3-9 for three different given residence time τ under the four conditions given in Table 3-3. The left turning points with minimum equivalence ratios correspond to the LBO limits. The reduced model agrees closely with the detailed model including the turning points., which again shows the capability of capturing LBO kinetics.

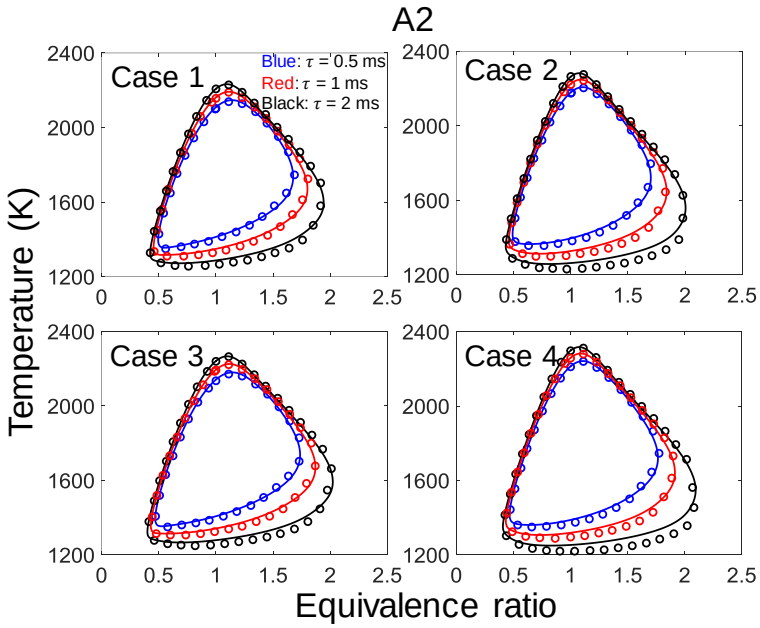

Figure 3-9. Temperature profiles of PSR as function of equivalence ratios for A2 with different residence time τ under the four conditions given in Table 3-3, calculated with the detailed (solid lines) and fuel-specific reduced (symbols) models, respectively. Similar agreement is observed for C1 and C5.

3.3.5 Fuel sensitivities of the reduced models

The relative combustion performance of different jet fuels is very important for fuel selection. Hence, the reduced models must be able to capture the fuel sensitivities from the detailed models, *i.e.* the reduction process should predict the correct relative trends in critical flame features for the different fuels. The fuel sensitivities of the reduced models are compared with the detailed models in 0-D and 1-D systems in Figure 3-10 and Figure 3-11. It is seen that the reduced models capture the fuel sensitivities in the detailed models very well.

For the ignition delay, as discussed in [102, 109], C1 ignites faster than A2 and C5 in the temperature region of 1000-1200 K, while it ignites slower than A2 and C5 at temperature over 1300 K by a factor about 2-4. The ignition delay of jet fuels is mainly affected by two processes with different timescales: the fuel decomposition and the oxidation of pyrolysis fragments. At lower temperatures, fuel decomposition controls the ignition delay. Because the overall rate of C1 pyrolysis is faster than A2, the ignition delay is shorter than A2. At higher temperatures, the oxidation of pyrolysis fragments controls the ignition delay. Because the pyrolysis of C1 yields more *i*C_4H_8 while A2 yields more C_2H_4, and the oxidation of *i*C_4H_8 is slower than C_2H_4, the ignition delay of C1 becomes longer than A2. A more detailed comparative study of combustion chemistry of A2 and C1 can be found in Refs. [102, 109]. For the extinction of PSR, the fuel sensitivity is not obvious under the tested conditions. The three target fuels almost overlap over the entire curves. This is due to the fact that, the important reactions which control the extinction of PSR only involve the small molecules, such as H, OH, O_2, HCO, CO and CO_2, as discussed in the LBO section. For the laminar flame speed, the relative trends predicted by the detailed models are also well captured by the reduced models.

To further investigate the fuel sensitivities in the reduced models in diffusive flames, Figure 3-11 compares the extinction of 1-D counterflow flames using the detailed and fuel-specific reduced models, respectively. The turning points are the extinction states. For the extinction of non-premixed counterflow flames (top panel), A2 and C5 have very close extinction strain rates, while C1 is extinguished at a smaller strain rate, or a larger reciprocal strain rate. In other words, C1 is less resistant to flow strains compared with A2 and C5 in non-premixed counterflow flames. In premixed counterflow flames (bottom panel), the fuel sensitivities become more noticeable at atmospheric pressure. Similar with non-premixed counterflow flames, C1 still has a smaller extinction strain rate than A2 and C5 in premixed counterflow flames. In addition, combined with the LBO study in PSR, where kinetics effects are found to be the similar for three fuels, the fuel sensitivities in the 1-D counterflow extinction may be attributed to the diffusion or other flow processes.

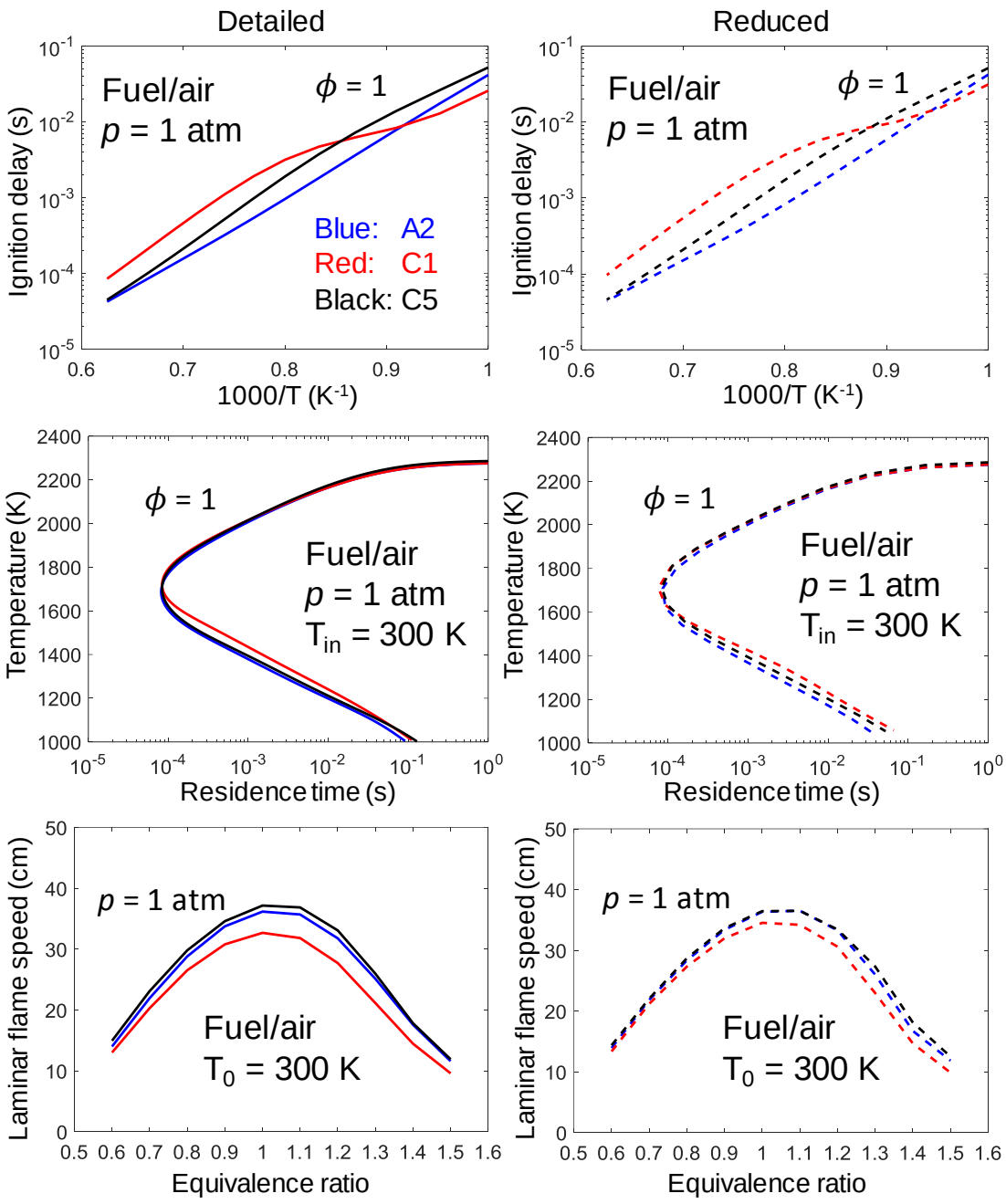

Figure 3-10. Fuel sensitivities in auto-ignition (top panel), temperature profiles of PSR (middle panel), and laminar flame speed (bottom panel) for detailed (left panel, solid lines) and reduced (right panel, dashed lines), respectively.

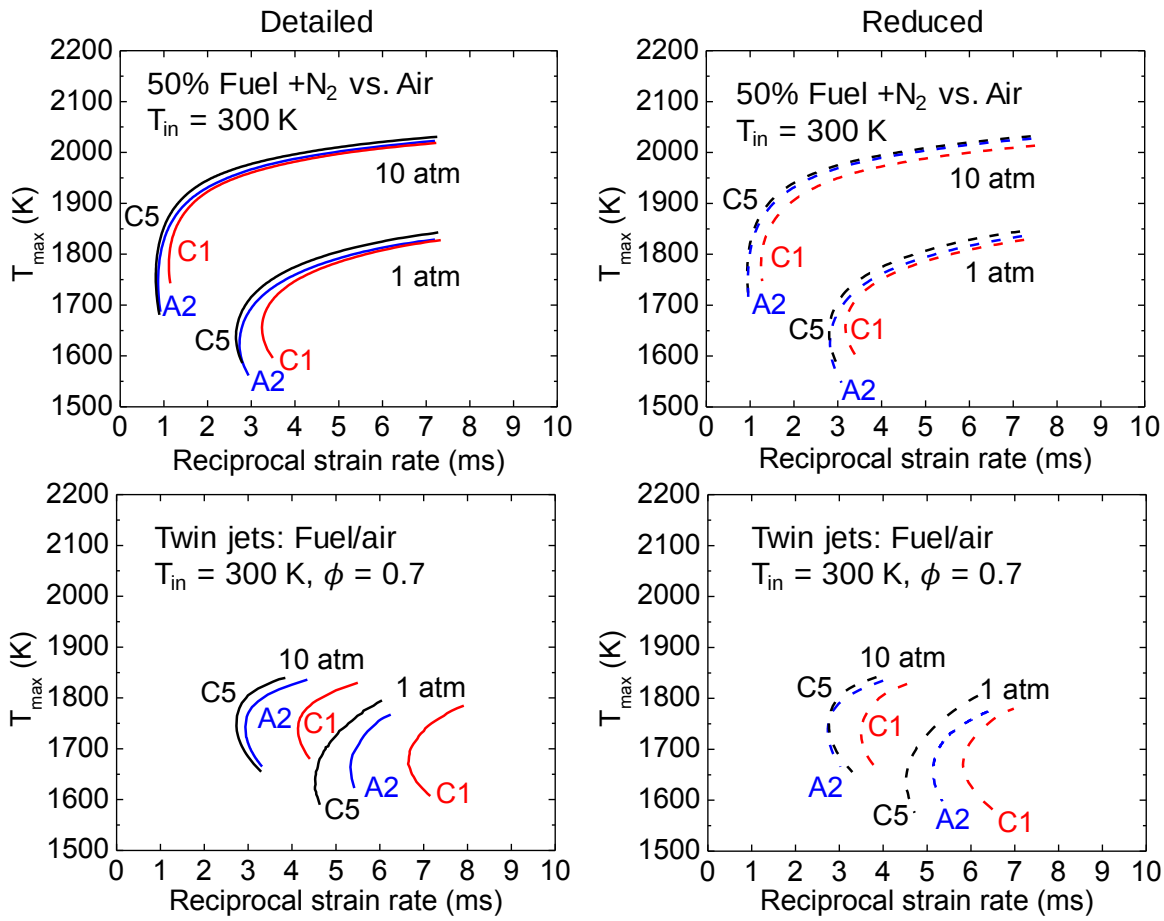

Figure 3-11. Comparison of the maximum temperature T_{max} in counterflow non-premixed (top panel) and premixed flames (bottom panel) as function of the reciprocal strain rate, calculated with the detailed (left panel, solid lines) and reduced (right panel, dashed lines) models, respectively.

3.4 Concluding remarks

In this chapter, the detailed HyChem models for real jet fuels, including A2, C1, and C5, are systematically reduced for high-temperature applications using the two-stage reduction method. Fuel-specific reduced models with 31, 26, and 31 species are obtained for A2, C1, and C5, respectively. A 35-species universal reduced model is further obtained using programmable fuel properties and fuel cracking reactions. In addition, a 45-species universal reduced model with NO sub-chemistry is developed.

The reduced models, including the fuel-specific and universal models, are validated comprehensively against the detailed HyChem models for 0-D homogenous, including auto-ignition and PSR, and 1-D diffusive systems, including laminar flame speed and extinction of premixed and non-premixed counterflow flames. The validation shows good agreements between the detailed and reduced models over a wide range of conditions.

The reduced models are further validated under LBO conditions in PSR, showing tight agreements with the detailed models. Important reactions for LBO of PSR are identified through a bifurcation analysis. Such reactions involve only small molecules in the oxidation core, and none of the fuel cracking reactions is found to play an important role at the selected LBO conditions.

Finally, the reduced models are shown to capture the fuel sensitivities well in both 0-D and 1-D systems, showing the fuel sensitivities are well retained in the reduction processes.

Chapter 4 A Reduced Kinetic Model for Ethylene/Air Combustion with Polycyclic Aromatic Hydrocarbons Formation Pathways

4.1 Introduction

Soot formation may have negative impacts on environment and human health. While soot are solid particles, the gaseous polycyclic aromatic hydrocarbons (PAHs) are important soot precursors. As such, a reliable gas phase kinetic model with PAH formation is critical for predicting sooting flames. Recently, a KAUST-Aramco Mech 1.0 with PAH chemistry up to coronene ($C_{24}H_{12}$ or A7) has been developed, and the predictions of soot precursors showed improved agreement with experimental data [118]. Although significant progress has been made in understanding the chemical kinetics of soot formation, predictive soot models have not yet been fully exploited in high-fidelity CFD simulations due to the enormous computational cost attributed to the large number of species. As such, computationally affordable reduced reaction models with PAH formation is necessary and important to accommodate detailed soot chemistry in high-fidelity CFD simulations. In this chapter, a reduced model for ethylene/air combustion with PAH formation pathways is developed to allow for efficient CFD simulations with predictive soot models.

4.2 Development of the reduced model

The detailed KAUST-Aramco PAH Mech 1.0 with 397 species is chosen as the starting model. In the detailed model, the comprehensively validated AramcoMech 1.3 C_0-C_2 chemistry developed by NUIG [119] is utilized and extended up to reactions involving benzene (C_6H_6 or A1). On this base model, the formation of aromatics larger than A1 is accounted by including the PAH growth pathways up to A7 for predicting soot formation.

The reduction is performed within the pressure range of 0.1-10 atm, equivalence ratio 0.5-5, and initial temperature of 1000-1500 K for auto-ignition. The detailed model with 397 species is first reduced to 271 species [118] with the skeletal reduction of DRG-X by Selvaraj *et al.* at KAUST with an error threshold 0.1. The fuel species C_2H_4, and two PAH species, *i.e.* pyrene ($C_{16}H_{10}$ or A4) and A7, are chosen as the starting species in DRG-X.

In the next step with DRGASA, in order to ensure the accurate prediction of soot, concentrations of H radical and important PAH species including A1, A4, and A7 are selected as target species, and a worst-case error 0.3 is specified for auto-ignition delay and PSR extinction time. The resultant skeletal model consists of 99 species. In the last step, the skeletal model is further reduced by the LQSSA method, resulting an 86-species reduced model.

In the following, the 86-species reduced model and the 99-species skeletal model are validated for auto-ignition delay, PSR temperature profiles, key species mole fractions in PSRs and counterflow diffusion flames against the detailed model.

4.3 Validation of the reduced model

Figure 4-1 compares the auto-ignition delay for the reduced, skeletal, and detailed models under low to high pressures and lean to rich mixtures. Figure 4-2 shows the comparison of temperature profiles in PSRs for the three models. The reduced and skeletal models agree tightly with the detailed model under various conditions.

In addition to the key global combustion responses, species that are important for the prediction of soot are compared. Figure 4-3 shows the comparison of species mole fractions of H radical and important PAH species in PSRs. The reduced and skeletal models yield satisfactory results compared with the detailed model for the species mole fractions. Figure 4-4 compares the mole fractions of H radical and important PAHs in 1-D counterflow diffusion flame. In the non-

premixed counterflow flame, C_2H_4 is used as the fuel and the oxidizer is air (O_2/N_2=1:3.76). The counterflow flame is established with pressure of 1 atm, inlet temperature of 300 K, and velocity of 100 cm/s for both fuel and oxidizer streams. The reduced and skeletal models exhibit good agreements with the detailed model for the species profiles.

The skeletal model has also been validated against experiments in both non-premixed and premixed flames in Ref. [118] by KAUST. Predictions of key PAH species are found to be in good agreements with experiments.

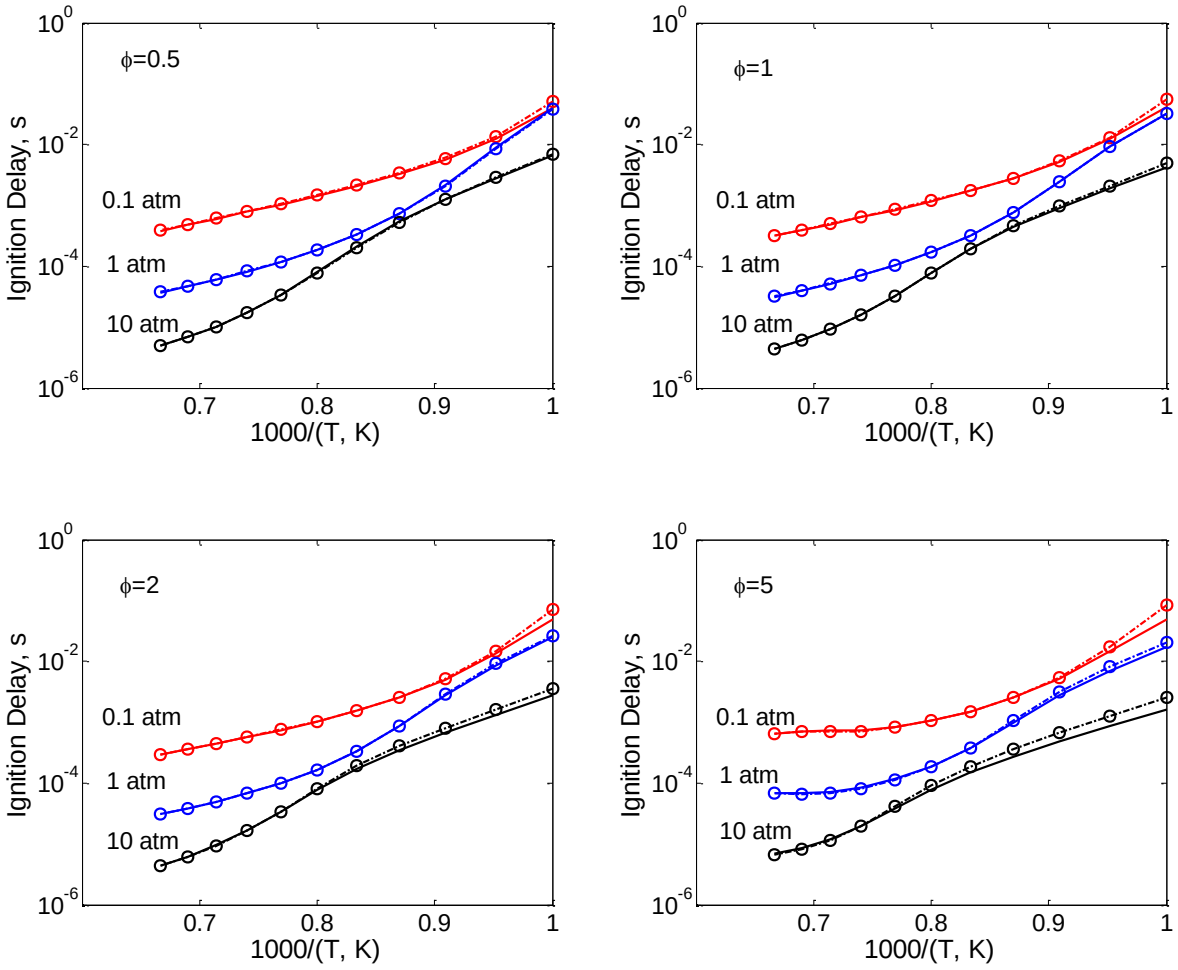

Figure 4-1. Ignition delay time as a function of initial temperature for ethylene/air mixture at pressures of 0.1, 1, and 10 atm, and equivalence ratios of 0.5, 1, 2, and 5, respectively. Solid lines: detailed. Dashed lines: skeletal. Symbols: reduced.

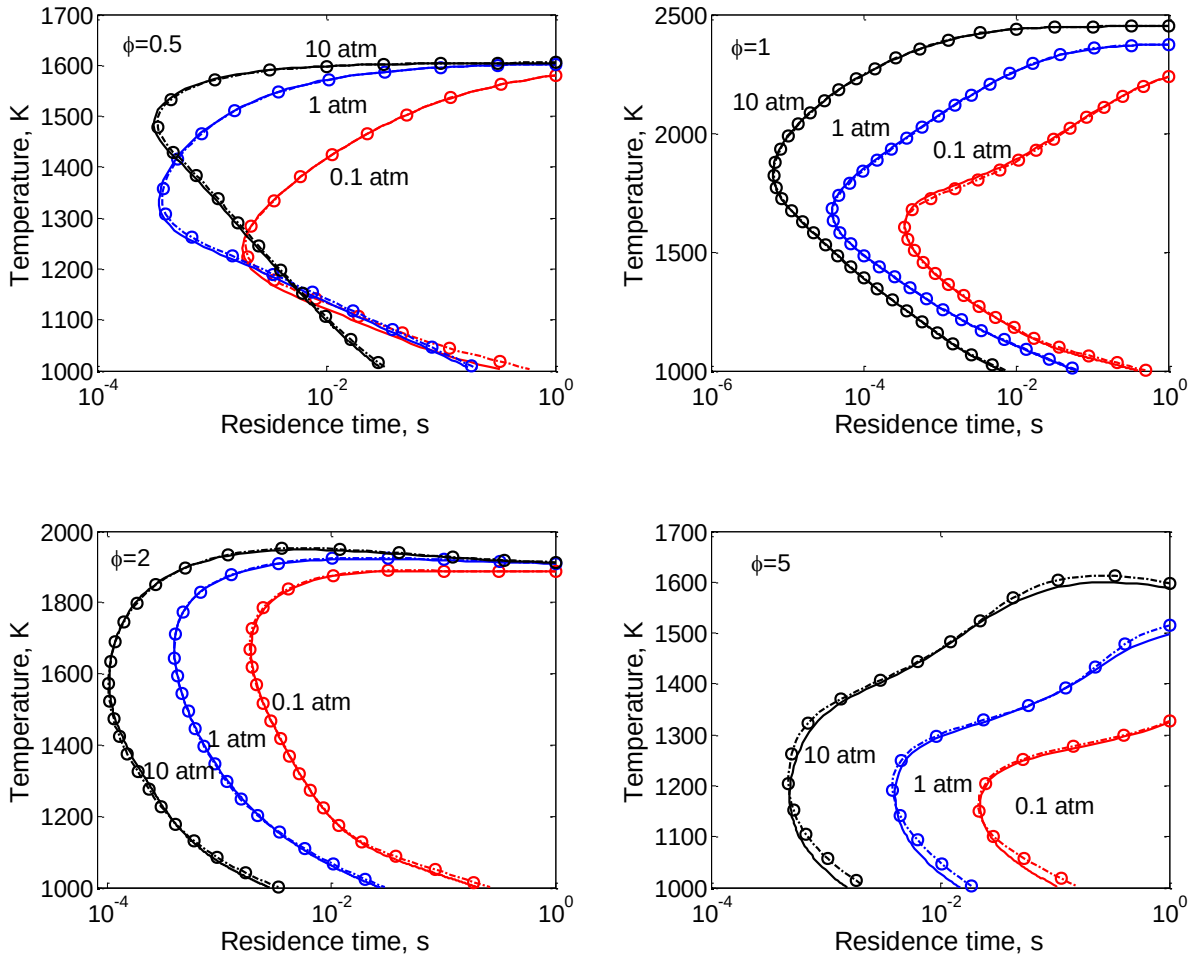

Figure 4-2. Temperature profiles in PSRs with inlet temperature 300 K for ethylene/air mixture at pressures of 0.1, 1, and 10 atm, and equivalence ratios of 0.5, 1, 2, and 5, respectively. Solid lines: detailed. Dashed lines: skeletal. Symbols: reduced.

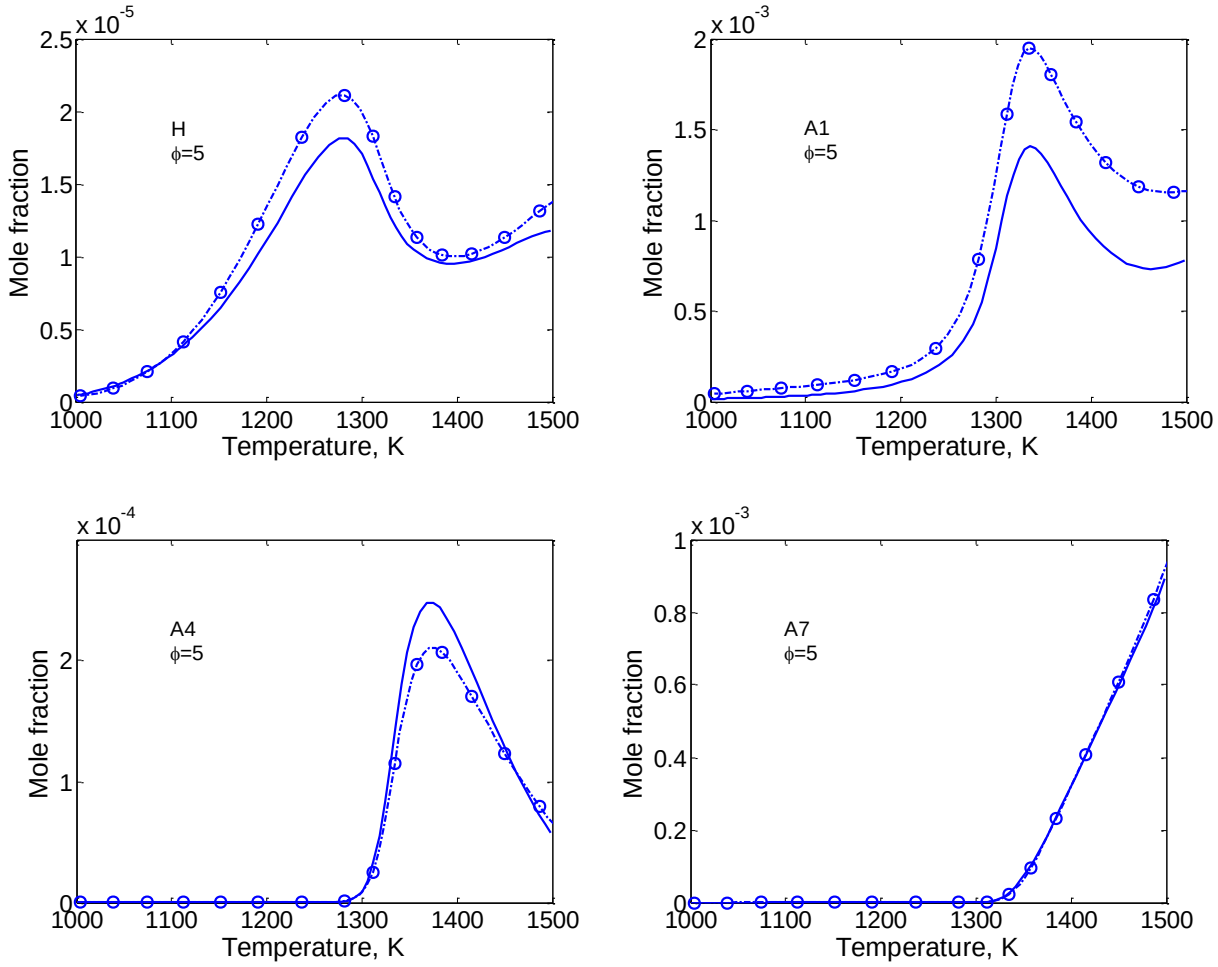

Figure 4-3. Mole fractions of H radical and major soot precursors in PSRs at pressure of 1 atm and equivalence ratio of 5. Solid lines: detailed. Dashed lines: skeletal. Symbols: reduced.

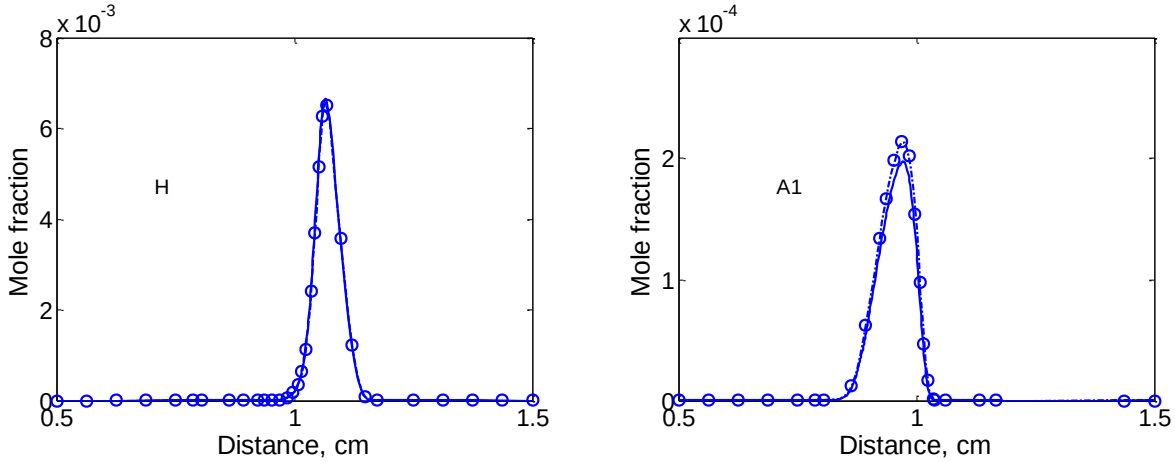

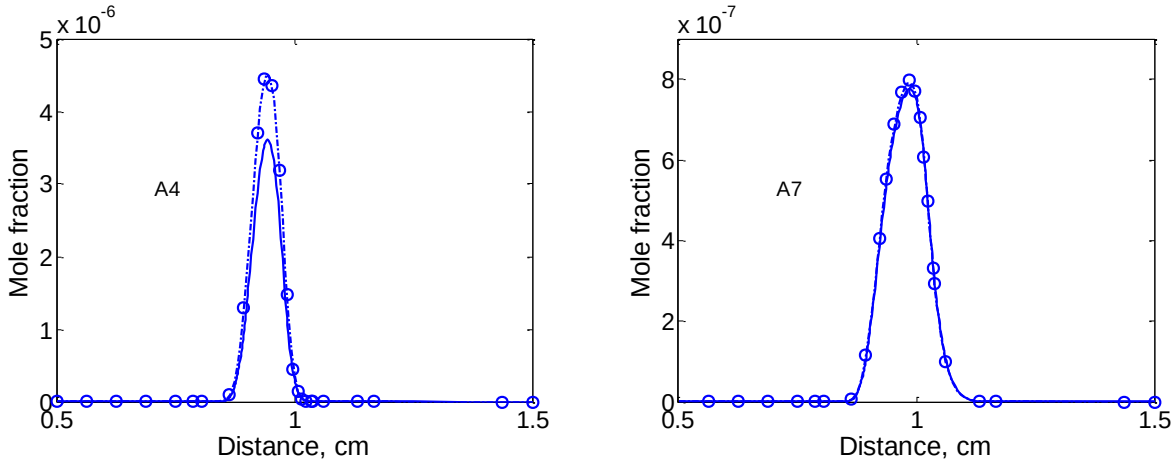

Figure 4-4. Mole fractions of H radical and major soot precursors in counterflow diffusion flame. Fuel: C_2H_4, oxidizer: air. Pressure is 1 atm, inlet temperature is 300 K, and velocity is 100 cm/s for both fuel and oxidizer streams. Solid lines: detailed. Dashed lines: skeletal. Symbols: reduced.

4.4 Concluding remarks

In this chapter, a 99-species skeletal model and an 86-species reduced model for ethylene/air combustion with PAH formation pathways are developed based on the KAUST-Aramco PAH Mech 1.0. The resultant skeletal and reduced models show satisfactory results compared with the detailed model for key global flame responses, including auto-ignition delay and PSR extinction time, and important species profiles, including H, A1, A4, and A7. The compact models derived in this study can enable efficient simulations with predictive soot models and benefit the study of soot formation.

Chapter 5 Efficient Approaches to Mixture-Averaged Diffusion Modeling

5.1 Introduction

In order to capture the important flame responses and structures, besides the affordable and accurate chemistry models developed in Chapter 2, Chapter 3, and Chapter 4, accurate modeling of molecular diffusion, *e.g.* using the MAD model or even the MCD model, is also important [2, 48, 49]. As discussed in Chapter 1, the MCD model features high accuracy but also high computational cost. In contrast, the MAD model may be preferable due to its fair accuracy and efficiency, where the computational cost is primarily attributed to the expensive evaluation of the $K \times K$ binary diffusion coefficient matrix, and it can be high for large reaction models. Simplified approaches, such as the unity Lewis number approach and the constant but non-unity Lewis number approach, are computationally cheap but important physics may be ignored. As such, it is necessary to investigate the effects on important flame responses with the simplified approaches and detailed molecular diffusion models, as well as to reduce the cost of the MAD model to facilitate its use in flame simulations.

The remainder of this chapter is organized as follows. First, the effects of molecular diffusion are reviewed, where the variations of species Lewis numbers are demonstrated using 1-D counterflow non-premixed and premixed flames, and the unity Lewis number approach is then compared with the detailed MAD model in calculating 1-D laminar flame speed and premixed counterflow extinction. In the following, fuel diffusion effects on premixed flame extinction are further investigated using 1-D counterflow flames. After demonstrating the importance and necessity of accurate modeling of molecular diffusion, three new methods to obtain accurate and efficient reduced MAD models are proposed. The reduced MAD models are comprehensively validated for global flame responses, including 1-D laminar flame speed and counterflow

extinction, and *a posteriori* validation of species diffusivities is further performed using DNS data with various reaction states. Lastly, the speedup factors for evaluating species diffusivities using the reduced MAD models are measured by comparing with the detailed MAD model.

5.2 Effects of molecular diffusion

5.2.1 Variations of species Lewis numbers in *n*-dodecane counterflow flames

Using the unity Lewis number approach, both the differential diffusion effects and variations of species Lewis numbers are ignored. For the prescribed constant but non-unity Lewis number approach, the differential diffusion is relatively retained whereas the variations of Lewis numbers are still neglected.

In the following, variations of species Lewis numbers are examined in both 1-D non-premixed and premixed counterflow flames under different stretches. The premixed flame involves opposed twin premixed jets of *n*-dodecane/air at inlet temperature of 300 K, equivalence ratio of 0.7, and pressure of 1 atm. For the non-premixed flame, the fuel stream consists of *n*-dodecane diluted with 50 % N_2 in mole and the oxidizer stream is air. The inlet temperature is 300 K and pressure is 1 atm for both streams. The global strain rate is defined in Eq. (2-1).

Figure 5-1 shows the extinction responses for the 1-D non-premixed and premixed counterflow flames, respectively, calculated using a 24-species reduced *n*-dodecane reaction model developed in Chapter 2 with the detailed MAD model from the CHEMKIN transport library [57, 96]. Maximum temperatures are plotted against the reciprocal global strain rates, where the turning point represents the extinction state. For each curve, two states, P_1 and P_2, with distinct strain rates are selected for further demonstration. In Figure 5-2(a) and Figure 5-2(b), Lewis numbers for each species at different grid locations are evaluated based on the solutions of P_1 and

P_2. The standard deviations for species Lewis numbers are further plotted in Figure 5-2(c) and Figure 5-2(d) for non-premixed and premixed flames, respectively.

It is seen that, in the non-premix flames, the standard deviations are larger than those in the premixed flames. The largest deviation occurs for the fuel species *n*-dodecane, and the second is for 1-hexene, since these two species quickly decompose into small molecules near the flame front and their concentrations change significantly. From Figure 5-2(a-d), it can be observed that, 1) Lewis numbers for different species are quite different, *i.e.* differential diffusion effects are prominent and not negligible, and 2) Lewis numbers for each species vary significantly along the domain. These observations indicate that, the unity Lewis number approach or prescribed constant but non-unity Lewis number approach may not be suitable for high-fidelity flame simulations, especially when the mixture composition and temperature change dramatically, *e.g.* near the flame front, or when local ignition or extinction is involved.

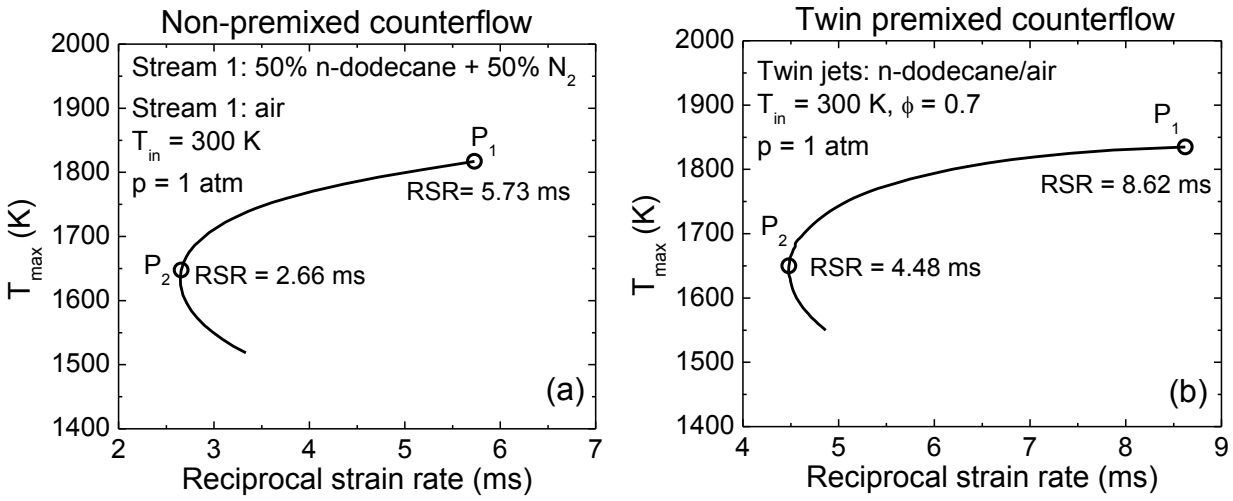

Figure 5-1. (a) 1-D counterflow extinction responses for non-premixed and (b) twin premixed flames with *n*-dodecane as the fuel. P_1 and P_2 are the sampled reaction states on the curves. RSR: reciprocal strain rate.

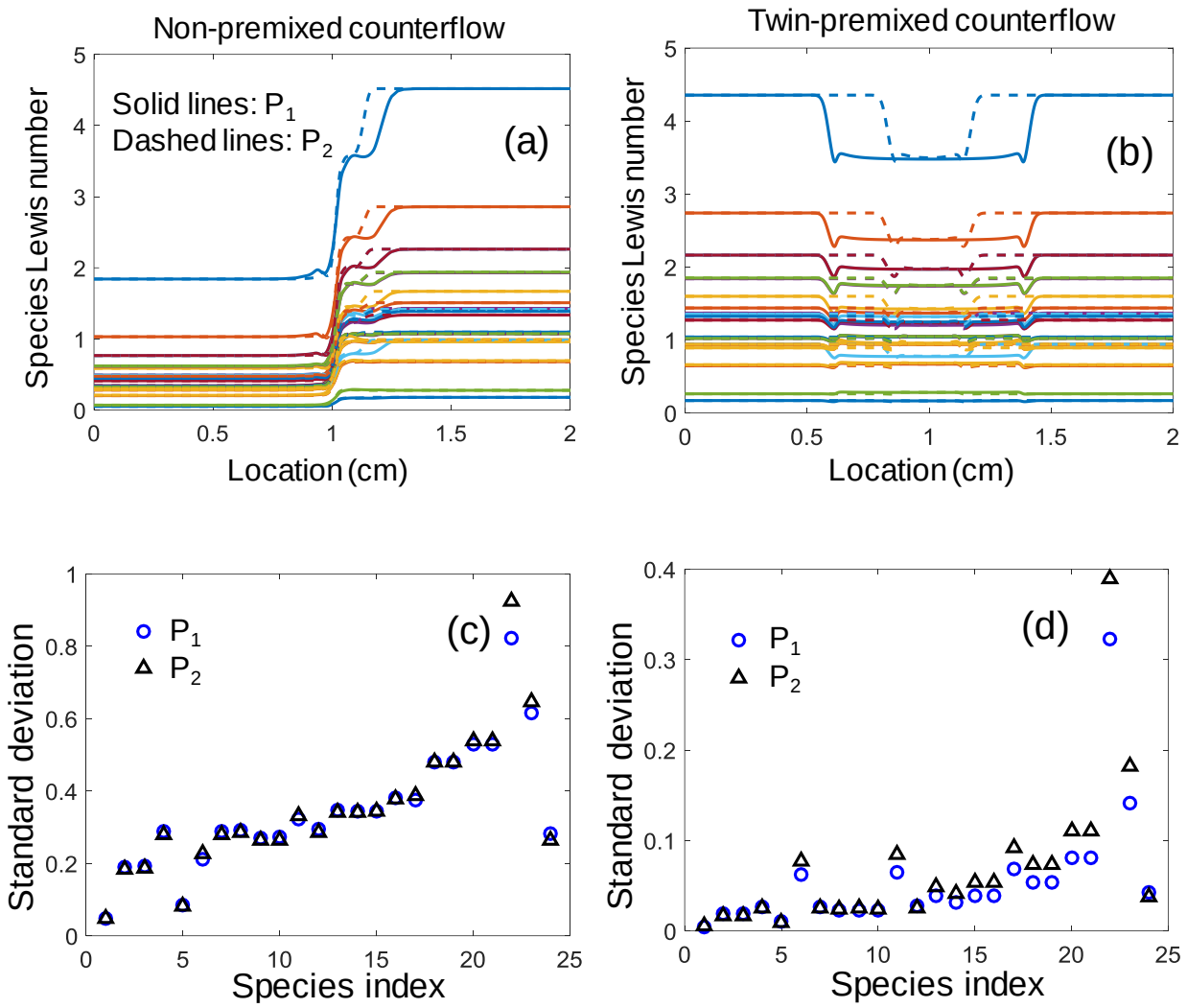

Figure 5-2. Species Lewis numbers at different grid locations for (a) 1-D non-premixed and (b) premixed counterflow flames, respectively. Standard deviations in species Lewis numbers for (c) non-premixed and (d) premixed counterflow flames, respectively.

5.2.2 Unity Lewis number and the MAD model in premixed flames

From the previous results, significant variations of species Lewis numbers have been observed. To further investigate the effects of unity Lewis number approach on global flame responses, laminar flame speeds and premixed counterflow flame extinctions are calculated using the detailed MAD model and unity Lewis number approach, respectively. The results are shown

in Figure 5-3. Significant discrepancies are observed from the results between the detailed MAD model and unity Lewis number approach. These results clearly indicate the inadequacy of the unity Lewis number approach in predicting important flame responses such as flame propagation or extinction.

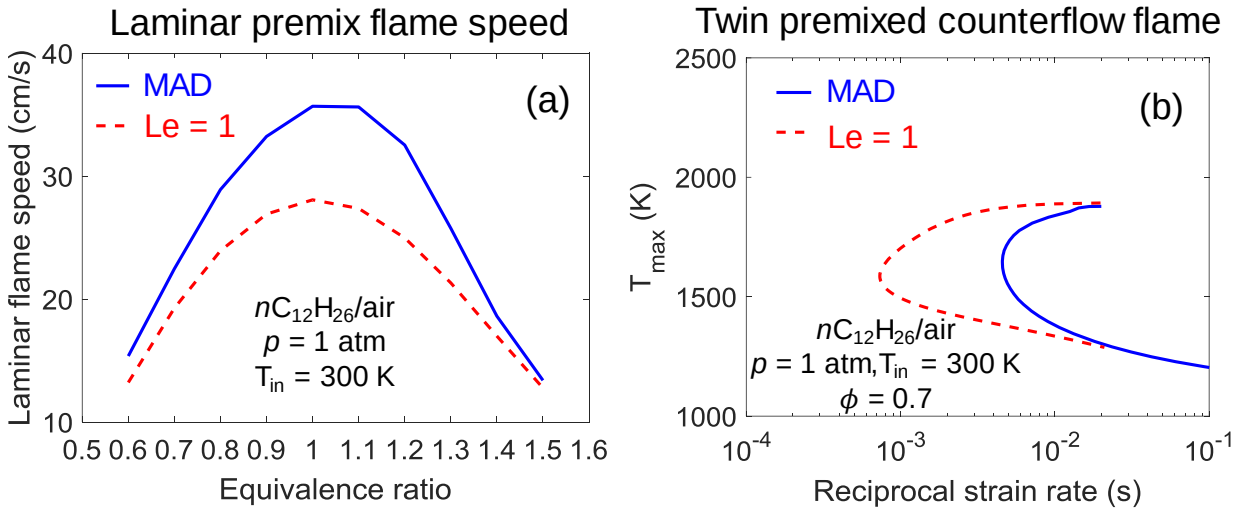

Figure 5-3. (a) Laminar flame speed as a function of equivalence ratio and (b) maximum temperature as a function of reciprocal strain rate in twin premixed counterflow flames, calculated using the detailed MAD model (solid lines) and unity Lewis number approach (dashed lines), respectively.

5.2.3 Fuel diffusion effects on premixed counterflow flame extinction

As the unity Lewis number approach may be a too strong assumption, let us focus on the fuel diffusion effects on counterflow flame extinction responses. In Ref. [120], Holley *et al.* performed a systematical sensitivity analysis of 1-D counterflow flame extinction strain rate to the fuel diffusion. Non-premixed counterflow extinctions of *n*-dodecane were found to be sensitive to the fuel diffusivity. In these flames the diffusion of the fuel is typically slow due to the large fuel size and large molecular weight, but the diffusion process is critical for the fuel molecules to mix

with the oxidizer transported from the other side in non-premixed counterflow flames [121]. In contrast, for premixed counterflow flames, which were established by counterflowing a premixed *n*-dodecane/air jet at 403 K against a N_2 jet at 298 K at 1 atm, the extinction strain rates were found to be insensitive to the fuel diffusivity. In Figure 5-4(a), the same configuration for the premixed counterflow used by Holley *et al.* is employed. With a ±20% perturbation in the fuel diffusivity, the sensitivity of extinction strain rate, defined as $d\ln RSR\,/d\ln D_{Fuel}$, is about ±20% when the equivalence ratio is 0.7 for the premixed jet. This is consistent with the observations made by Holley *et al*. This level of sensitivity is considered to be insignificant compared with that of the non-premixed counterflow flames. However, if the premixed counterflow is established using twin premixed jets rather than a premixed jet against a N_2 jet used by Holley *et al.*, the sensitivity increases dramatically to larger than ±50% with the same equivalence ratio 0.7 for twin jets, as shown in Figure 5-4(b).

In Figure 5-5(a), the fuel diffusivity effects on twin premixed counterflow flame extinctions are investigated with four different equivalence ratios, including $\phi = 0.7$, 1, 1.3, and 2. It is found that for the lean case ($\phi = 0.7$) and the very rich case ($\phi = 2$), the effects of fuel diffusivity are prominent due to the relatively low extinction strain rates. P_1, P_2, P_3, and P_4 are four points chosen near the extinction state from the solution calculated with the detailed MAD model. The temperature profiles of the four sampled points are plotted in Figure 5-5(b). Different directions (signs) of sensitivities are observed for the lean ($\phi = 0.7$) and the rich case ($\phi = 2$). For the lean case ($\phi = 0.7$), as the fuel is deficit, more fuel molecules are transported to the flame zone and therefore it can sustain a higher strain rate when the diffusivity of the fuel is increased by a factor of 1.2. For the rich case ($\phi = 2$), the extinction is mostly attributed to the incomplete combustion, where the flame will be easier to be extinguished with increased fuel diffusivity

The results from Figure 5-4 and Figure 5-5 reveal that, the diffusion of *n*-dodecane can also be important for premixed counterflow extinction which was considered insignificant in previous studies, especially when the extinction occurs at a low strain rate. The above analysis demonstrates the importance of molecular diffusion in flame propagation and extinction problems. Therefore, it is necessary to employ accurate molecular diffusion models, *e.g.* the MAD model, in flame simulations. However, the computational cost of the MAD model can be high due to the quadratic dependence on the number of species. In the following, efficient and accurate approaches for the MAD model reduction will be proposed.

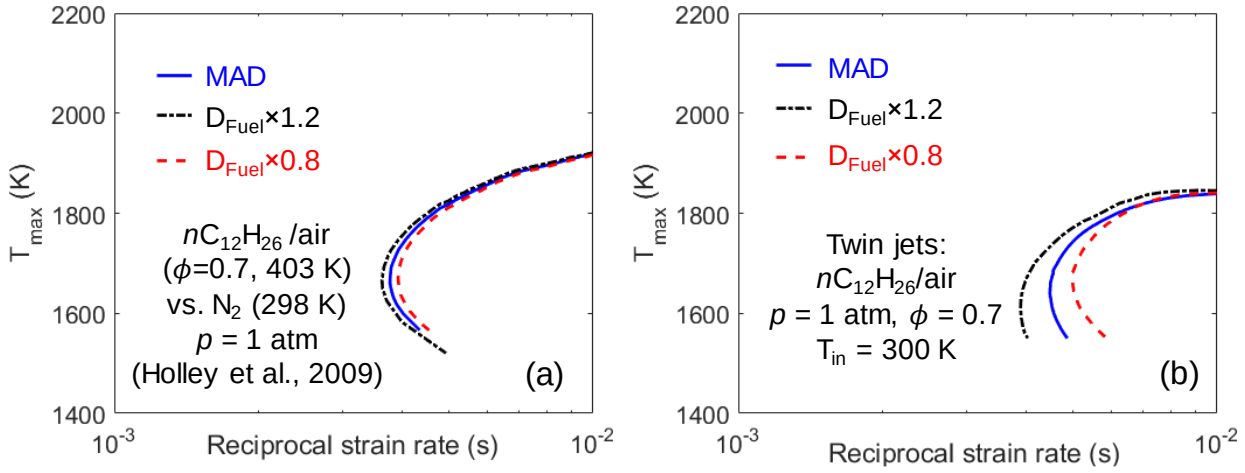

Figure 5-4. Maximum temperature as a function of reciprocal strain rate for counterflow flames with (a) fuel/air mixture against N_2 and (b) twin premixed jets, calculated using the detailed MAD model with and without perturbed fuel diffusivity, respectively.

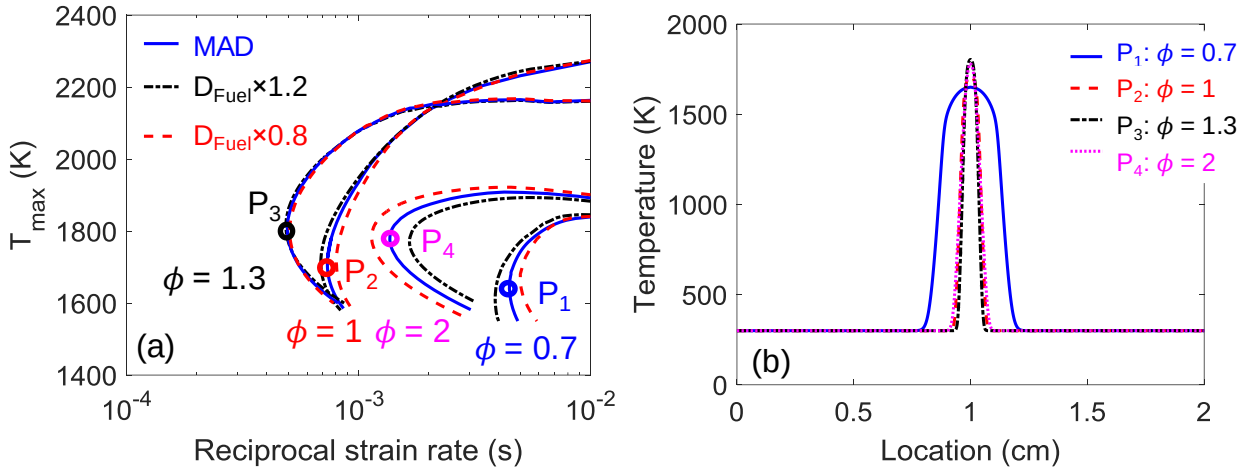

Figure 5-5. (a) Maximum temperature as a function of reciprocal strain rate for twin premixed counterflow flames at different equivalence ratios, calculated using the detailed MAD model with and without perturbed fuel diffusivity, respectively. (b) Temperature profiles calculated with the detailed MAD for four near extinction states P_1, P_2, P_3, and P_4.

5.3 Methodologies

5.3.1 A brief review of the diffusive species bundling approach

The species bundling approach developed by Lu and Law [58] quantifies the similarity in binary diffusion coefficients by measuring the relative error in binary diffusion coefficients between a pair of species *i* and *j*, which is defined as

$$\varepsilon_{i,j} = \max_{\substack{k=1,\ldots,K \\ T_{min}<T<T_{max}}} \left| \ln\left(\frac{D_{i,k}}{D_{j,k}}\right) \right|, \tag{5-1}$$

where $T_{\min}$ to $T_{\max}$ is the range of temperature users are interested in. Given a user-specified error threshold ε, the binary diffusion coefficients of species *i* and *j* are considered as similar if $\varepsilon_{i,j} < \varepsilon$. Therefore, species with similar binary diffusion coefficients can be bundled into one group, and each group has a representative species. The systematic reduction is formulated as an integer programming problem and solved efficiently with a greedy algorithm [58].

Once the species with similar binary diffusion coefficients are bundled into groups, the binary diffusion coefficient between two species is replaced by the binary diffusion coefficient between the two groups. The grouped binary diffusion coefficient matrix $\boldsymbol{DG}$ is

$$DG_{n,m} = D_{r(n),r(m)}, \text{where } n, m = 1,2, \dots, KG. \tag{5-2}$$

where the subscripts *n* and *m* represent the *n*th and *m*th group, respectively. $DG_{n,m}$ represents the binary diffusion coefficient between two groups, and *KG* is the number of groups. $r(n)$ is a function that returns the representative species for group *n*. The species diffusivity for species *i* can be rewritten as

$$\overline{D}_i = \frac{1 - Y_i}{Q_{\mathrm{g}(i)} - \dfrac{X_i}{DG_{\mathrm{g}(i),\mathrm{g}(i)}}}, \tag{5-3a}$$

$$Q_n = \sum_{m=1}^{KG} Q_{n,m}\,, Q_{n,m} = \frac{XG_m}{DG_{n,m}}, \tag{5-3b}$$

$$XG_m = \sum_{\mathrm{g}(l)=m} X_l, \tag{5-3c}$$

where $\mathrm{g}(i)$ is a function that returns the group number for species *i*, and XG_m is the summation of species mole fractions in group *m*. With species bundling, the original binary diffusion coefficient matrix $\boldsymbol{D}$ is reduced to a grouped matrix $\boldsymbol{DG}$. The dimension is reduced from *K*×*K* to *KG*×*KG*, which gives a nearly quadratic speedup factor $(K/KG)^2$ in the evaluation of diffusion terms. The reduction method through species bundling was tested for different reaction models. Validations in premixed and non-premixed flames showed good agreement with the detailed MAD model, and significant reduction in CPU time was achieved in the evaluation of species diffusivities [58].

5.3.2 A reduced MAD model based reaction states sampling and species bundling

For convenience, a matrix $\boldsymbol{Q}$ is defined for Eq. (5-3b), where $Q_{n,m}$ is the entry at the *n*th row and *m*th column, and Q_n is the summation of the *n*th row. Note that, matrices $\boldsymbol{Q}$ and the bundled binary diffusion coefficient matrix $\boldsymbol{DG}$ have a one-to-one correspondence. $Q_{n,m}$ can be seen as a weighted contribution of $DG_{n,m}$ to the species diffusivity $\overline{D}_i$, where the group mole fraction XG_m is the weighting factor. It is observed in Eq. (5-3b) that, not every $Q_{n,m}$ has the same importance to the summation term Q_n, *i.e.* not every binary diffusion coefficient $DG_{n,m}$ has the same contribution to the species diffusivity $\overline{D}_i$. Some coefficients $DG_{n,m}$ may only have negligible contribution to $\overline{D}_i$, when the associated mole fraction XG_m always stays in a low level. Therefore, $Q_{n,m}$ involving such a low mole fraction can be ignored from Q_n. To quantify the importance of $Q_{n,m}$ to Q_n, an importance index $I_{n,m}$ is defined as follows,

$$I_{n,m} \equiv \frac{|Q_{n,m}|}{\max\limits_{j=1,KG} |Q_{n,j}|}. \tag{5-4}$$

In each row of matrix $\boldsymbol{Q}$, every entry $Q_{n,m}$ is normalized by the largest value in this row. If and only if the important index $I_{n,m}$ is larger than a user-specified threshold, $Q_{n,m}$ is considered to have a non-negligible contribution to the summation term Q_n, and thus will be retained in the evaluation of Q_n. As such, the associated $DG_{n,m}$ needs to be evaluated, otherwise it is ignored.

In Eq. (5-4), since the importance index involves both mole fraction and binary diffusion coefficient, it is a function of both local temperature and mixture composition, which may vary significantly in flames. To identify the important binary diffusion coefficients $DG_{n,m}$, a wide range of reaction states need to be sampled. Consequently, $DG_{n,m}$ is ignored if and only if its important index is smaller than the user-specified error threshold under every sampled condition, and it needs

to be retained otherwise. The set of important entries is therefore a union of important entries for every sampled condition and valid globally. The reaction states sampling can be performed in canonical reactors as done in kinetic model reduction, such as 0-D auto-ignition, PSR, and 1-D laminar stretched/un-stretched flames, based on the applications of interest. After the important $DG_{n,m}$ terms are identified based on reaction state sampling, a reduced MAD model can be formulated as

$$\overline{D}_i = \frac{1 - Y_i}{Q'_{\mathrm{g}(i)} - \frac{X_i}{DG_{\mathrm{g}(i),\mathrm{g}(i)}}}, \tag{5-5a}$$

$$Q'_n = \sum_{m=1}^{KG'} Q_{n,m}\,,\; Q_{n,m} = \frac{XG_m}{DG_{n,m}}. \tag{5-5b}$$

This reduced MAD model is referred to as Model 1 henceforth. Note that in Eq. (5-3) of the bundled MAD model, Q_n is a summation of KG terms. In contrast, Q'_n is only a summation of KG' terms, where KG' is the number of important entries in each row of $\boldsymbol{Q}$.

It is noted that, in the species bundling approach, the diagonal term $X_i/DG_{\mathrm{g}(i),\mathrm{g}(i)}$ in the denominator of Eq. (5-3a) is always evaluated, whereas in the denominator of Eq. (5-5a), the diagonal term $X_i/DG_{\mathrm{g}(i),\mathrm{g}(i)}$ is retained or removed together with the $XG_{\mathrm{g}(i)}/DG_{\mathrm{g}(i),\mathrm{g}(i)}$ term in the summation term Q'_n, depending on whether the associated binary diffusion coefficient $DG_{\mathrm{g}(i),\mathrm{g}(i)}$ is identified to be important or not. If the diagonal binary diffusion coefficient $DG_{\mathrm{g}(i),\mathrm{g}(i)}$ is identified to be unimportant, $XG_{\mathrm{g}(i)}/DG_{\mathrm{g}(i),\mathrm{g}(i)}$ will not be included in the summation term Q'_n. Subsequently, the diagonal term $X_i/DG_{\mathrm{g}(i),\mathrm{g}(i)}$ will also be removed from the denominator of Eq. (5-5a), because $X_i/DG_{\mathrm{g}(i),\mathrm{g}(i)}$ is even smaller than the unimportant term $XG_{\mathrm{g}(i)}/DG_{\mathrm{g}(i),\mathrm{g}(i)}$.

In addition, because the binary diffusion coefficient matrix $\boldsymbol{DG}$ is symmetric, if one binary diffusion coefficient $DG_{n,m}$ is identified as important and needs to be evaluated, the symmetric term $DG_{m,n}$ can be readily obtained. As such, the symmetric term for $Q_{n,m}$, *i.e.* $Q_{m,n}$, is also retained in the summation term.

5.3.3 A linear-time reduced MAD model for premixed fuel/air combustion

For premixed fuel/air combustion, the MAD of a species with respect to the bulk mixture can be approximated as

$$\overline{D}_i = D_{i,N_2}, \tag{5-6}$$

if N_2 is abundant in the mixture. This reduced MAD is referred to as Model 2 henceforth. Compared with the detailed MAD model, the computational cost of evaluating species diffusivities is reduced from the quadratic function $O(K^2)$ to a linear function $O(K)$. This method can be readily combined with the species bundling, resulting in

$$\overline{D}_i = DG_{g(i),g(N_2)}, \tag{5-7}$$

such that the computational cost is further reduced. This reduced MAD is referred to as Model 3 henceforth.

Next, Model 2 in Eq. (5-6) will be derived starting from the detailed MAD model in Eq. (1-2b) based on two assumptions.

Assumption 1:

$$\frac{WM}{W_{N_2}} = 1 + \varepsilon_{WM}, \tag{5-8a}$$

where W_{N_2} is the molecular weight of N_2, WM is the mean molecular weight of the mixture, and ε_{WM} is an error term depending on the mixture property and represents the relative discrepancy

between WM and W_{N_2}. This assumption is based on the argument that the mean molecular weight is close to the molecular weight of N_2 in premixed fuel/air combustion when N_2 is abundant.

Assumption 2:

$$\frac{D_{i,N_2}}{D_{i,j}} = \frac{W_j}{W_{N_2}} + \varepsilon_{j,N_2}, \tag{5-8b}$$

where ε_{j,N_2} is an error term depending on the molecular properties. This assumption is based the argument that the binary diffusion coefficient is dominated by the molecular weight effect.

Then, the mixture-averaged species diffusivity in Eq. (1-2b) is multiplied by D_{i,N_2} in both numerator and denominator and rewritten as:

$$\overline{D}_i = \frac{1 - Y_i}{\sum_{j \neq i}^{K} X_j \frac{D_{i,N_2}}{D_{i,j}}} D_{i,N_2}. \tag{5-9}$$

The denominator is then transformed to:

$$\begin{aligned} \sum_{j \neq i}^{K} X_j \frac{D_{i,N_2}}{D_{i,j}} &= \sum_{j \neq i}^{K} X_j \left(\frac{W_j}{WM} \frac{WM}{W_{N_2}} + \varepsilon_{j,N_2} \right) = \frac{WM}{W_{N_2}} \sum_{j \neq i}^{K} X_j \frac{W_j}{WM} + \sum_{j \neq i}^{K} X_j \varepsilon_{j,N_2} \\ &= \frac{WM}{W_{N_2}} (1 - Y_i) + \sum_{j \neq i}^{K} X_j \varepsilon_{j,N_2} \\ &= 1 - Y_i + \left\{ \varepsilon_{WM} (1 - Y_i) + \sum_{j \neq i}^{K} X_j \varepsilon_{j,N_2} \right\}. \end{aligned} \tag{5-10}$$

It is noticed that, Eq. (5-6) is exact when the error terms in the bracket are zero, *i.e.* Model 2 is identical to the detailed MAD model in such cases. It is seen that, there are two error terms in the bracket, the first one depends on the discrepancy between the mean molecular weight and the molecular weight of N_2, and the second depends on the molecular properties of the mixture. It will

be shown in the next section, the errors in Model 2 are rather small compared with detailed MAD model, *i.e.* the error terms in the bracket are small. In addition, a relative error can be defined as

$$err = \frac{\varepsilon_{WM}(1 - Y_i) + \sum_{j \neq i}^{K} X_j \varepsilon_{j,N_2}}{(1 - Y_i)} = \varepsilon_{WM} + \frac{\sum_{j \neq i}^{K} X_j \varepsilon_{j,N_2}}{(1 - Y_i)}, \quad (5\text{-}11)$$

where the first term ε_{WM} is a constant for every species. For the second term, when species *i* is N_2, the denominator $1 - Y_{N_2}$ is relatively small compared with other species due to the high mass fraction Y_{N_2}. As such, the second term is expected to be larger for N_2 than the other species. This indicates that N_2 may have a larger relative error in the species diffusivity than the other species if Eq. (5-6) is used for N_2.

5.4 Results and discussion

5.4.1 Structure of the binary diffusion coefficient matrix

Since the time-saving using the reduced MAD models is attributed to the reduction in the number of evaluated binary diffusion coefficients, the structures of the binary diffusion coefficient matrices with different MAD models will be shown in the following. The aforementioned 24-species reduced reaction model for *n*-dodecane is used here for demonstration. Figure 5-6 shows the sparse pattern of the binary diffusion coefficient matrix for the detailed MAD model, bundled model, and Model 1, respectively. The black pixels are the coefficients that need to be evaluated through polynomials. Note that the binary diffusion coefficient matrix is symmetric and thus only about half of the entries need to be evaluated. With the detailed MAD model, total 276 binary diffusion coefficients need to be evaluated through polynomials in this 24×24 matrix. Note that the diagonal terms are not needed for the detailed MAD. With the species bundling, the binary diffusion coefficients are reduced to 14 groups with an error threshold of 0.1 in the temperature range of 300–3000 K. As such, only 105 coefficients need to be evaluated. In Model 1, the binary

diffusion coefficients are first bundled into 14 groups and then unimportant entries in the bundled binary diffusion matrix are eliminated using an error threshold of 0.1. The important entries are identified based on reaction states sampled over a wide range of conditions with equivalence ratio of 0.5-1.5, pressure of 1-10 atm, inlet temperature of 300 K for PSR, and initial temperature of 1000-1600 K for auto-ignition. The parameter range is chosen to be the same with that used in the development of this 24-species reduced reaction model in Chapter 2. Finally, only 3 columns in the matrix, which correspond to 3 important groups with high mole fractions, are retained. These 3 groups are 1) H_2O, 2) N_2, O_2, CO, HO_2, H_2O_2, 3) CO_2. Note that, the sampling procedure in Model 1 does not necessarily result in fully columns.

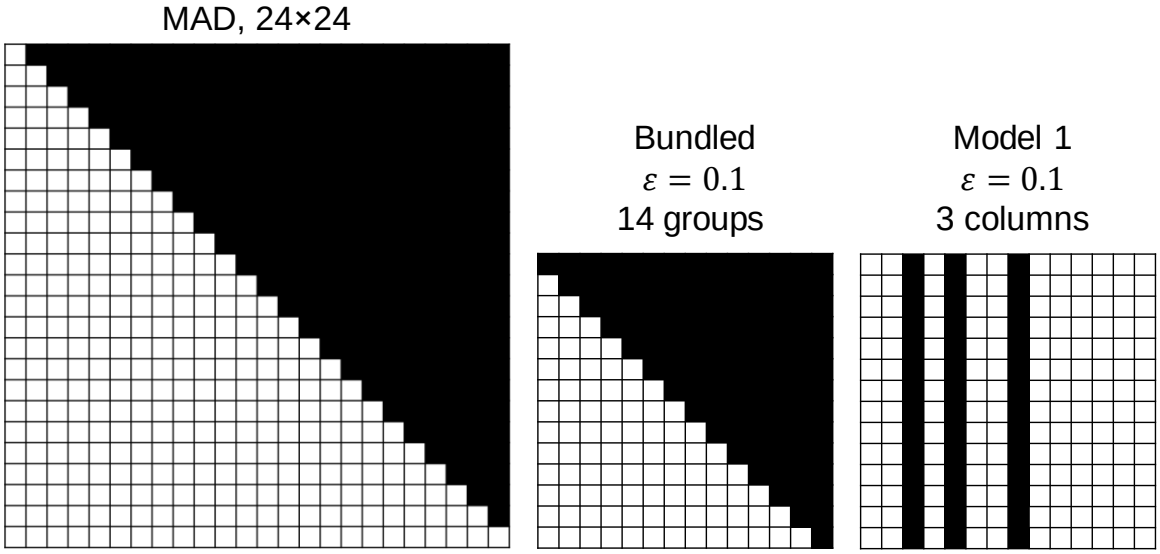

Figure 5-6. Patterns for the binary diffusion coefficient matrix of the detailed MAD model (left), bundled model (middle), and Model 1 (right), respectively. Black pixels are the entries that need to be evaluated.

For Model 2 and Model 3, the sparse patterns are shown in Figure 5-7. With Model 2, the number of non-trivial binary diffusion coefficients is significantly reduced to 24, while with Model

3, the number is further reduced to 14 with an error threshold of 0.1 in the temperature range of 300-3000 K.

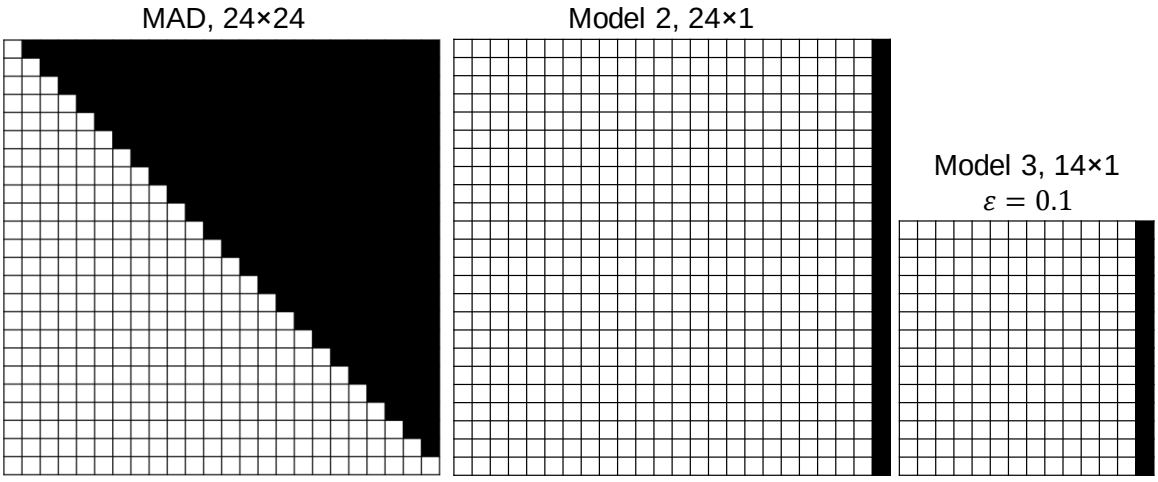

Figure 5-7. Patterns for binary diffusion coefficient matrix of the detailed MAD model (left), Model 2 (middle), and Model 3 (right), respectively. Black pixels are the entries that need to be evaluated.

5.4.2 Validation of global flame responses and *a posteriori* validation of species diffusivities

To validate the reduced MAD models, global flame responses, including laminar premixed flame speeds and premixed counterflow extinction strain rates, are calculated using the detailed MAD model, bundled model, and Models 1-3 for *n*-dodecane/air, respectively, at atmospheric pressure and inlet temperature of 300 K. The validation results are shown in Figure 5-8. The bundled model and three new reduced models agree quite well with the detailed MAD model under all the tested conditions.

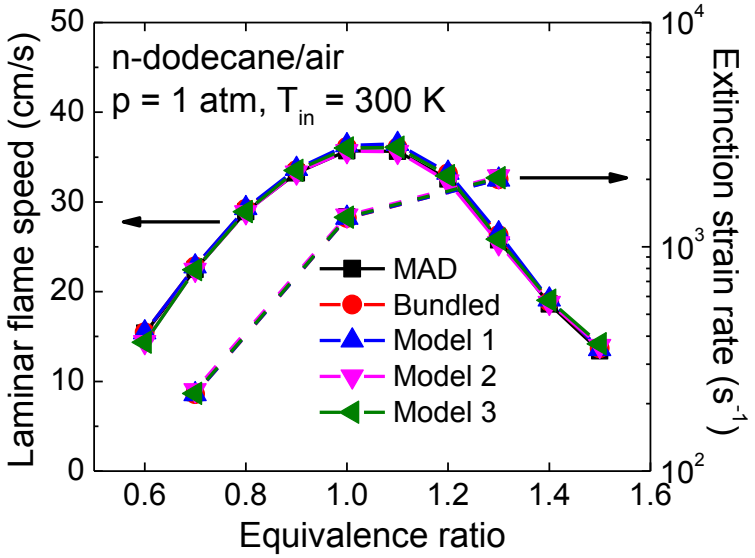

Figure 5-8. Laminar flame speed (left *y*-axis) and global extinction strain rate (right *y*-axis) as functions of equivalence ratio, calculated using the detailed MAD, bundled, and Models 1-3, respectively.

To scrutinize the errors in species diffusivities, *a posteriori* validation is performed using DNS data of a 2-D strongly turbulent premixed *n*-butane/air flame [117]. The 25-species reduced reaction model for *n*-butane developed in Chapter 2 was employed in this DNS. The DNS is for a premixed flame propagating into fresh mixture at temperature of 500 K with an equivalence ratio of 0.6 and pressure of 5 atm. The solution at the time of 0.4 ms is used for the present analysis, and the temperature field is shown in Figure 5-9(a). With an error threshold of 0.1, the 25-species model is first bundled to 10 groups in the temperature range of 300-3000 K. Next, for Model 1, only 3 important groups are identified with an error threshold of 0.1 based on reaction states sampled over equivalence ratio of 0.6-0.9, pressure of 1-5 atm, inlet temperature of 300 K for PSR, and initial temperature of 1000-1600 K for auto-ignition. Note that, the parameter range is chosen to be the same with that used in the development of this 25-species reduced reaction model. The 3 important groups include 1) H_2O, 2) N_2, O_2, CO, HO_2, H_2O_2, 3) CO_2, CH_2O, C_2H_2, C_2H_4, C_2H_5,

C_2H_6. Again, these groups are those have high mole fractions physically. For each grid point in the DNS data, the species diffusivities are calculated with different MAD models using the local composition and temperature solutions. The results from the detailed MAD model are taken as the accurate solutions to measure the errors in species diffusivities for different reduced models. The results are plotted in Figure 5-9(b). The worst-case error indicates the maximum error among all the species diffusivities at the same point.

As shown in Figure 5-9(b), the worst-case errors for the bundled, Model 1, and Model 3 are effectively controlled by the user specified error threshold of 0.1. It is noted that the errors of the bundled model and Model 1 overlap in this case, indicating the important groups are identified effectively. In addition, in this specific case, the worst-case errors occur for the same species C_2H_6 for both the bundled model and Model 1 and are exactly the same. Between the bundled model and Model 1, there are no errors for the diffusivities of C_2H_6 since it is in an important group in Model 1 and the binary diffusion coefficients in the entire column of the bundled diffusion matrix are retained. As such, the major source of the errors is actually from the bundling process.

The worst-case errors for Model 2 are within about 10%. Note that no error threshold is specified in Model 2. By scrutinizing the errors, it is found that the largest error always occurs in the diffusivity of N_2, which is consistent with the analysis in Eq. (5-11). Note that, with Model 2, the diffusivity of N_2 can be alternatively evaluated using the detailed MAD in Eq. (1-2) without additional evaluation of binary diffusion coefficients since all other binary diffusion coefficients with respect to N_2 are always needed in Model 2. In such cases, there is no error in N_2 diffusivity compared with the detailed MAD. The worst-case errors are subsequently less than 5% if excluding the error in N_2 diffusivity. The small errors in Model 2 indicate the error terms in Eq. (5-10) or Eq.(5-11) are essentially small under the test conditions.

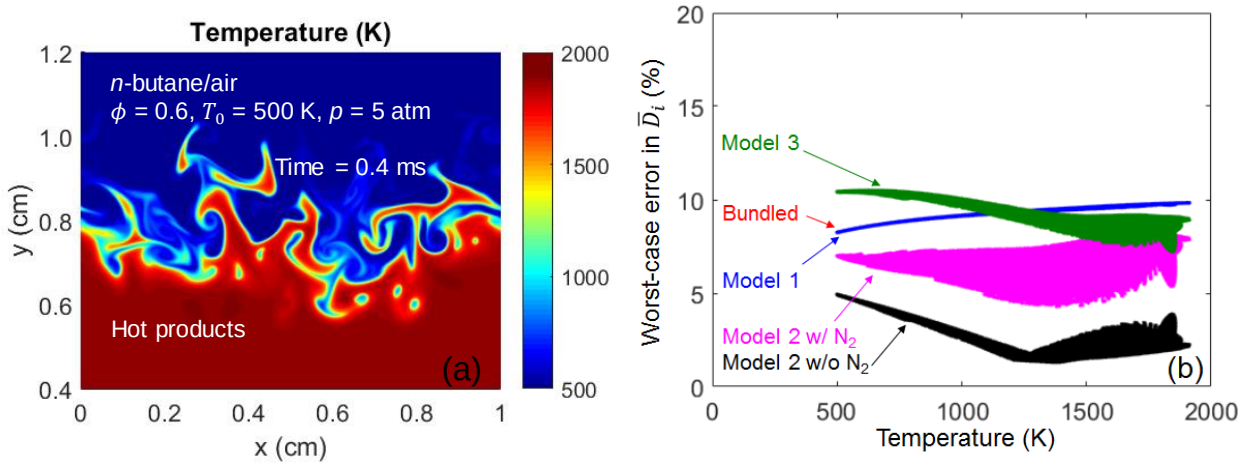

Figure 5-9. (a) Temperature contour for the 2-D DNS of *n*-butane/air at time of 0.4 ms. (b) Worst-case relative errors in species diffusivities as functions of temperature, calculated with different molecular diffusion models.

For the above DNS data, the worst-case errors in species diffusivities are further plotted in Figure 5-10 against $|\varepsilon_{WM}|$. The black dashed line is a reference line with a slope of 1. As discussed above, the worst-case errors always occur in N_2 diffusivities and the errors in other species are embedded, the errors in N_2 diffusivities are not considered here. It can be seen the maximum worst-case error is less than 5%, while the minimum is only about 1%. When $|\varepsilon_{WM}|$ is small enough, the second error term in Eq. (5-11) becomes dominant, and the errors deviate from the reference line. When $|\varepsilon_{WM}|$ is larger than about 2%, the worst-case error and $|\varepsilon_{WM}|$ follow almost a linear trend with a slope of 1, indicating that $|\varepsilon_{WM}|$ is the leading order error source under such conditions.

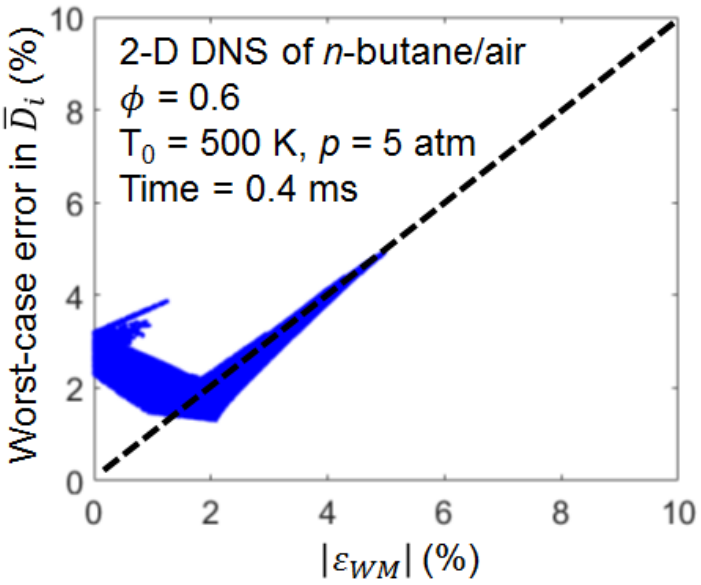

Figure 5-10. Worst-case error in species diffusivity in Model 2 as a function of the relative discrepancy between the mixture mean molecular weight and the molecular weight of N_2 using the 2-D DNS data at 0.4 ms. Dashed line: a reference line with a slope of 1.

5.4.3 Model 1 for non-premixed flames

Note that the above validations are based on premixed applications, *e.g.* laminar flame speed, premixed counterflow flames, and the 2-D DNS. While Model 2 and Model 3 are developed only for premixed fuel/air combustion, Model 1 is applicable for both premixed and non-premixed flames.

To demonstrate the applicability of Model 1 in non-premixed flames, a non-premixed counterflow flame is simulated with *n*-dodecane diluted with 50% N_2 in mole counterflowing against air. Both streams are at 300 K and 1 atm. The bundled MAD model for the non-premixed flame is the same with the aforementioned 14-group bundled model used in premixed flames, as the bundling approach does not depend on mixture compositions and only depend on temperature. For Model 1, the important groups are identified by sampling from this non-premixed counterflow

configuration with different strain rates with an error threshold of 0.1. In addition to the three important groups identified for premixed flames in Figure 5-6, two additional groups, including 1) *n*-dodecane and 2) C_2H_2, C_2H_4, C_2H_6, are found important. Note that the second group involves major fuel cracking products.

Figure 5-11 shows the maximum temperature as a function of reciprocal strain rate for non-premixed counterflow flames of *n*-dodecane with the detailed MAD model, the 14-group bundled model, and Model 1 with 5 important groups, respectively. In Figure 5-11(a), while a slight discrepancy is observed between the detailed MAD and the 14-group bundled model, Model 1 agrees tightly with its starting model, that is the bundled model. Two distinct states P_1 and P_2 at low and high stretch rates respectively are sampled from the solutions of the detailed MAD model for further demonstration in the right figure. These solutions are used to evaluate the worst-case relative errors in species diffusivities for the bundled model and Model 1 in comparison with the detailed MAD model. In Figure 5-11(b), the worst-case relative errors in species diffusivities are plotted with temperature for the two states P_1 and P_2. The errors of the bundled model largely overlap with those of Model 1, again indicating the important groups are identified effectively in non-premixed flames

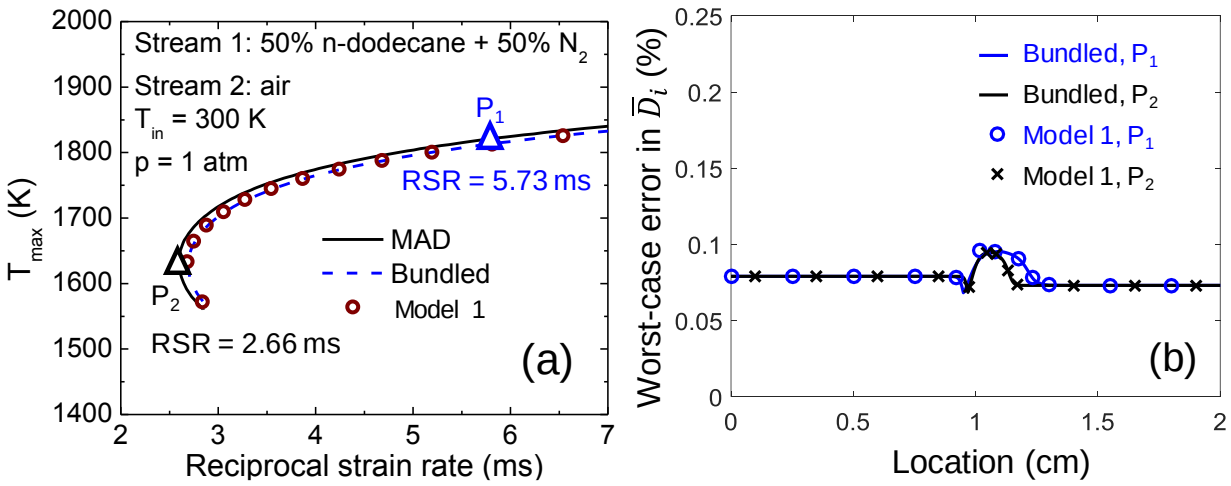

Figure 5-11. (a) Maximum temperature as a function of reciprocal strain rate for *n*-dodecane non-premixed counterflow. (b) Worst-case error in species diffusivities calculated using the two conditions, P_1 and P_2, sampled from the solutions using the detailed MAD model.

5.4.4 Error control study of Model 1

In the previous sections, an error threshold of 0.1 is used consistently to identify the important binary diffusion coefficients in Model 1. In the following, the error control behavior with different error thresholds for Model 1 is studied with the *n*-dodecane reaction model. The sampling space is the same with that used in Figure 5-6 for premixed flames, *i.e.* 0-D auto-ignition and PSR. The worst-case relative errors in species diffusivities are plotted in Figure 5-12 with respect to different error thresholds. The species diffusivities from the 14-group bundled model are used as the accurate solution to evaluate the errors in Model 1, since the bundled model is the starting model for Model 1. Two different worst-case errors are considered here, *i.e. local* worst-case error and *global* worst-case error. By using the locally identified important entries in the bundled diffusion coefficient matrix ***DG*** for each sampled condition and taking the maximum of the errors for all the sampled conditions and all the species, it results in the *local* worst-case errors represented by the black line with solid triangles. By using the union of the locally important entries for each sampled condition, the *global* worst-case errors are obtained and represented by the green line with empty circles, which is used throughout this chapter for Model 1. The blue dashed line is a reference line with a slope of 1. It is seen that the *local* worst-case errors are almost linearly proportional to the error thresholds, while the *global* worst-case errors are smaller and thus more conservative. When the error threshold is smaller than 0.01, the globally important entries recover all the entries in the bundled binary diffusion coefficient matrix ***DG***. As such, the error is exactly 0. When the error threshold becomes larger than 0.3, there are only 14 important

coefficients for both locally and globally important entries, which exactly correspond to the group containing N_2.

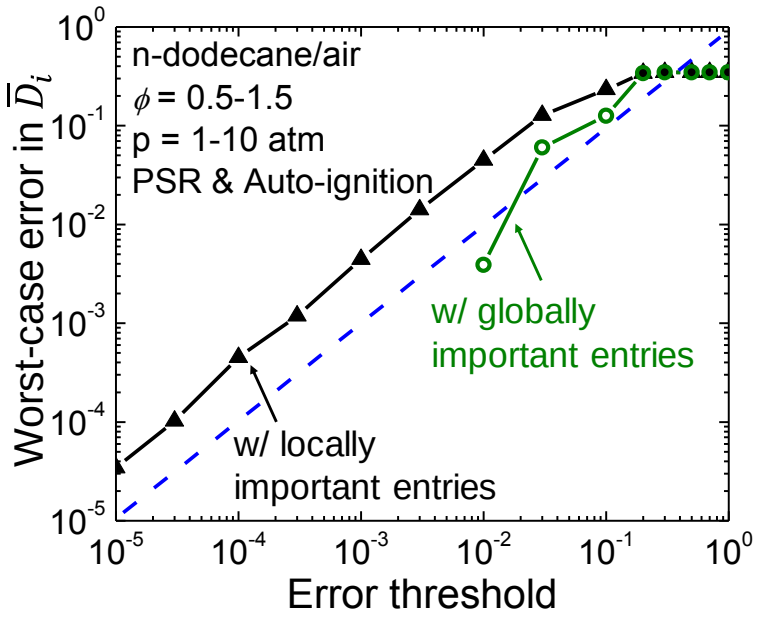

Figure 5-12. Worst-case relative errors in species diffusivities as functions of error thresholds. Dashed line: a reference line with a slope of 1.

5.4.5 Speedup factors and major features of reduced MAD models

After demonstrating the accuracy of the reduced MAD models, speedup factors are measured for the 24-species *n*-dodecane model and the 25-species *n*-butane model. In Table 5-1, the speedup of the bundled model and Models 1-3 are measured by comparing the averaged CPU time of one evaluation of species diffusivities with that of the detailed MAD model. It is seen that, all the three reduced MAD models proposed in this chapter show improvements in the computational efficiency compared with the bundled species model, especially Model 3 that achieves speedup factors up to 60.

To compare the different reduced MAD models, the major features of these reduced MAD models are summarized in Table 5-2. The bundled model, Model 1, and Model 3 all involve user-

specified error thresholds, whereas Model 2 does not involve any user-specified error thresholds and the worst-case error depends on the mixture composition, especially the discrepancy between the mean molecular weight and N_2 molecular weight, which has been numerically shown as the leading order error source in Figure 5-10. It is further noted that while only temperature space is sampled in the bundled model and Model 3, both temperature and composition spaces are sampled in Model 1.

Table 5-1. Speedup factors of reduced MAD models

Reduced MAD models	Speedup factors	
	n-dodecane (24 species)	*n*-butane (25 species)
Bundled	2.5 ($\varepsilon = 0.1$, 14 groups)	4.4 ($\varepsilon = 0.1$, 10 groups)
Model 1	4.6 ($\varepsilon = 0.1$, 3 columns)	6.5 ($\varepsilon = 0.1$, 3 columns)
Model 2	31.7	32.3
Model 3	44.5 ($\varepsilon = 0.1$)	61.6 ($\varepsilon = 0.1$)

Table 5-2. Major features of reduced MAD models

Reduced MAD models	Worst-case error	Sampling space	Applicable conditions
Bundled	Error threshold specified in bundling	Temperature	Both non-premixed and premixed flames
Model 1	Error thresholds specified in bundling and important index	Temperature and composition	Both non-premixed and premixed flames
Model 2	Mixture properties	No sampling	Premixed fuel/air combustion

Model 3	Mixture properties and error threshold specified in bundling	Temperature	Premixed fuel/air combustion

5.5 Concluding remarks

In this chapter, molecular diffusion effects on premixed flame propagation and extinction are investigated in 1-D laminar flames. Lewis numbers variations are found to be significant, and unity Lewis number approach may produce pronounced errors in predicting important flame responses such as flame speed and extinction strain rate. In addition, fuel diffusion effects on premixed counterflow extinction are studied with different configurations and equivalence ratios with *n*-dodecane as the fuel. While the fuel diffusion effects were previously considered insignificant for premixed counterflow extinction by countering a premixed jet against a N_2 jet, the effects are quite pronounced by countering twin premixed jets, especially when the extinction occurs at relatively low strain rate. Therefore, it is necessary to employ accurate molecular diffusion models in flame simulations.

To obtain efficient and accurate reduced MAD models, three new methods are proposed. The reduced MAD models are validated for 1-D laminar flame speed and premixed and non-premixed counterflow extinction with *n*-dodecane as the fuel. The validations of important global flame responses show very good agreements between the reduced MAD models and the detailed MAD model. Furthermore, *a posteriori* validation of species diffusivities using different reduced MAD models is performed using 2-D DNS data of a turbulent premixed *n*-butane/air flame, where the worst-case errors are shown to be well controlled.

Lastly, CPU time for evaluating species diffusivities is measured for the different reduced MAD models and compared with the detailed MAD model with two different fuels. Significant

speedup factors up to 60 are achieved for Model 3. To compare the different reduced MAD models, their major features are summarized in the end.

Chapter 6 A Dynamic Adaptive Method for Hybrid Integration of Stiff Chemistry

6.1 Introduction

Operator splitting schemes are widely used in practical simulations of multi-dimensional flows because expensive implicit solvers are only used for the integration of local chemistry to handle the chemical stiffness, while low cost explicit solvers can be adopted to integrate the non-chemical source terms. While error control of the splitting schemes has been well studied at the limit of small splitting time steps, the splitting time steps adopted in most practical simulations are typically moderately large to avoid excessively high computational cost, and such cases with moderately large splitting time steps are referred to as coarse cases [71]. Splitting errors induced by stiff chemistry in coarse cases can be rather large [122], although successes have been reported in many studies, *e.g.* [29, 70, 74]. The mechanisms for the large splitting errors in coarse cases can be complex and are not fully understood.

In this chapter, a mechanism associated with stiff chemistry that can result in failed error control of operator-splitting schemes in coarse cases is identified. The reason of the failure is attributed to the significant modification of the slow chemistry's trajectory by operator splitting, *i.e.* by excluding the transport source term from the sub-step for chemistry integration. AHI is then proposed as a substitute of the operator-splitting schemes to integrate combustion systems involving stiff chemistry with improved accuracy.

As the outline of this chapter, the large splitting errors of the Strang splitting scheme in coarse cases are first demonstrated and investigated using a toy problem. An AHI method is then proposed to resolve this issue and to achieve accurate and efficient time-integration of stiff chemistry coupled with transport. The AHI method is tested in auto-ignition and the solutions are compared with that from SENKIN [123], which utilizes the fully implicit DASAC solver based

on the backward difference formula (BDF). The results of AHI are then compared with that of the Strang splitting scheme for the toy problem and an unsteady PSR of hydrogen/air using detailed chemistry.

6.2 A toy problem with the Strang splitting scheme

A toy model is first constructed to investigate the possible scenarios where the operator splitting schemes may fail in coarse cases. The model involves the following three reactions.

$$A \overset{k_1}{\rightarrow} R \qquad (R_1)$$

$$R \overset{k_2}{\rightarrow} C \qquad (R_2)$$

$$A + \alpha R \overset{k_3}{\rightarrow} B + \alpha R \qquad (R_3)$$

where k_1, k_2 and k_3 are the reaction rate coefficients of reactions R_1, R_2 and R_3, respectively. Species *A* is the reactant, *B* is the product, *C* is an intermediate species that is not of direct importance to *A* and *B*, and *R* is a radical that controls the important reaction R_3 for product formation. The parameter α determines the overall reaction order and nonlinearity of R_3.

For simplicity, the transport term of species *R* is set to be a constant, *d*, and those for the other species are set to be zero. The term *d* mimics the effect of a mixture, *e.g.* in the preheat zone of a premixed flame, receiving substantial amount of radicals from a neighboring fluid element, *e.g.* in the reaction zone. Note that including nontrivial transport terms for the major species doesn't affect the nature of the toy problem.

The dependent variables and source terms for the toy problem can thereby be expressed as:

$$\mathbf{\Phi} = [A, B, C, R]^T,$$

$$\boldsymbol{S} = [-k_1 A - k_3 A R^{\alpha},\ k_3 A R^{\alpha},\ k_2 R,\ k_1 A - k_2 R]^T, \tag{6-1}$$

$$\boldsymbol{M} = [0,0,0,d]^T,$$

with the initial condition being

$$A = 1, B = C = R = 0, at\ t = 0$$

k_2 is chosen to be much larger than k_1, *i.e.* $k_2 \gg k_1$, such that *R* stays in quasi steady state (QSS) after an initial transient period and can be approximated as

$$R \approx \frac{k_1 A + d}{k_2} \tag{6-2}$$

and the timescale of *R* can be defined as $\tau = 1/k_2$. It is seen that the concentration of *R* is sensitive to transport unless $|d| \ll k_1 A$. However, without the transport term, the concentration of *R* in the chemistry sub-step in Eqs. (1-5) and (1-7) after an initial transient period can be approximated as

$$R \approx \frac{k_1 A}{k_2} \tag{6-3}$$

which can be significantly different from that in Eq. (6-2) if $|d|$ is not trivial, resulting in large errors in the reaction rate of R_3. The error in the chemistry sub-step can subsequently lead to significant splitting errors in the major species as demonstrated in the following cases.

The following parameters are used for the toy problem in all the simulations in the present study unless particularly specified: $k_1 = 1$, $k_2 = \tau^{-1} = 10^6$, $k_3 = \tau^{-\alpha}$, $d = 1$, while different values of α and the splitting time step Δt are used. Note that k_3 is selected such that the rate of reaction R_3 is $O(1)$. To measure the splitting errors, the "exact" solutions for this toy model are obtained using fully implicit integration with sufficiently small time steps such that the numerical error is negligible for the measurement.

Figure 6-1 shows the profiles of *A*, *B* and *R* in the toy model with $\alpha = 2$. It is seen that the splitting scheme with $\Delta t = 10^{-7}$ agrees well with the exact solution because Δt is sufficiently small to resolve radical *R* whose timescale is $\tau = 10^{-6}$, *i.e.* the problem is not stiff at such a small splitting time step. However, when a larger splitting time step, $\Delta t = 10^{-5}$, is used, which should nevertheless still be sufficiently small to accurately resolve the major species profiles, which have timescales of *O*(1), large errors occur for all the species. The error in *R* is primarily induced by the mechanism explained in Eqs. (6-2) and (6-3), and the errors in *A* and *B* can only be attributed to the error in *R* because the transport terms are trivial for *A* and *B*.

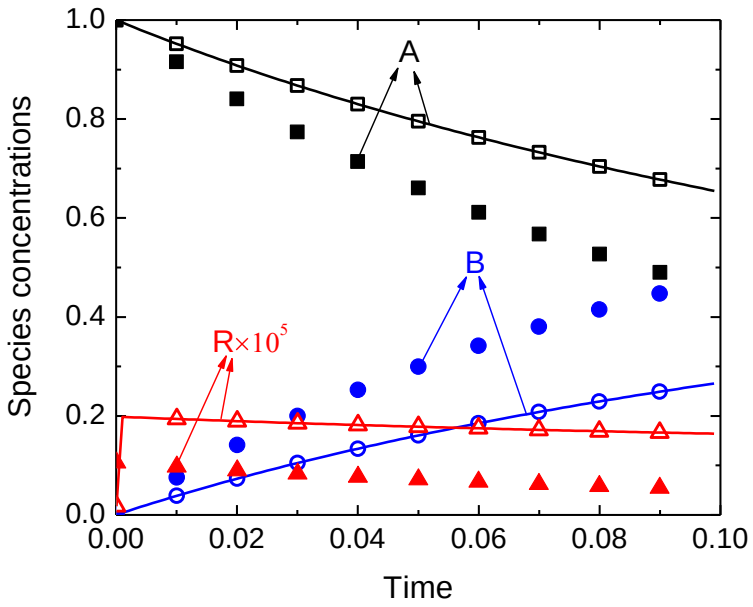

Figure 6-1. Calculated species concentration profiles for the toy problem with α=2 and τ=10^{-6}. Lines: exact solution; Closed symbols: Strang splitting scheme with Δt=10^{-5}; Open symbols: Strang splitting scheme with Δt=10^{-7}.

Figure 6-2 shows the relative errors in the concentrations of B and R, respectively, as functions of the splitting time step Δt for $\alpha = 2$, with the dotted line indicating the trend line of slope 2. In the present study, the relative error, ε, in a computed quantity, ψ, is defined as

$$\varepsilon = \frac{|\psi - \psi^E|}{|\psi + \psi^E|} \tag{6-4}$$

where ψ^E is the value from the exact solution. The relative errors in Figure 6-2 for the Strang splitting scheme is measured at the time when $A = 0.5$ in the exact solution for the toy problem. It is seen that when Δt is smaller than the radical timescale, $\tau = 10^{-6}$, the Strang splitting scheme is second-order in accuracy. However, with $\Delta t \gg \tau$, *e.g.* $\Delta t = 10^{-5}$, the error control fails and the relative errors quickly approach $O(1)$. It is worth mentioning again that a time step of 10^{-5} is an unnecessarily small time step size to resolve the species profiles with non-splitting schemes, as to be shown later.

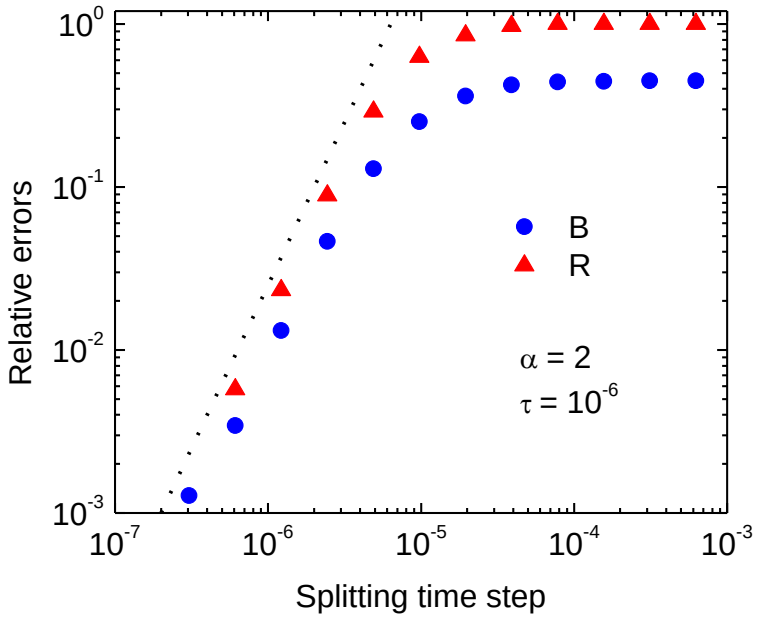

Figure 6-2. Relative errors in species concentrations for the toy problem with α=2, measured at the time when A = 0.5 in the exact solution, as functions of the splitting time step for the second-order Strang splitting scheme. Dotted line shows the trend line with slope of 2.

To further investigate the dependence of the splitting error on the nonlinearity of the toy problem, as characterized by the parameter α, Figure 6-3 shows the relative errors of the Strang splitting scheme in species concentrations measured at time when A = 0.5 in the exact solution for different α values. It is interesting to observe that while large errors are present for the strongly nonlinear cases, *e.g.* $\alpha = 2$, the errors in A and B vanish when the problem becomes quasi-linear in R, that is $\alpha = 1$. The reason for the small, or precisely zero, error in A and B at $\alpha = 1$ is attributed to the exact error cancellation, which also occurs when the operators are commuting in special cases [71]. It is noted that the splitting error changes sign at $\alpha = 1$. For the present toy problem, while errors in A and B vanish in the quasi-linear condition, the error in R nevertheless remains large such that the operators are not commuting. To scrutinize the process of the error cancellation in B, Figure 6-4 plots the concentrations of B and R within the first splitting time step $[0, \Delta t]$ for the cases with (a) $\alpha = 2$, (b) $\alpha = 1$, respectively, with $\Delta t = 10^{-4}$. It is seen in Figure 6-4(b) that while large errors in the concentration of B are present in the chemistry sub-steps for Eqs. (1-5) and (1-7), the errors cancel exactly at the end of the splitting time step for $\alpha = 1$, while the errors only cancel partially for the cases with $\alpha = 2$. It is noted again that the concentration of R cannot be accurately computed by the operator-splitting scheme regardless of the α values.

Based on the above observation, since nonlinearity is intrinsic in detailed chemistry, operator splitting schemes may subject to large splitting errors when significant radical sources from the transport term are present, *e.g.* for a mixture in the preheat zone of a premixed flame receiving H radicals from the reaction zone through back-diffusion.

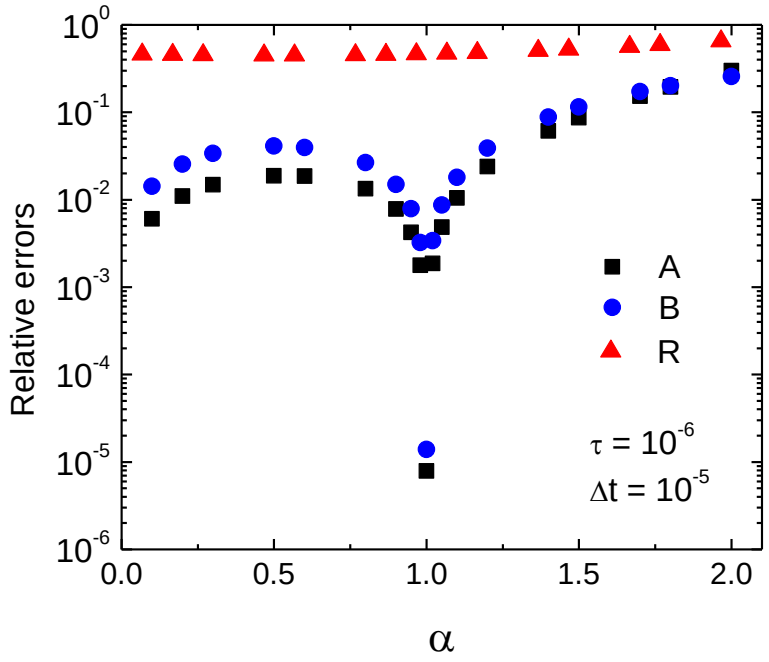

Figure 6-3. Relative errors in species concentrations for the toy problem, measured at the time A = 0.5 in the exact solution, as functions of α, for the Strang splitting scheme with Δt=10^{-5}.

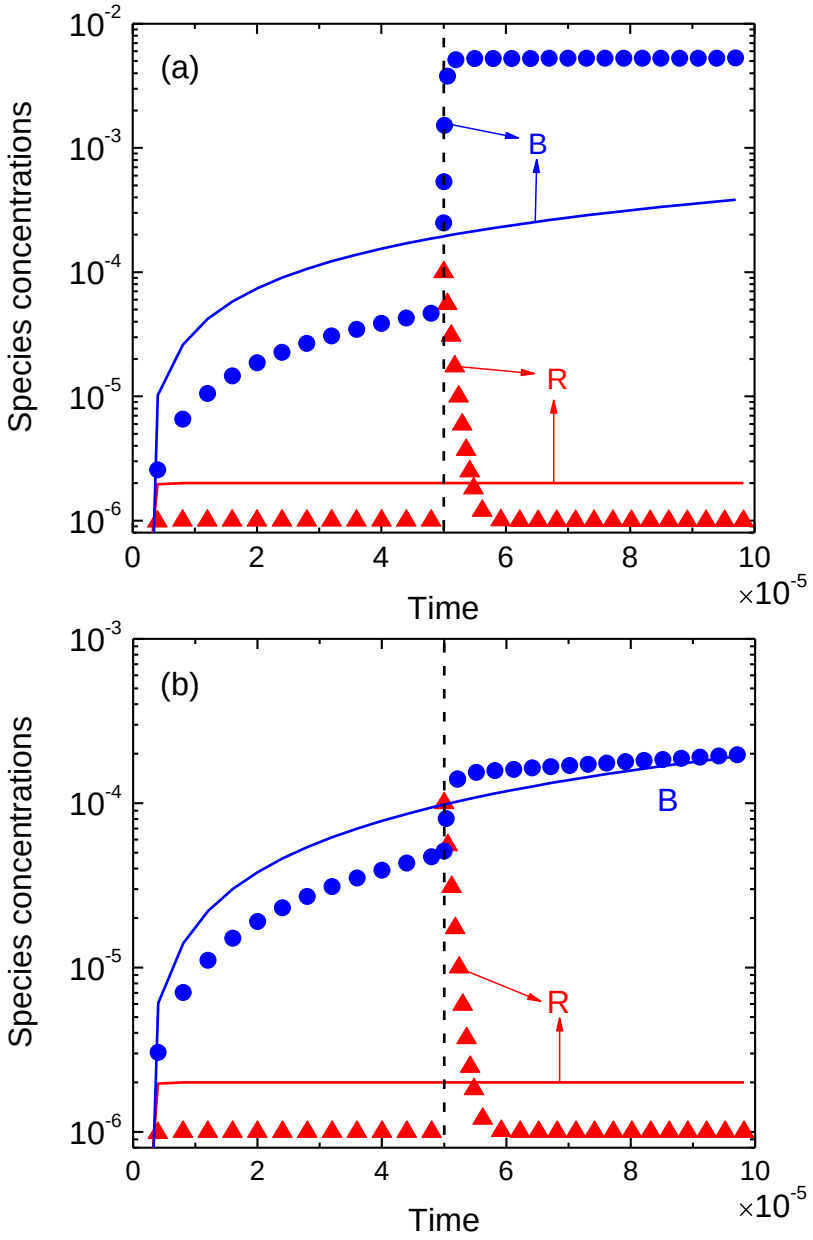

Figure 6-4. Concentrations of B and R calculated with the Strang splitting scheme with $\Delta t=10^{-4}$ for the toy problem with (a) $\alpha=2$ and (b) $\alpha=1$. The solid lines indicate the exact solutions and markers are from the Strang splitting scheme. The dash line indicates the end of integration of Eq. (1-5) and the beginning of the integration of Eq. (1-7). The jump in R results from the integration of Eq. (1-6).

6.3 A dynamic adaptive method for hybrid integration

To resolve this problem, an AHI method is proposed in the present study. The AHI method first separates the fast species and reactions from the slow ones by comparing their timescales with the integration time step. The fast chemical processes are integrated implicitly while the slow chemical processes and transport are integrated explicitly. The slow processes are always carried during the integration of the fast chemistry.

6.3.1 Identification of fast and slow reactions and species

A critical component in the AHI method is to identify fast and slow reactions and species on-the-fly. While CSP, ILDM and other eigen-analyses could be used for fast-slow separation, efficiency is key for on-the-fly identification. An efficient criterion proposed by Lam [37] is used in the present study to define the timescale of a reaction:

$$\tau_i \equiv |\mathbf{J}_i \cdot \boldsymbol{\nu_i}|^{-1},$$

$$\mathbf{J}_i = \frac{\partial \Omega_i}{\partial \boldsymbol{c}} = \left[\frac{\partial \Omega_i}{\partial c_1} \frac{\partial \Omega_i}{\partial c_2} \dots \frac{\partial \Omega_i}{\partial c_k} \dots \frac{\partial \Omega_i}{\partial c_{n_s}}\right], \tag{6-5}$$

$$\boldsymbol{\nu}_i = \left[\nu_{1,i}\ \nu_{2,i}\ \dots \nu_{k,i} \dots \nu_{n_s,i}\right]^{\mathrm{T}},$$

where Ω_i is the net reaction rate for the i^{th} reaction, $\boldsymbol{c}$ is the vector of species mole concentrations, $\nu_{k,i}$ is stoichiometric coefficient of the k^{th} species in the i^{th} reaction, and n_s is the total number of species. The i^{th} reaction is considered fast if

$$\tau_i < \frac{\tau_c}{\beta} \tag{6-6}$$

where τ_c is a threshold timescale which is set equal to the integration time step h in the present study, and β is a safety factor that can be mechanism-dependent. The k^{th} species is considered fast if it contributes significantly to a fast reaction, as determined by

$$\left|\frac{\partial \Omega_i}{\partial c_k}\right| > \beta \tau_c^{-1} \tag{6-7}$$

A value of $\beta = 0.5$ is used in the present study for all the simulations unless otherwise specified.

In the present study, the Jacobian of each reaction in Eqs. (6-5) and (6-7) is evaluated based on analytically derived derivatives to ensure high precision and efficiency for the identification of the fast species and reactions. It is noted that temperature is always treated as a slow variable in the AHI method. To ensure the validity of this treatment, the integration time step must be sufficiently small to explicitly resolve heat release.

6.3.2 A dynamic adaptive method for hybrid integration

At any time instance during the integration, fast species and reactions can be identified based on Eqs. (6-5) to (6-7) using the current solution which can be rewritten as

$$\frac{d\boldsymbol{\Phi}}{dt} = \boldsymbol{S}_f + \mathbf{g}_s, \qquad \boldsymbol{\Phi} = \begin{bmatrix} \boldsymbol{\Phi}_f \\ \boldsymbol{\Phi}_s \end{bmatrix} \tag{6-8}$$

where $\boldsymbol{\Phi}_f$ indicates the vector of variables for the fast species, and $\boldsymbol{\Phi}_s$ includes the slow species and other slow variables, *e.g.* temperature. It is emphasized again that the integration time step must be sufficiently small to resolve the temperature profile such that temperature is always a slow variable to be included in $\boldsymbol{\Phi}_\mathbf{s}$. The source term $\boldsymbol{S}_f$ is the contribution from the fast reactions and $\mathbf{g}_\mathrm{s}$ includes the contributions from both the slow reactions and the transport term, *i.e.*

$$\boldsymbol{S}_f = \sum_{i=1}^{m} \boldsymbol{\nu}_i \Omega_i \tag{6-9}$$

$$\mathbf{g}_s = \sum_{i=m+1}^{n_r} \boldsymbol{\nu}_i \Omega_i + \boldsymbol{M} \tag{6-10}$$

where n_r is the total number of reactions and m is the number of fast reactions, which are always listed before the slow ones.

For numerical integration, Eq. (6-8) can be discretized with a first-order scheme:

$$\frac{\Phi_i^{n+1} - \Phi_i^n}{h} = S_{i,f}(\boldsymbol{\Phi}_f^{n+1}, \boldsymbol{\Phi}_s^n) + g_{i,s}(\boldsymbol{\Phi}_f^n, \boldsymbol{\Phi}_s^n) \tag{6-11}$$

where the superscripts indicate the integration step number, the subscript i indicates the i^{th} entry in $\boldsymbol{\Phi}$, and h is the time step size. It is seen that the contribution from the fast reactions, $\boldsymbol{S}_f$, is evaluated partial-implicitly, while the slow reactions and the transport term in $\mathbf{g}_s$ are evaluated fully explicitly. To integrate Eq. (6-11), $\boldsymbol{\Phi}_f^{n+1}$ is first solved implicitly using the first N_f equations in Eq. (6-11) using the BDF scheme, where N_f is the length of vector $\boldsymbol{\Phi}_f$. The remaining N_s equations in Eq. (6-11), where N_s is the length of $\boldsymbol{\Phi}_s$, are then integrated explicitly using the forward Euler scheme to obtain $\boldsymbol{\Phi}_s^{n+1}$. It is noted that, in rare cases, the criteria in Eqs. (6-6) and (6-7) may result in fast reactions involving no fast species. This will not incur accuracy or stability issues to the method since a reaction can be included in the $\boldsymbol{S}_f$ term whether it is fast or not.

Using the above procedure, the number of variables to be implicitly solved is reduced to the number of fast species, such that the computational cost of AHI can be significantly lower than that of the fully implicit chemistry solvers. In addition, the computational cost is further reduced since only the fast reaction rates need to be re-evaluated during the Newton iterations to solve the equations for the fast species, and there is no need to re-evaluate the slow reaction rates and the transport term during the iterations. As such, the computational cost of AHI is expected to be comparable to, or lower than, that of the operator splitting schemes and other fully implicit chemistry solvers.

6.4 Results and discussion

6.4.1 Accuracy and efficiency of the AHI method

The accuracy of the AHI method is first studied in constant-pressure auto-ignition, for which dependent variables and source terms can be expressed as

$$\boldsymbol{\Phi} = \left[Y_1, Y_2, Y_3, \dots, Y_i, \dots, Y_{n_s}, T\right]^T \tag{6-12}$$

$$S_i(\boldsymbol{\Phi}) = \frac{\dot{m}_i}{\rho}, i = 1,2,3, \dots, n_s; S_{n_s+1}(\boldsymbol{\Phi}) = -\frac{\sum_{i=1,n_s} \dot{m}_i h_i}{\rho c_p}, \dot{m}_i = \omega_i W_i \tag{6-13}$$

$$\boldsymbol{M}(\boldsymbol{\Phi}) = 0 \tag{6-14}$$

where the subscript i indicates the i^{th} species, ρ is density, T is temperature, Y_i, h_i, W_i and ω_i are mass fraction, specific enthalpy, molecular weight and the mole production rate, respectively, and c_p is the mixture averaged specific heat capacity. It is noted that the transport term is trivial for auto-ignition, and operator splitting is not involved in this section for the test of the AHI method unless otherwise specified.

Figure 6-5 shows the numerical solutions of the constant-pressure auto-ignition for a stoichiometric hydrogen/air mixture, calculated with the fully explicit first-order Euler scheme, fully implicit (DASAC), and the AHI method, respectively. In the present work, the relative and absolute error tolerances for DASAC are set as 10^{-8} and 10^{-20}, respectively. The detailed hydrogen/air mechanism by Li et al [124] with 9 species and 21 reactions is adopted. For comparison, the solution from the fully implicit solver is regarded as the exact solution. It is shown that the solution obtained by the AHI method with $h = 10^{-7}\ s$ agrees well with the exact solution, while the explicit solver with a smaller time step $h = 10^{-8}\ s$ diverges when ignition occurs, due to the extremely short timescales emerged near the ignition point as shown in Figure 6-6. It is seen in Figure 6-5 and Figure 6-6 that the divergence occurs shortly after the shortest reaction timescale

becomes smaller than the explicit integration time step, as indicated by the vertical dashed line. Figure 6-6 further shows that the shortest reaction timescale defined in Eq. (6-5) decreases rapidly from longer than 100 ns to shorter than 3 ns after the ignition, where temperature becomes higher than $2000\ K$. As such, the integration time of $h = 10^{-8}\ s$ is not sufficiently small for the explicit integration to be stable.

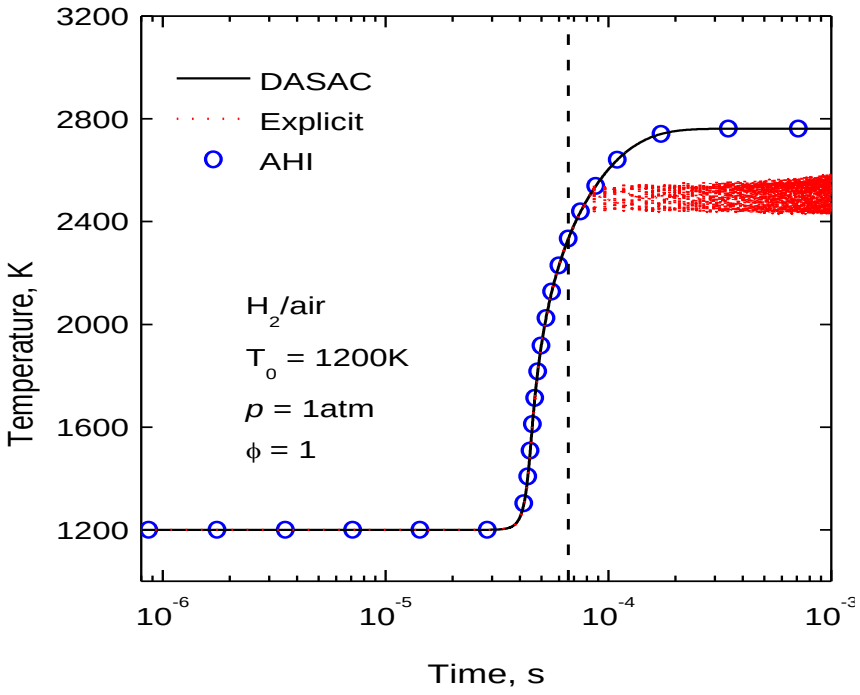

Figure 6-5. Temperature profiles of constant-pressure auto-ignition of hydrogen/air mixture, calculated using the fully implicit solver DASAC (solid line), AHI method with h=10^{-7}s (circles), and explicit first-order Euler scheme with h=10^{-8}s(dots), respectively. The vertical dashed line indicates when the fastest reaction timescale becomes smaller than the explicit integration time step.

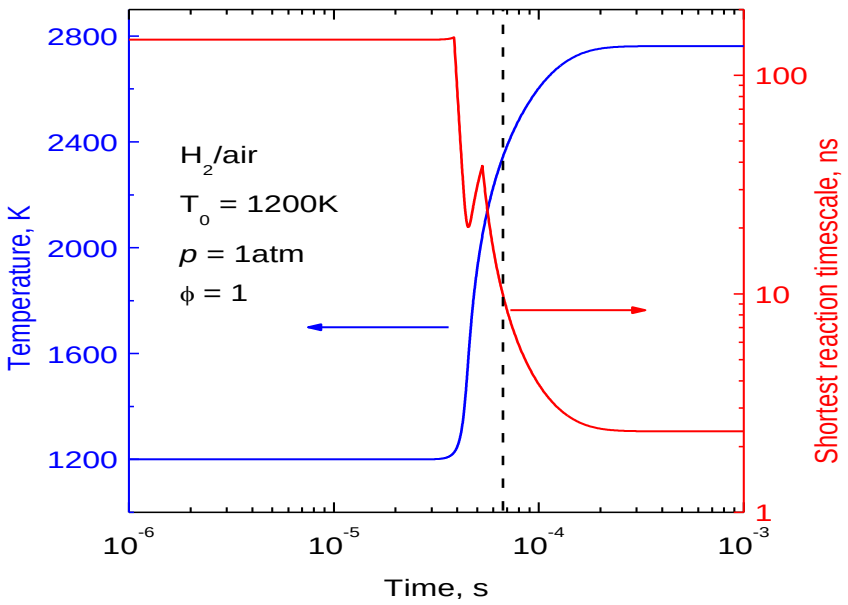

Figure 6-6. The shortest reaction timescale and temperature profile as functions of time for constant-pressure auto-ignition of hydrogen/air. The vertical dashed line indicates when the fastest reaction timescale becomes smaller than the explicit integration time step.

Figure 6-7 further shows the detailed profiles of species mass fractions and the relative errors calculated using Eq. (6-4) in species mass fractions for auto-ignition of hydrogen/air. It is seen that with a fixed time step of $h = 10^{-7}\ s$, the solutions from the AHI method agree well with that from DASAC, including the solutions near the ignition point, where the species mass fractions and temperature change dramatically. The ignition delays of hydrogen/air at different initial temperatures are further computed using DASAC and the AHI method, respectively, as shown in Figure 6-8. It is seen that the results from the AHI method with a fixed time step of $h = 10^{-7}\ s$ are nearly identical to that of DASAC. The accurate and stable solutions by AHI using $h = 10^{-7}\ s$ for the different cases indicate that the fast chemical processes are effectively identified using the criteria in Eqs. (6-5) to (6-7).

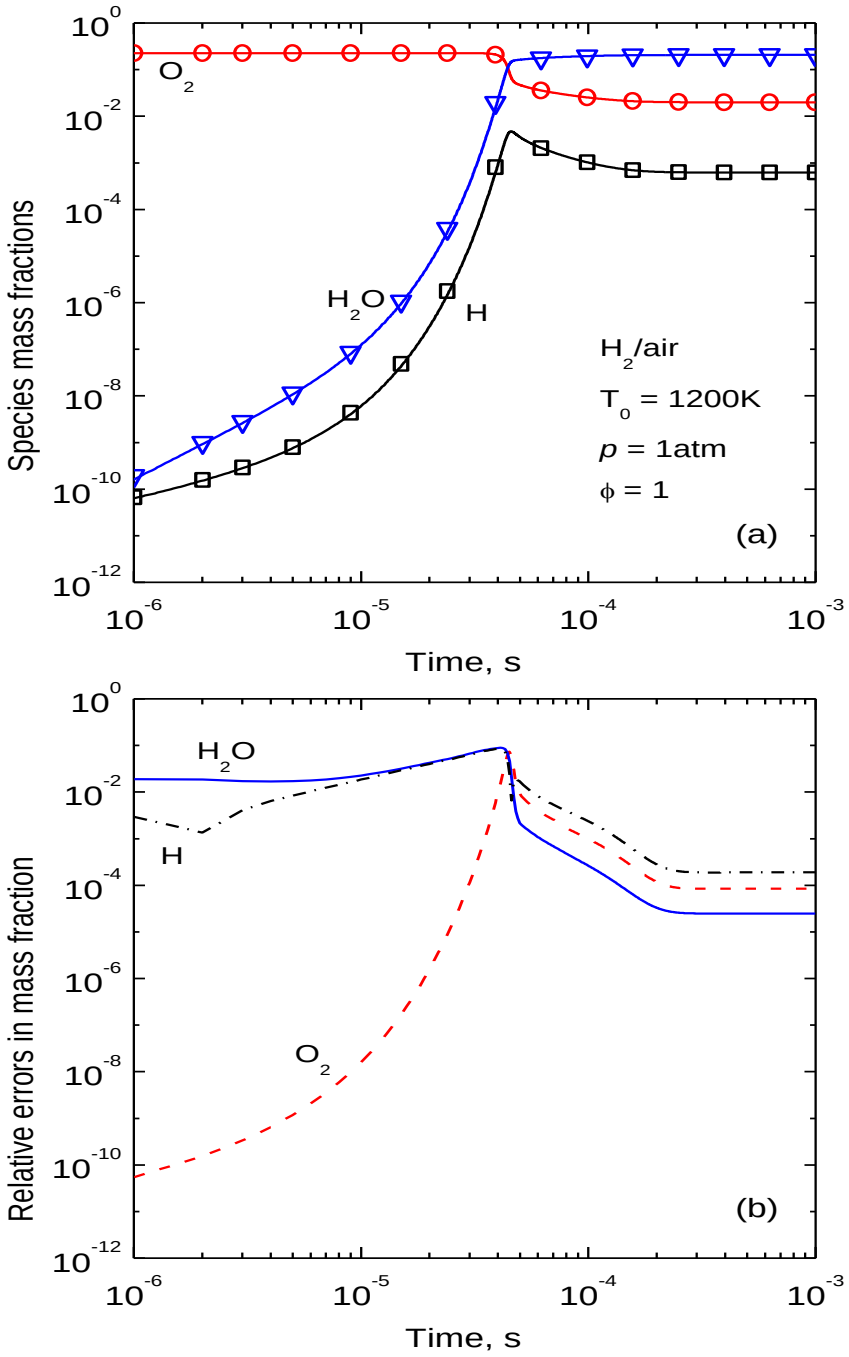

Figure 6-7. (a) Profiles of species mass fractions for constant-pressure auto-ignition of hydrogen/air, calculated using DASAC (solid lines) and the AHI method with h=10^{-7}s (symbols), respectively. (b) Relative errors in species mass fractions between AHI and DASAC.

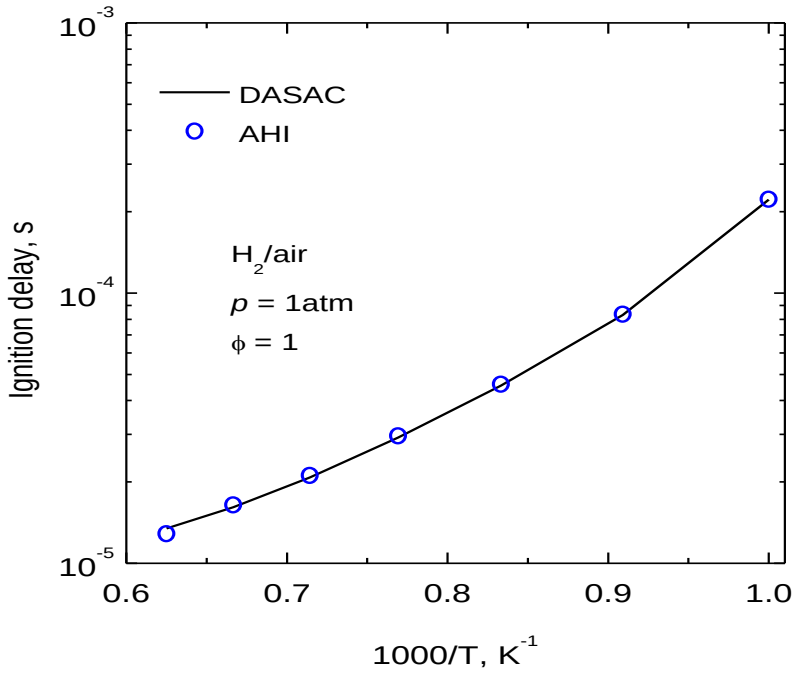

Figure 6-8. Ignition delay of constant-pressure auto-ignition as a function of the initial temperature for hydrogen/air, calculated with DASAC (solid line) and the AHI method with h=10^{-7}s (circles), respectively.

To validate the order of accuracy of the AHI method, the dependence of local relative errors, defined in Eq. (6-4), of the AHI method on the integration time step size is measured for auto-ignition of stoichiometric hydrogen/air at atmospheric pressure, with initial temperature of $T_0 = 1200\ K$. It is noted that in the present error measurements, only one integration step of size h is invoked for each measurement. The integrations for both the AHI method and the exact solution start from the same initial condition, such that the measured error is strictly incurred by the single integration step. Furthermore, to ensure that the change in the measured quantity is not numerically trivial within the integration time step, the measurement is chosen to be made near the ignition point, *i.e.* the inflection point of the temperature profile, where most dramatic changes occur in the variables. The measured relative errors of different variables are plotted in Figure 6-9. It is seen

that the single-step error of the first-order AHI method is of $O(h^2)$, and thus the method is confirmed to be overall first-order in accuracy. It is noted that the construction of higher-order schemes with dynamic adaptive fast-slow separation can be involved and merits further investigation.

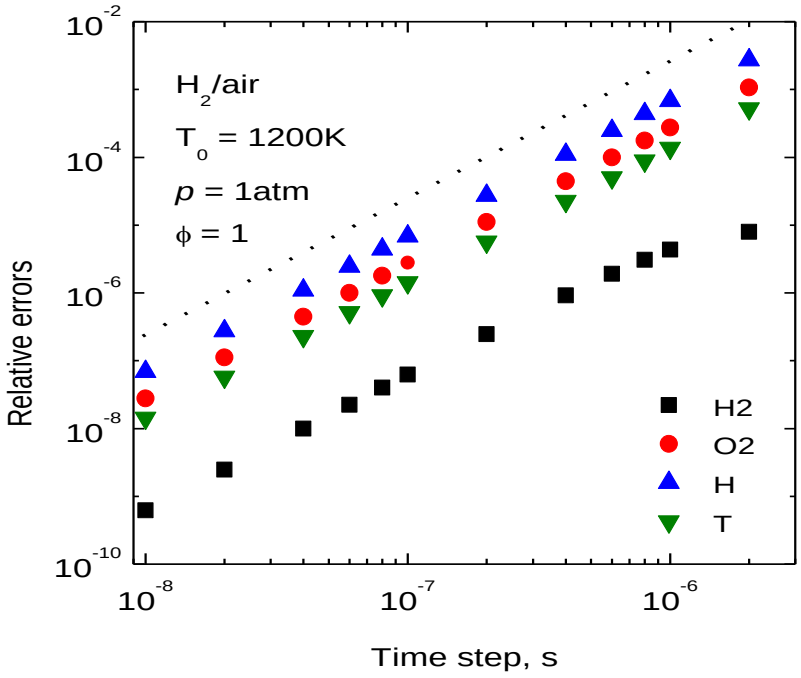

Figure 6-9. Dependence of local relative errors on the integration time step size for constant-pressure auto-ignition of stoichiometric hydrogen/air. Dotted line: trend line with slope of 2. Symbols: measured relative errors.

Compared with fully implicit solvers for chemistry integration, time savings can be achieved by the AHI method by reducing the number of fast variables to be solved implicitly. Figure 6-10(a) shows the number of fast species identified using Eqs. (6-5) to (6-7) at different temperatures in constant-pressure auto-ignition of hydrogen/air, ethylene/air and methane/air mixtures, respectively, at atmospheric pressure and initial temperature of $T_0 = 1200\,K$. The simulations for ethylene/air and methane/air employ a 32-species skeletal mechanism [93] and a

111-species detailed mechanism [86], respectively, to show the fraction of fast variables in typical hydrocarbon flames. It is seen that the number of fast species is significantly smaller than the total number of species at low temperatures before the ignition points for all the cases. Considering that the computational cost of implicit solvers with dense Jacobian operations is a quadratic to cubic function of the number of variables, significant savings in computational cost can be achieved with the AHI method compared with the fully implicit methods when the mechanism is large. Figure 6-10(b) shows the CPU time for the overall simulation of constant pressure auto-ignition without transport and constant pressure unsteady PSR with transport, respectively.

For constant pressure unsteady PSR, the dependent variable list and the source terms for the unsteady PSR can be expressed as

$$\boldsymbol{\Phi} = \left[Y_1, Y_2, Y_3, \dots, Y_i, \dots Y_{n_s}, T\right]^T$$

$$\begin{gathered} S_i(\boldsymbol{\Phi}) = \frac{\dot{m}_i}{\rho}, i = 1,2,3, \dots, n_s, S_{n_s+1}(\boldsymbol{\Phi}) = -\frac{\sum_{i=1,n_s} \dot{m}_i h_i}{\rho c_p}, \dot{m}_i = \omega_i W_i \\ M_i(\boldsymbol{\Phi}) = \frac{Y_i^0 - Y_i}{\tau_{res}}, i = 1,2, \dots, n_s, M_{n_s+1}(\boldsymbol{\Phi}) = \frac{\sum_{i=1,n_s} Y_i^0 (h_i^0 - h_i)}{c_p \tau_{res}} \end{gathered} \tag{6-15}$$

$$\tau_{res} = \frac{\rho V}{\dot{m}_{in}}$$

where the superscript 0 indicates the inlet condition, V is the volume of the reactor, and τ_{res} is the residence time defined based on the inlet mass flow rate $\dot{m}_{in}$.

For the auto-ignition cases, the CPU time of AHI method is normalized by the corresponding CPU time if all the species and reactions are treated implicitly in AHI. For the unsteady PSR cases, the CPU time of AHI method is normalized by the corresponding CPU time of the Strang splitting scheme where the chemistry sub-steps are solved using VODE with

analytical and numerical Jacobian, respectively. It is noted that the AHI method in the present paper always uses analytical Jacobian. The simulation was measured for hydrogen/air, methane/air and ethylene/air at constant atmospheric pressure. The auto-ignition cases were initialized with stoichiometric fuel/air mixtures at $T_0 = 1200\,K$, while the unsteady PSR is initialized with the steady state solution with temperature perturbed by +10 K such that the PSR relaxes toward the steady state solution during the integration. The inlet stream of the PSR consists of fresh stoichiometric fuel/air mixtures at $T_{in} = 300\,K$, and the residence time is $\tau_{res} = 1\,ms$. All the cases are integrated from $t = 0$ to $0.05\,s$ with fixed time steps of $10^{-7}s$, and the system has mostly reached steady state at the end of the integration. β is chosen to be 0.4 for the methane/air case, while the default value of 0.5 was used for the other cases. It is seen that the AHI method achieves approximately 20%, 40%, and 70% time savings for hydrogen, ethylene and methane cases, respectively, for the auto-ignition cases. The time savings are primarily attributed to the reduced number of fast variables that are implicitly solved. In contrast, time savings by factors of 5~10 were achieved for the unsteady PSR cases compared to the splitting scheme using VODE and analytical Jacobian, and even larger time savings were achieved compared to the splitting scheme with Jacobian evaluated through numerical perturbations. The significant time savings for unsteady PSR are primarily attributed to the nontrivial transport term in Eq. (6-15). In the splitting scheme, many integration steps are invoked at the beginning of each chemistry sub-step to revolve the relaxation of the fast chemical modes that are artificially activated when the transport term is switched on or off, as demonstrated in Figure 6-4 for radical *R* in the toy problem, while the AHI method doesn't involve the artificial activation of the fast chemical modes because the transport term is always integrated with chemistry. As such, the current AHI method can be substantially more efficient than the splitting schemes even if adaptive fast chemistry is not used, *i.e.* all the

species and reactions are treated implicitly. The measurement of computational cost was based on numerical codes implemented in FORTRAN and compiled with the Intel FORTRAN Compiler on Intel CPUs.

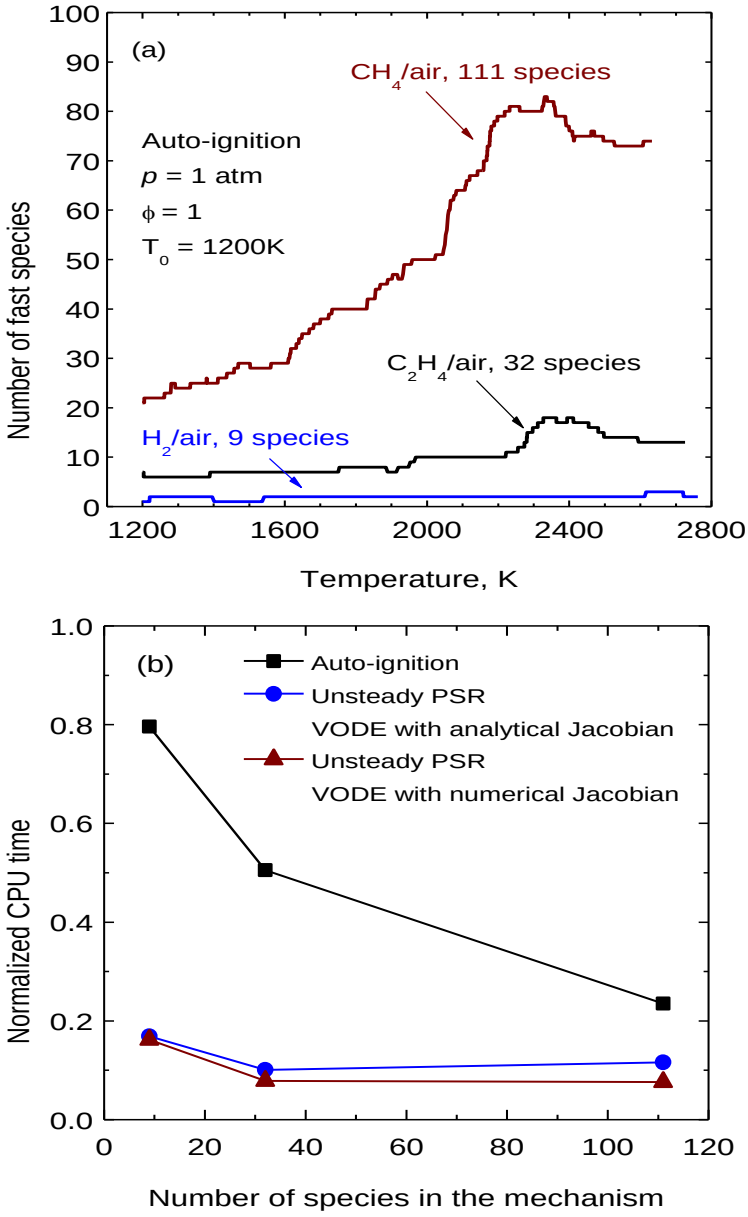

Figure 6-10. (a) Number of fast species in constant-pressure auto-ignition, and (b) CPU time for the integration constant-pressure auto-ignition, normalized by that of fully implicit integration, and

for unsteady PSR, normalized by that of the Strang splitting scheme using VODE, for hydrogen-, ethylene- and methane-air mixtures, respectively, at atmospheric pressure.

6.4.2 Comparisons of the AHI method and the Strang splitting scheme

6.4.2.1 Comparison for the toy problem

The performance of the AHI method is first compared with the operator-splitting scheme for the toy problem. To solve the toy problem with the AHI method, the integration time step sizes are selected such that R_1 and R_3 are slow reactions, and R_2 is a fast reaction. *A*, *B* and *C* are slow species solved explicitly, and *R* is a fast species solved implicitly.

Figure 6-11 shows the solutions from the AHI method and the Strang splitting scheme, respectively, in comparison with the exact solution obtained with a sufficiently small integration time step. A splitting time step of $\Delta t = 10^{-5}$ is used for the splitting scheme, and a time step of $h = 10^{-5}$ is used for AHI. It is observed that the AHI method can accurately solve the case while the Strang splitting scheme results in *O*(1) errors in all the species. Figure 6-12 further shows the relative errors in *B* as functions of the splitting time step Δt for the Strang splitting scheme, and the integration time step *h* for the AHI method, respectively. The relative errors for both methods are measured at time when *A* = 0.5 in the exact solution. The dotted line and the dashed line are the trend lines with slope of 2 for the splitting scheme and slope of 1 for AHI, respectively. It is demonstrated that for the Strang splitting scheme, the point where the method starts to show the desired second-order behavior strongly depends on, and is close to, the timescale of radical *R*. Specifically, in the cases with $\tau = 10^{-8}$ and $\tau = 10^{-6}$, the splitting errors barely decrease until the splitting time step is shorter than approximately 10^{-7} and 10^{-5}, respectively. Note that explicit solvers can be used to integrate the toy problem with a time step close to or shorter than τ. Furthermore, the splitting time step Δt in the Strang splitting scheme is different from the

integration time step h in the AHI method, as each chemistry integration sub-step of the operator-splitting scheme consists of a sequence of fractional implicit integration steps much smaller than Δt. Within each chemistry sub-step, multiple internal implicit integration time steps are typically involved when using stiff ODE solvers to solve the chemistry sub-steps as discussed in the previous section for the unsteady PSR. In comparison, an integration time step in AHI does not consist of any additional sub-step. Therefore, it makes no sense in terms of computational cost to integrate the toy problem using splitting schemes with a splitting time step close to or shorter than τ.

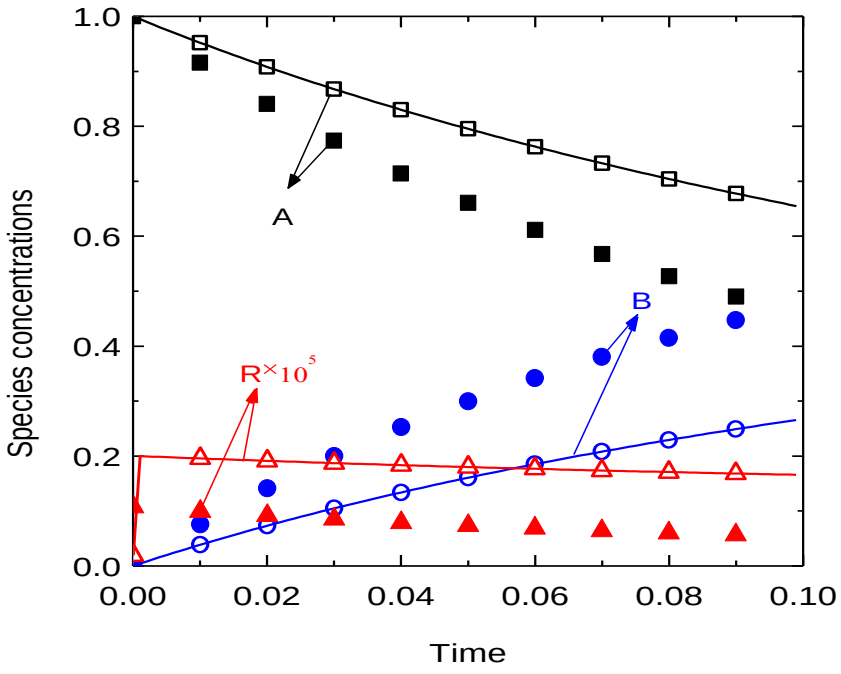

Figure 6-11. Profiles of species concentrations in the toy problem with α=2 and τ=10^{-6}, calculated with the AHI method with h=10^{-5} (open symbols) and the Strang splitting scheme with Δt==10^{-5} (closed symbols), respectively, in comparison with the exact solution (lines).

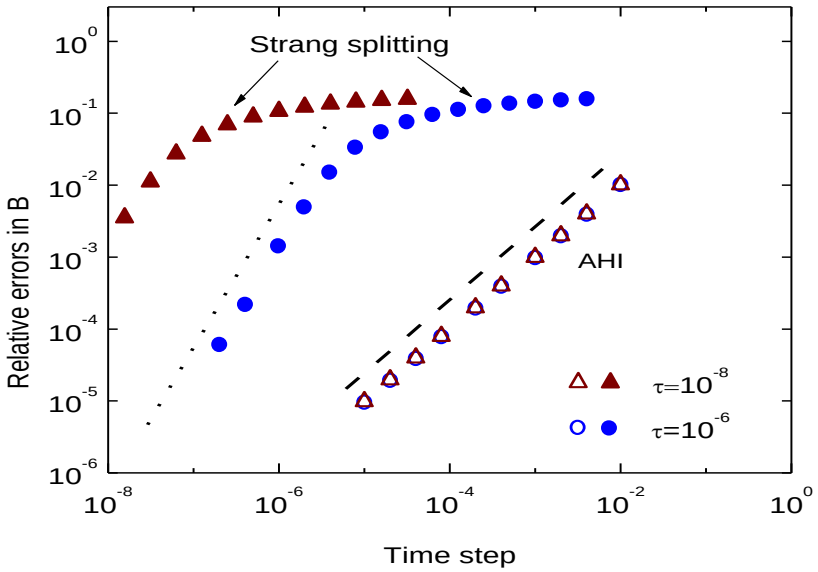

Figure 6-12. Relative errors in B for the toy problem, measured at time when A = 0.5 in the exact solution, as functions of the time step, *i.e.* Δt for the Strang splitting scheme and h for AHI, with α=0.5 for cases with different timescales of R. Closed symbols: Strang splitting scheme. Open symbols: AHI. Triangles: τ=10^{-8}, circles: τ=10^{-6}. The dotted trend line has slope of 2 and the dashed line has slope of 1.

In comparison, the relative errors in B using the AHI method are mostly independent of τ for the two cases, and are smaller than that of the splitting scheme by orders of magnitude at a reasonable time step for implicit solvers, *e.g.* 10^{-2}~10^{-5}, considering that the timescales of the major species are $O(1)$.

6.4.2.2 Comparison for an unsteady PSR

The AHI method is further compared with the Strang splitting scheme with an unsteady PSR of hydrogen/air with significant source of H radical at inlet. The unsteady PSR is initialized with fresh H_2/air mixture at $\phi = 0.3$ and temperature of 875K. The inlet stream consists of fresh H_2/air mixture at $\phi = 0.3$ enriched with 0.1% (in mass) H radical. The inlet condition is time

independent with temperature of $T_{in} = 875\ K$. Pressure of the reactor is fixed at p = 80 atm and residence time is fixed at $\tau_{res} = 2 \times 10^{-6} s$. For integration of the PSR with the Strang splitting scheme, the chemistry sub-step is solved fully implicitly while the transport sub-step is solved explicitly using the second-order Runge-Kutta method. The exact solution is obtained by a fully implicit solver without operator splitting.

Figure 6-13(a) compares the results from the AHI method with $h = 2 \times 10^{-7} s$ and the Strang splitting method with $\Delta t = 2 \times 10^{-7} s$, respectively. It is observed that the mixture ignites approximately at $8\tau_{res}$ as indicated by the exact solution and the solution from AHI, while the Strang splitting scheme predicts an ignition time of approximately $15\tau_{res}$. To further demonstrate the source of the error in the Strang splitting scheme, Figure 6-13(b) shows that the calculated H mass fraction and the normalized contribution of the transport term as a fraction of the creation rate of H radical, F_H, which is expressed as

$$F_H(\mathbf{\Phi}) = M_H(\mathbf{\Phi})/[M_H(\mathbf{\Phi}) + C_H(\mathbf{\Phi})]$$

$$C_H(\mathbf{\Phi}) = \sum_{i=1}^{n_r} (\nu_{H,i}^f \Omega_i^r + \nu_{H,i}^r \Omega_i^f) \tag{6-16}$$

where M_H is the transport term for H radical calculated by Eq. (6-15), C_H is the chemical creation rate of H. The subscript i indicates the i^{th} reaction, $\nu_{H,i}^f$ and $\nu_{H,i}^r$ are the forward and reverse stoichiometric coefficients of H in the i^{th} reaction, respectively, and Ω_i^f and Ω_i^r are the forward and reverse reaction rates, respectively. It is seen that the Strang splitting scheme significantly under-predicts the H mass fraction in the early stage of the ignition, where the contribution of the H radical from the transport term dominates the chemical creation rate, through the same mechanism explained in the toy problem. The large errors in H concentration subsequently propagate to other

quantities and result in significantly delayed ignition. In contrast, H mass fraction is correctly resolved using the AHI method, since the chemical source term and the transport term are integrated together in AHI.

Based on the results for the toy problem and the unsteady PSR for H_2/air, splitting transport from the chemistry integration may result in significant errors in chemistry unless unreasonably small splitting time steps are employed. In this sense transport and stiff chemistry are probably non-splittable in general situations, as nonlinearity and radical transportation are frequently involved in combustion problems.

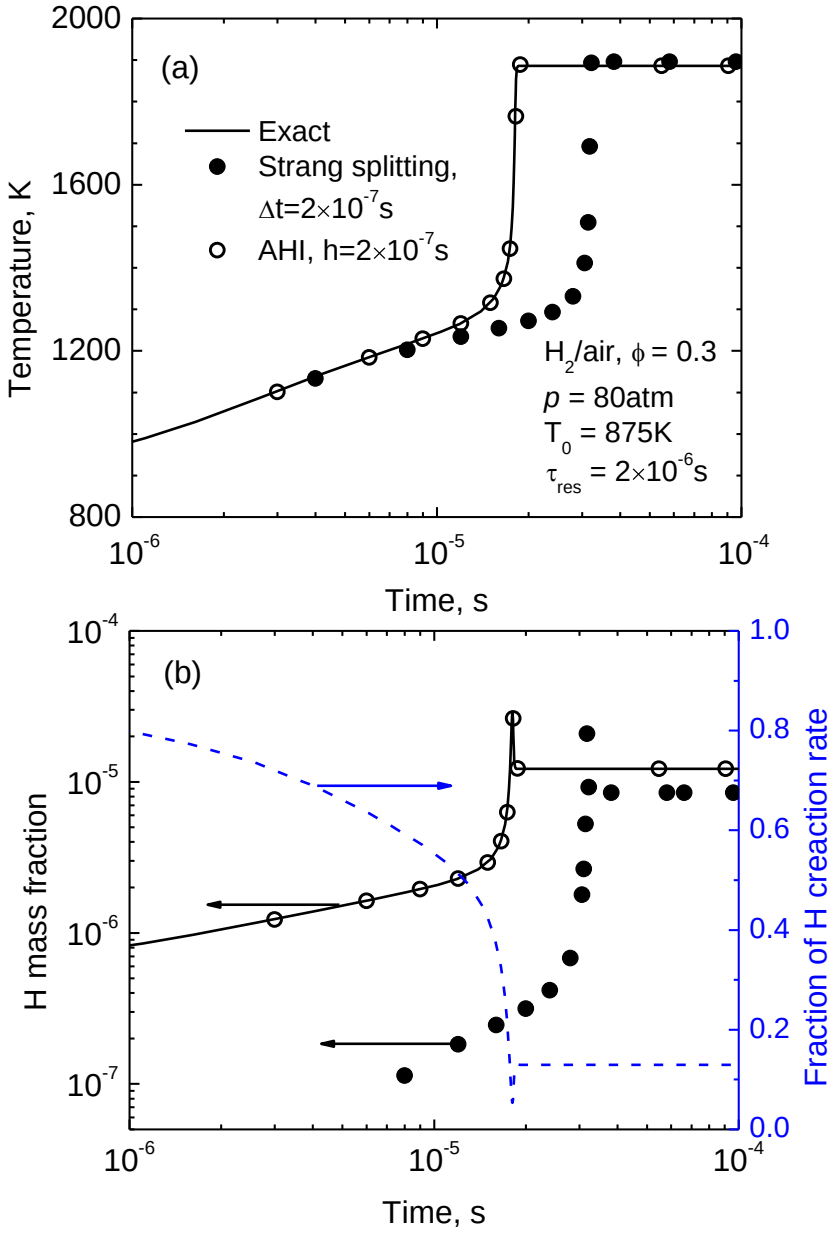

Figure 6-13. (a) Temperature, and (b) mass fraction of H and the fraction of H radical creation rate attributed to transport as functions of time in an unsteady PSR for H_2/air with equivalence ratio of ϕ=0.3. The mixture inlet stream is fresh mixture of H_2/air at ϕ=0.3 and inlet temperature T_{in} = 875 K enriched with 0.1% H radical (in mass).

6.5 Concluding remarks

A failing scenario of the operator splitting schemes is identified and demonstrated with a toy problem. In reacting flows with significant radical sources from the transport term, the operator splitting may incur large errors in the radical concentrations by excluding the transport term in the chemistry integration sub-step. Such errors in the radical concentrations may accumulate and lead to significant errors in major species concentrations and global flame responses, particularly when the chemical creation rates of the radicals are relatively low and strong nonlinearity is present in the radical-controlled reactions. Such a scenario is relevant to practical combustion systems such as premixed flame propagation, where the preheat zone receives a significant amount of radicals from the neighboring reaction zone through back-diffusion.

The AHI method is proposed as a substitute of the operator-splitting schemes to resolve this issue with improved accuracy while at a comparable or lower computational cost. An efficient criterion in the recent CSP literature is employed to define the timescale of reactions and to subsequently separate the fast and slow reactions and species. The fast chemistry is integrated partial-implicitly while the slow processes, including slow chemistry and transport, are integrated explicitly. The accuracy of the AHI method is demonstrated using auto-ignition of hydrogen/air mixtures. The AHI method shows effective first-order error convergence and is stable using dynamic adaptive fast-slow separation.

The accuracies of the AHI method and the Strang splitting scheme are compared for the toy problem and an unsteady PSR with significant H radical source at inlet. The accuracy of the AHI method is significantly higher than that of the Strang splitting scheme for reasonably small to moderately large integration steps, showing that the transport source term should not be excluded

from stiff chemistry integration when strong nonlinearity and significant radical transport are involved.

Chapter 7 Summaries and Future Work

The present dissertation is to address the severe challenges in accommodating the expensive detailed chemistry in large-scale CFD simulations through reduced detailed kinetic models, reduced MAD models, and development of efficient stiff chemistry solvers.

By using a two-stage approach, large detailed reaction models are systematically reduced to obtain CFD-amenable reduced models for a variety of fuels. Specifically, in Chapter 2, a compact 24-species reduced model for *n*-dodecane with lumped fuel cracking steps is developed and extensively validated. The reduced model shows good agreements with the lumped-detailed and detailed models. It is shown that the fast fuel cracking assumption is valid and robust under high-T conditions in laminar flames. To further investigate the fuel cracking behaviors in turbulent flames, a reduced model for *n*-butane is derived from USC Mech II and applied by Sandia in 2-D DNS of a lean turbulent premixed flame. Analysis of the DNS results show that fast fuel cracking assumption remains valid even under intense turbulence conditions. Statistical analysis of the DNS data shows that fuel cracking is complete before the flame zones, and for the conditions tested, turbulent transport does not bring any significant fuel molecules into the flame zones, and thus further substantiates the validity of the fast fuel cracking assumption and the lumping approach.

In Chapter 3, reduced models are developed for selected real jet fuels based on the detailed HyChem models from the Stanford team. Each of the fuel-specific reduced models consists of approximately 30 species. Furthermore, a universal reduced model with 35 species is obtained with programmable fuel thermodynamic and transport properties and fuel cracking reaction parameters. The reduced HyChem models are validated against the detailed models for auto-ignition, PSR, 1-D laminar premixed flame speed, and extinction of 1-D premixed and non-premixed counterflow flames. In addition, important reactions controlling LBO of PSR are

identified through a bifurcation analysis, showing that only the reactions involving small molecules play important roles. Furthermore, the reduced models are shown to well capture the fuel sensitivities.

In Chapter 4, to enable efficient CFD simulations of sooting flames, a 99-species skeletal model and an 86-species reduced model for ethylene/air combustion with PAH formation are developed using sensitivity analysis and LQSSA, starting from a 271-species skeletal model of the KAUST Aramco Mech 1.0, which consists of the PAH chemistry up to A7. The resulting skeletal and reduced models show good agreements with the detailed model in auto-ignition delay, PSR extinction time, and mole fractions of H radical and important PAH species including A1, A4, and A7.

Table 7-1. Summary of reduced kinetic models developed in this study

Key aspects	Fuel	Number of species in reduced model	Number of species in detailed model	Source of detailed model
Jet fuel surrogate	*n*-dodecane	24	123	JetSurF 1.0-l [87]
Small molecule with fuel cracking behaviors	*n*-butane	25	111	USC Mech II [86]
Real jet fuel	A2	31	119	HyChem (Stanford)
	C1	26		
	C5	31		
	Universal for A2/C1/C5	35		
Real jet fuel with NOx chemistry	Universal for A2/C1/C5	45	119 for jet fuel 22 for NOx	Jet fuel chemistry from HyChem (Stanford) NOx chemistry from GRI Mech 3.0 [107] and updated by Luo *et al.* [108]
With PAH chemistry	C_2H_4	86	397	KAUST Aramco PAH Mech 1.0 [118]

In Chapter 5, effects of using detailed and simplified molecular diffusion models on flame propagation and extinction problems are investigated. The unity Lewis number approach is shown to give significant discrepancies compared with the detailed MAD model for some important flame behaviors. To facilitate the application of the MAD model in flame simulations, three new methods are developed to obtain efficient yet accurate reduced MAD models. The reduced MAD models are shown to achieve speedup factors up to about 60 compared with the detailed MAD model for the evaluation of species diffusivities. The reduced MAD models are validated for 1-D laminar flame speed and counterflow extinction calculations, showing excellent agreements with the detailed MAD models. In addition, *a posteriori* validation of species diffusivities using different reduced MAD models is performed using 2-D DNS data of a turbulent premixed *n*-butane/air flame [117]. The worst-case errors in species diffusivities are found to be well controlled by the user-specified error thresholds.

In Chapter 6, the widely-used operator-splitting schemes for integration of stiff chemistry coupled with transport are found to fail in terms of error control, *i.e.* incurring $O(1)$ relative errors, with splitting time steps larger than that required for fully explicit integration, when significant non-chemical radical sources are present. It is shown that, by excluding the transport term from the chemistry integration, errors by orders of magnitude may occur in radical concentrations solved in the chemistry sub-step, resulting in significant errors in the major species. The failing scenario is demonstrated with a toy problem and an unsteady PSR for hydrogen/air with significant H radical concentration at inlet. Motivated by the failing scenario of the operator splitting schemes, a dynamic adaptive method for hybrid integration of stiff chemistry, AHI, is proposed as a substitute of the operator-splitting scheme in such cases. The AHI method can obtain accurate solutions by integrating the fast species and reactions implicitly and the non-stiff terms, including

slow reactions and non-chemical source terms, explicitly. Specifically, fast species and reactions are identified on-the-fly based on their analytically derived timescales, the rates of slow variables are evaluated explicitly and those of fast species are evaluated partial-implicitly. As such, the number of variables to be implicitly solved at each integration time step is reduced to the number of the fast species, resulting in a smaller Jacobian matrix and consequently lower computational cost compared with the fully implicit solvers. The hybrid method is validated in auto-ignition for hydrogen/air with different equivalence ratios and initial temperatures, and compared with the Strang splitting scheme for the toy problem and the unsteady PSR. Results show significant improvement in accuracy using the AHI method.

The present study can be extended in the future in the following aspects. 1) Application of the reduced kinetic models and molecular diffusion models and the AHI solver in high-fidelity CFD simulations. 2) Incorporation of reliable low-temperature pathways and emission sub-models to the reduced HyChem models. 3) Further reduction and/or modeling of the PAH chemistry, as the current reduced models with about 90 species are still large for many CFD simulations. 4) Development of AHI schemes with higher order of accuracy.

References

[1] IEA, *Key world energy statistics*, International Energy Agency, 2016.
[2] T. Lu, C. K. Law, Toward accommodating realistic fuel chemistry in large-scale computations, *Prog. Energy Combust. Sci.* 35 (2) (2009) 192-215.
[3] J. H. Chen, A. Choudhary, B. d. Supinski, M. DeVries, E. R. Hawkes, S. Klasky, W. K. Liao, K. L. Ma, J. Mellor-Crummey, N. Podhorszki, R. Sankaran, S. Shende, C. S. Yoo, Terascale direct numerical simulations of turbulent combustion using S3D, *Computational Science & Discovery* 2 (1) (2009) 015001.
[4] R. B. Bird, W. E. Stewart, E. N. Lightfoot, *Transport Phenomena*, Wiley, New York, 1960.
[5] G. Dixon-Lewis, Flame structure and flame reaction kinetics .2. Transport phenomena in multicomponent systems, *Proceedings of the Royal Society of London Series A-Mathematical and Physical Sciences* 307 (1488) (1968) 111-135.
[6] Y. Xin, W. Liang, W. Liu, T. Lu, C. K. Law, A reduced multicomponent diffusion model, *Combust. Flame* 162 (1) (2015) 68-74.
[7] A. Ern, V. Giovangigli, Fast and Accurate Multicomponent Transport Property Evaluation, *J. Comput. Phys.* 120 (1) (1995) 105-116.
[8] A. Ern, V. Giovangigli, Projected iterative algorithms with application to multicomponent transport, *Linear Algebra and its Applications* 250 (1997) 289-315.
[9] A. Ern, V. Giovangigli, *Multicomponent transport algorithms*, Springer-Verlag Berlin Heidelberg, 1994.
[10] M. D. Smooke, The computation of laminar flames, *Proc. Combust. Inst.* 34 (1) (2013) 65-98.
[11] P. Brown, G. Byrne, A. Hindmarsh, VODE: A Variable-Coefficient ODE Solver, *SIAM J. Sci. Stat. Comp.* 10 (5) (1989) 1038-1051.
[12] M. Caracotsios, W. E. Stewart, Sensitivity analysis of initial value problems with mixed odes and algebraic equations, *Comput. Chem. Eng.* 9 (4) (1985) 359-365.
[13] X. Zheng, T. Lu, C. K. Law, Experimental counterflow ignition temperatures and reaction mechanisms of 1,3-butadiene, *Proc. Combust. Inst.* 31 (2007) 367-375.
[14] A. S. Tomlin, M. J. Pilling, T. Turanyi, J. H. Merkin, J. Brindley, Mechanism reduction for the oscillatory oxidation of hydrogen - sensitivity and quasi-steady-state analyses, *Combust. Flame* 91 (2) (1992) 107-130.
[15] T. Turanyi, Sensitivity analysis of complex kinetic systems - tools and applications, *J. Math. Chem.* 5 (3) (1990) 203-248.
[16] R. Sankaran, E. R. Hawkes, J. H. Chen, T. Lu, C. K. Law, Structure of a spatially developing turbulent lean methane-air Bunsen flame, *Proc. Combust. Inst.* 31 (2007) 1291-1298.
[17] Y. Liu, Y. Wu, Y. Gao, T. Lu, A linearized error propagation model based on Jacobian analysis for skeletal mechanism reduction, in: *9th US National Combustion Meeting, Cincinnati*, 2015.
[18] T. Turanyi, Reduction of large reaction-mechanisms, *New J. Chem.* 14 (11) (1990) 795-803.
[19] T. Lu, C. K. Law, A directed relation graph method for mechanism reduction, *Proc. Combust. Inst.* 30 (2005) 1333-1341.
[20] T. Lu, C. K. Law, Linear time reduction of large kinetic mechanisms with directed relation graph: n-Heptane and iso-octane, *Combust. Flame* 144 (1-2) (2006) 24-36.
[21] T. Lu, C. K. Law, On the applicability of directed relation graphs to the reduction of reaction mechanisms, *Combust. Flame* 146 (3) (2006) 472-483.

[22] T. Lu, C. K. Law, Strategies for mechanism reduction for large hydrocarbons: *n*-heptane, *Combust. Flame* 154 (1-2) (2008) 153-163.
[23] T. Lu, M. Plomer, Z. Luo, S. Sarathy, W. Pitz, S. Som, D. Longman, Directed Relation Graph with Expert Knowledge for Skeletal Mechanism Reduction, in: *7th US National Combustion Meeting*, Atlanta, GA, March 20-23, 2011.
[24] P. Pepiot-Desjardins, H. Pitsch, An efficient error-propagation-based reduction method for large chemical kinetic mechanisms, *Combust. Flame* 154 (1-2) (2008) 67-81.
[25] W. Sun, Z. Chen, X. Gou, Y. Ju, A path flux analysis method for the reduction of detailed chemical kinetic mechanisms, *Combust. Flame* (2010).
[26] Y. Shi, L. Liang, H. W. Ge, R. D. Reitz, Acceleration of the chemistry solver for modeling DI engine combustion using dynamic adaptive chemistry (DAC) schemes, *Combust. Theory Model.* 14 (1) (2010) 69-89.
[27] L. Liang, J. G. Stevens, J. T. Farrell, A dynamic adaptive chemistry scheme for reactive flow computations, *Proc. Combust. Inst.* 32 (1) (2009) 527-534.
[28] Z. Ren, Y. Liu, T. Lu, L. Lu, O. O. Oluwole, G. M. Goldin, The use of dynamic adaptive chemistry and tabulation in reactive flow simulations, *Combust. Flame* 161 (1) (2014) 127-137.
[29] Z. Ren, C. Xu, T. Lu, M. A. Singer, Dynamic adaptive chemistry with operator splitting schemes for reactive flow simulations, *J. Comput. Phys.* 263 (2014) 19-36.
[30] Z. Luo. Development of Reduced Chemical Kinetics for Combustion Simulations with Transportation Fuels. Doctoral Dissertations, University of Connecticut, 2013.
[31] K. E. Niemeyer, C.-J. Sung, M. P. Raju, Skeletal mechanism generation for surrogate fuels using directed relation graph with error propagation and sensitivity analysis, *Combust. Flame* 157 (9) (2010) 1760-1770.
[32] T. Lu, C. K. Law, A criterion based on computational singular perturbation for the identification of quasi steady state species: A reduced mechanism for methane oxidation with NO chemistry, *Combust. Flame* 154 (4) (2008) 761-774.
[33] Z. Ren, S. B. Pope, Entropy production and element conservation in the quasi-steady-state approximation, *Combust. Flame* 137 (1-2) (2004) 251-254.
[34] C. J. Montgomery, C. G. Yang, A. R. Parkinson, J. Y. Chen, Selecting the optimum quasi-steady-state species for reduced chemical kinetic mechanisms using a genetic algorithm, *Combust. Flame* 144 (1-2) (2006) 37-52.
[35] J. D. Ramshaw, Partial chemical equilibrium in fluid dynamics, *Phys. Fluids* 23 (4) (1980) 675-680.
[36] M. Rein, The partial-equilibrium approximation in reacting flows, *Phys. Fluids A* 4 (5) (1992) 873-886.
[37] S. H. Lam, Model reductions with special CSP data, *Combust. Flame* 160 (12) (2013) 2707-2711.
[38] T. Lu, Y. Ju, C. K. Law, Complex CSP for chemistry reduction and analysis, *Combust. Flame* 126 (1-2) (2001) 1445-1455.
[39] S. H. Lam, D. A. Goussis, The CSP method for simplifying kinetics, *Int. J. Chem. Kinet.* 26 (4) (1994) 461-486.
[40] S. H. Lam, Using CSP to understand complex chemical-kinetics, *Combustion Science and Technology* 89 (5-6) (1993) 375-404.
[41] S. H. Lam, D. A. Goussis, Understanding complex chemical kinetics with computational singular perturbation, *Symposium (International) on Combustion* 22 (1) (1989) 931-941.

[42] U. Maas, S. B. Pope, Simplifying chemical-kinetics - intrinsic low-dimensional manifolds in composition space, *Combust. Flame* 88 (3-4) (1992) 239-264.
[43] H. Bongers, J. A. Van Oijen, L. P. H. De Goey, Intrinsic low-dimensional manifold method extended with diffusion, *Proc. Combust. Inst.* 29 (1) (2003) 1371-1378.
[44] Z. Ren, S. B. Pope, The use of slow manifolds in reactive flows, *Combust. Flame* 147 (4) (2006) 243-261.
[45] T. Lu, C. K. Law, Systematic approach to obtain analytic solutions of quasi steady state species in reduced mechanisms, *J. Phys. Chem. A* 110 (49) (2006) 13202-13208.
[46] M. D. Smoke, V. Giovangigli, in: *Lect. Notes Phys.*, M. D. Smooke, (Ed.) Springer Berlin Heidelberg: Berlin, Heidelberg, 1991; Vol. 384, pp 1-28.
[47] E. Giacomazzi, F. R. Picchia, N. Arcidiacono, A review of chemical diffusion: Criticism and limits of simplified methods for diffusion coefficient calculation, *Combust. Theory Model.* 12 (1) (2007) 135-158.
[48] C. K. Law, *Combustion physics*, Cambridge University Press, New York, 2006.
[49] R. Hilbert, F. Tap, H. El-Rabii, D. Thevenin, Impact of detailed chemistry and transport models on turbulent combustion simulations, *Prog. Energy Combust. Sci.* 30 (1) (2004) 61-117.
[50] M. S. Sweeney, S. Hochgreb, M. J. Dunn, R. S. Barlow, The structure of turbulent stratified and premixed methane/air flames II: Swirling flows, *Combust. Flame* 159 (9) (2012) 2912-2929.
[51] M. S. Sweeney, S. Hochgreb, M. J. Dunn, R. S. Barlow, The structure of turbulent stratified and premixed methane/air flames I: Non-swirling flows, *Combust. Flame* 159 (9) (2012) 2896-2911.
[52] R. S. Barlow, M. J. Dunn, M. S. Sweeney, S. Hochgreb, Effects of preferential transport in turbulent bluff-body-stabilized lean premixed CH4/air flames, *Combust. Flame* 159 (8) (2012) 2563-2575.
[53] M. J. Dunn, R. S. Barlow, Effects of preferential transport and strain in bluff body stabilized lean and rich premixed CH4/air flames, *Proc. Combust. Inst.* 34 (1) (2013) 1411-1419.
[54] R. S. Barlow, M. J. Dunn, G. Magnotti, Preferential transport effects in premixed bluff-body stabilized CH4/H2 flames, *Combust. Flame* 162 (3) (2015) 727-735.
[55] C. Bruno, V. Sankaran, H. Kolla, J. H. Chen, Impact of multi-component diffusion in turbulent combustion using direct numerical simulations, *Combust. Flame* 162 (11) (2015) 4313-4330.
[56] V. Nilsen, G. Kosály, Differential diffusion in turbulent reacting flows, *Combust. Flame* 117 (3) (1999) 493-513.
[57] R. J. Kee, G. Dixon-Lewis, J. Warnatz, M. E. Coltrin, J. A. Miller, A Fortran Computer Code Package for the Evaluation of Gas-phase Multicomponent Transport Properties, *Sandia National Laboratories Report SAND86-8246* (1986).
[58] T. Lu, C. K. Law, Diffusion coefficient reduction through species bundling, *Combust. Flame* 148 (3) (2007) 117-126.
[59] M. J. McNenly, R. A. Whitesides, D. L. Flowers, Faster solvers for large kinetic mechanisms using adaptive preconditioners, *Proc. Combust. Inst.* 35 (1) (2015) 581-587.
[60] F. Perini, E. Galligani, R. D. Reitz, A study of direct and Krylov iterative sparse solver techniques to approach linear scaling of the integration of chemical kinetics with detailed combustion mechanisms, *Combust. Flame* 161 (5) (2014) 1180-1195.
[61] F. Perini, E. Galligani, R. D. Reitz, An Analytical Jacobian Approach to Sparse Reaction Kinetics for Computationally Efficient Combustion Modeling with Large Reaction Mechanisms, *Energy Fuels* 26 (8) (2012) 4804-4822.

[62] F. Perini, E. Galligani, G. Cantore, R. D. Reitz, Validation of a Sparse Analytical Jacobian Chemistry Solver for Heavy-Duty Diesel Engine Simulations with Comprehensive Reaction Mechanisms, *SAE Technical Paper 2012-01-1974* (2012).
[63] D. A. Schwer, J. E. Tolsma, W. H. Green, P. I. Barton, On upgrading the numerics in combustion chemistry codes, *Combust. Flame* 128 (3) (2002) 270-291.
[64] C. Xu, Y. Gao, Z. Ren, T. Lu, A sparse stiff chemistry solver based on dynamic adaptive integration for efficient combustion simulations, *Combust. Flame* 172 (2016) 183-193.
[65] U. M. Ascher, S. J. Ruuth, R. J. Spiteri, Implicit-explicit Runge-Kutta methods for time-dependent partial differential equations, *Appl. Numer. Math.* 25 (2–3) (1997) 151-167.
[66] J. Frank, W. Hundsdorfer, J. G. Verwer, On the stability of implicit-explicit linear multistep methods, *Appl. Numer. Math.* 25 (2–3) (1997) 193-205.
[67] U. M. Ascher, S. J. Ruuth, B. T. R. Wetton, Implicit-Explicit Methods for Time-Dependent Partial Differential Equations, *SIAM J. Numer. Anal.* 32 (3) (1995) 797-823.
[68] G. Marchuk, On the theory of the splitting-up method, in: *Proceedings of the 2nd Symposium on Numerical Solution of Partial Differential Equations*, *SVNSPADE*, 1970; pp 469-500.
[69] N. N. Yanenko, in: *The method of fractional steps*, Springer-Verlag: New York, 1971.
[70] O. M. Knio, H. N. Najm, P. S. Wyckoff, A semi-implicit numerical scheme for reacting flow: II. stiff, operator-split formulation, *J. Comput. Phys.* 154 (2) (1999) 428-467.
[71] B. Sportisse, An analysis of operator splitting techniques in the stiff case, *J. Comput. Phys.* 161 (1) (2000) 140-168.
[72] D. A. Schwer, P. Lu, W. H. Green, V. Semiao, A consistent-splitting approach to computing stiff steady-state reacting flows with adaptive chemistry, *Combust. Theory Model.* 7 (2) (2003) 383-399.
[73] D. L. Ropp, J. N. Shadid, C. C. Ober, Studies of the accuracy of time integration methods for reaction–diffusion equations, *J. Comput. Phys.* 194 (2) (2004) 544-574.
[74] M. A. Singer, S. B. Pope, H. N. Najm, Operator-splitting with ISAT to model reacting flow with detailed chemistry, *Combust. Theory Model.* 10 (2) (2006) 199-217.
[75] G. Strang, On the construction and comparison of difference schemes, *SIAM J. Numer. Anal.* 5 (3) (1968) 506-517.
[76] B. Savard, Y. Xuan, B. Bobbitt, G. Blanquart, A computationally-efficient, semi-implicit, iterative method for the time-integration of reacting flows with stiff chemistry, *J. Comput. Phys.* 295 (2015) 740-769.
[77] Y. Gao, R. Xu, H. Wang, T. Lu, Reduced High-Temperature Combustion Chemistry Models of Jet Fuels, in: *6th International Workshop on Model Reduction in Reacting Flows*, Princeton, New Jersey, July 11-14, 2017.
[78] Y. Gao, T. Lu, Reduced HyChem Models for Jet Fuel Combustion, in: *10th U.S. National Combustion Meeting*, College Park, Maryland, April 23-26, 2017; Paper 2RK-0410.
[79] Intergovernmental Panel on Climate Change, Special Report on Renewable Energy Sources and Climate Change Mitigation: Summary for Policymakers and Technical Summary, 2011.
[80] C. K. Westbrook, W. J. Pitz, O. Herbinet, H. J. Curran, E. J. Silke, A comprehensive detailed chemical kinetic reaction mechanism for combustion of n-alkane hydrocarbons from n-octane to n-hexadecane, *Combust. Flame* 156 (1) (2009) 181-199.
[81] S. M. Sarathy, C. K. Westbrook, M. Mehl, W. J. Pitz, C. Togbe, P. Dagaut, H. Wang, M. A. Oehlschlaeger, U. Niemann, K. Seshadri, P. S. Veloo, C. Ji, F. N. Egolfopoulos, T. Lu, Comprehensive chemical kinetic modeling of the oxidation of 2-methylalkanes from C7 to C20, *Combust. Flame* 158 (12) (2011) 2338–2357.

[82] S. M. Sarathy, C. Yeung, C. K. Westbrook, W. J. Pitz, M. Mehl, M. J. Thomson, An experimental and kinetic modeling study of n-octane and 2-methylheptane in an opposed-flow diffusion flame, *Combust. Flame* 158 (7) (2011) 1277-1287.
[83] X. You, F. N. Egolfopoulos, H. Wang, Detailed and simplified kinetic models of *n*-dodecane oxidation: The role of fuel cracking in aliphatic hydrocarbon combustion, *Proc. Combust. Inst.* 32 (1) (2009) 403-410.
[84] D. F. Davidson, S. C. Ranganath, K. Y. Lam, M. Liaw, Z. Hong, R. K. Hanson, Ignition Delay Time Measurements of Normal Alkanes and Simple Oxygenates, *J. Propul. Power* 26 (2) (2010) 280-287.
[85] T. Malewicki, K. Brezinsky, Experimental and modeling study on the pyrolysis and oxidation of n-decane and n-dodecane, *Proc. Combust. Inst.* 34 (1) (2013) 361-368.
[86] H. Wang, X. You, A. V. Joshi, S. G. Davis, A. Laskin, F. N. Egolfopoulos, C. K. Law, USC Mech Version II. High-Temperature Combustion Reaction Model of H_2/CO/C_1-C_4 Compounds. http://ignis.usc.edu/USC_Mech_II.htm, May 2007.
[87] B. Sirjean, E. Dames, D. A. Sheen, H. Wang, JetSurF 1.0-l: Simplified chemical kinetic models for high-temperature oxidation of C_1 to C_{12} *n*-alkanes, in: *6th U.S. National Combustion Meeting*, Ann Arbor, Michigan, May 17-20, 2009, Paper 23.F1.
[88] B. Sirjean, E. Dames, D. A. Sheen, X. Q. You, C. Sung, A. T. Holley, F. N. Egolfopoulos, H. Wang, S. S. Vasu, D. F. Davidson, R. K. Hanson, H. Pitsch, C. T. Bowman, A. Kelley, C. K. Law, W. Tsang, N. P. Cernansky, D. L. Miller, A. Violi, R. P. Lindstedt, A high-temperature chemical kinetic model of *n*-alkane oxidation, JetSurF 1.0, September 15, 2009. http://web.stanford.edu/group/haiwanglab/JetSurF/JetSurF1.0/index.html
[89] S. S. Vasu, D. F. Davidson, Z. Hong, V. Vasudevan, R. K. Hanson, *n*-Dodecane oxidation at high-pressures: Measurements of ignition delay times and OH concentration time-histories, *Proc. Combust. Inst.* 32 (1) (2009) 173-180.
[90] K. Kumar, C.-J. Sung, Laminar flame speeds and extinction limits of preheated *n*-decane/O_2/N_2 and *n*-dodecane/O_2/N_2 mixtures, *Combust. Flame* 151 (1-2) (2007) 209-224.
[91] C. Ji, E. Dames, Y. L. Wang, H. Wang, F. N. Egolfopoulos, Propagation and extinction of premixed C_5-C_{12} *n*-alkane flames, *Combust. Flame* 157 (2) (2010) 277-287.
[92] K. Seshadri, F. A. Williams, Laminar flow between parallel plates with injection of a reactant at high reynolds number, *Int. J. Heat Mass Transfer* 21 (2) (1978) 251-253.
[93] Z. Luo, C. S. Yoo, E. S. Richardson, J. H. Chen, C. K. Law, T. Lu, Chemical explosive mode analysis for a turbulent lifted ethylene jet flame in highly-heated coflow, *Combust. Flame* 159 (1) (2012) 265-274.
[94] C. A. Kennedy, M. H. Carpenter, Several new numerical methods for compressible shear-layer simulations, *Appl. Numer. Math.* 14 (4) (1994) 397-433.
[95] T. Lu, C. K. Law, C. S. Yoo, J. H. Chen, Dynamic stiffness removal for direct numerical simulations, *Combust. Flame* 156 (8) (2009) 1542-1551.
[96] R. J. Kee, F. M. Rupley, E. Meeks, CHEMKIN-III: A Fortran Chemical Kinetic Package for the Anaylsis of Gas-phase Chemical and Plasma Knietics, *Sandia National Laboratories Report SAND96-8216* (1996).
[97] T. Poinsot, D. Veynante, S. Candel, Diagrams of premixed turbulent combustion based on direct simulation, *Symposium (International) on Combustion* 23 (1) (1991) 613-619.
[98] T. Lu, C. S. Yoo, J. H. Chen, C. K. Law, Three-dimensional direct numerical simulation of turbulent lifted hydrogen/air jet flame in heated coflow: A chemical explosive mode analysis, *J. Fluid Mech.* 652 (1) (2010) 45–64.

[99] R. Shan, C. S. Yoo, J. H. Chen, T. Lu, Computational diagnostics for n-heptane flames with chemical explosive mode analysis, *Combust. Flame* 159 (10) (2012) 3119-3127.
[100] R. Xu, H. Wang, D. F. Davidson, R. K. Hanson, C. T. Bowman, F. N. Egolfopoulos, Evidence supporting a simplified approach to modeling high-temperature combustion chemistry, in: *10th U.S. National Combustion Meeting*, Maryland, April 23-26, 2017.
[101] R. Xu, D. Chen, K. Wang, Y. Tao, J. K. Shao, T. Parise, Y. Zhu, S. Wang, R. Zhao, D. J. Lee, F. N. Egolfopoulos, D. F. Davidson, R. K. Hanson, C. T. Bowman, H. Wang, HyChem model: application to petroleum-derived jet fuels, in: *10th U.S. National Combustion Meeting*, Maryland, April 23-26, 2017.
[102] R. Xu, D. Chen, K. Wang, H. Wang, A Comparative Study of Combustion Chemistry of Conventional and Alternative Jet Fuels with Hybrid Chemistry Approach, in: *55th AIAA Aerospace Sciences Meeting*, 2017.
[103] Z. Luo, S. Som, S. M. Sarathy, M. Plomer, W. J. Pitz, D. E. Longman, T. Lu, Development and validation of an *n*-dodecane skeletal mechanism for spray combustion applications, *Combust. Theory Model.* 18 (2) (2014) 187-203.
[104] T. Yao, Y. Pei, B.-J. Zhong, S. Som, T. Lu, K. H. Luo, A compact skeletal mechanism for *n*-dodecane with optimized semi-global low-temperature chemistry for diesel engine simulations, *Fuel* 191 (2017) 339-349.
[105] J. T. Edwards, Reference Jet Fuels for Combustion Testing, in: *55th AIAA Aerospace Sciences Meeting*, Grapevine, Texas, USA, 9-13 January, 2017.
[106] M. B. Colket, J. Heyne, M. Rumizen, J. T. Edwards, M. Gupta, W. M. Roquemore, J. P. Moder, J. M. Tishkoff, C. Li, An Overview of the National Jet Fuels Combustion Program, in: *54th AIAA Aerospace Sciences Meeting*, San Diego, California, USA, 4-8 January, 2016.
[107] G. P. Smith, D. M. Golden, M. Frenklach, N. W. Moriarty, B. Eiteneer, M. Goldenberg, C. T. Bowman, R. K. Hanson, S. Song, W. C. Gardiner, V. V. Lissianski, Z. Qin, http://www.me.berkeley.edu/gri_mech/
[108] Z. Luo, T. Lu, J. Liu, A reduced mechanism for ethylene/methane mixtures with excessive NO enrichment, *Combust. Flame* doi:10.1016/j.combustflame.2010.12.009 (2011).
[109] K. Wang, R. Xu, T. Parise, J. K. Shao, D. J. Lee, A. Movaghar, D. F. Davidson, R. K. Hanson, H. Wang, C. T. Bowman, F. N. Egolfopoulos, Combustion Kinetics of Conventional and Alternative Jet Fuels using a Hybrid Chemistry (HyChem) Approach, in: *10th U.S. National Combustion Meeting*, Maryland, April 23-26, 2017.
[110] A. H. Lefebvre, Fuel Effects on Gas Turbine Combustion—Ignition, Stability, and Combustion Efficiency, *J. Eng. Gas Turb. Power* 107 (1) (1985) 24-37.
[111] L. Esclapez, P. C. Ma, E. Mayhew, R. Xu, S. Stouffer, T. Lee, H. Wang, M. Ihme, Fuel effects on lean blow-out in a realistic gas turbine combustor, *Combust. Flame* 181 (2017) 82-99.
[112] R. D. Stachler, J. S. Heyne, S. Stouffer, J. D. Miller, M. Roquemore, Investigation of Combustion Emissions from Conventional and Alternative Aviation Fuels in a Well-Stirred Reactor, in: *55th AIAA Aerospace Sciences Meeting*, 2017.
[113] M. B. Colket, S. P. Zeppieri, M. D. Smooke, W. W. Kim, Laminar Flame Speeds, Flammability Limits, and Flame/Reaction Zone Thicknesses for a Surrogate Kerosene Fuel at Engine Operating Conditions, in: *50th AIAA Aerospace Sciences Meeting including the New Horizons Forum and Aerospace Exposition*, 2012.
[114] R. Shan, T. Lu, Ignition and extinction in perfectly stirred reactors with detailed chemistry, *Combust. Flame* 159 (6) (2012) 2069-2076.

[115] R. Shan, T. Lu, A bifurcation analysis for limit flame phenomena of DME/air in perfectly stirred reactors, *Combust. Flame* 161 (7) (2014) 1716-1723.
[116] B. J. Magda. Reduced Mechanism Validation and Analysis Near Extinction Limits of Perfectly Stirred Reactors. Master's Theses, University of Connecticut, 2016.
[117] Y. Gao, R. Shan, S. Lyra, C. Li, H. Wang, J. H. Chen, T. Lu, On lumped-reduced reaction model for combustion of liquid fuels, *Combust. Flame* 163 (2016) 437-446.
[118] P. Selvaraj, P. G. Arias, B. J. Lee, H. G. Im, Y. Wang, Y. Gao, S. Park, S. M. Sarathy, T. Lu, S. H. Chung, A computational study of ethylene–air sooting flames: Effects of large polycyclic aromatic hydrocarbons, *Combust. Flame* 163 (2016) 427-436.
[119] W. K. Metcalfe, S. M. Burke, S. S. Ahmed, H. J. Curran, A Hierarchical and Comparative Kinetic Modeling Study of C1−C2 Hydrocarbon and Oxygenated Fuels, *Int. J. Chem. Kinet.* 45 (10) (2013) 638-675.
[120] A. T. Holley, X. Q. You, E. Dames, H. Wang, F. N. Egolfopoulos, Sensitivity of propagation and extinction of large hydrocarbon flames to fuel diffusion, *Proc. Combust. Inst.* 32 (1) (2009) 1157-1163.
[121] C. Liu, R. Zhao, R. Xu, F. N. Egolfopoulos, H. Wang, Binary diffusion coefficients and non-premixed flames extinction of long-chain alkanes, *Proc. Combust. Inst.* 36 (1) (2017) 1523-1530.
[122] R. Speth, W. Green, S. MacNamara, G. Strang, Balanced Splitting and Rebalanced Splitting, *SIAM J. Numer. Anal.* 51 (6) (2013) 3084-3105.
[123] A. E. Lutz, R. J. Kee, J. A. Miller, SENKIN: A Fortran program for predicting homogeneous gas phase chemical kinetics with sensivity analysis, *Technical Report SAND87-8248, Sandia National Laboratories* (1987).
[124] J. Li, Z. W. Zhao, A. Kazakov, F. L. Dryer, An updated comprehensive kinetic model of hydrogen combustion, *Int. J. Chem. Kinet.* 36 (10) (2004) 566-575.

Appendix

A. QSS species for deriving the 24-species reduced model for *n*-dodecane

Index	Species name
1	CH_2
2	CH_2*
3	HCO
4	CH_3O
5	C_2H_3
6	C_2H_5
7	nC_3H_7

B. QSS species for deriving the 25-species reduced model for *n*-butane

Index	Species name
1	CH_2
2	CH_2*
3	HCO
4	CH_3O
5	C_2H_3
6	CH_3CO
7	CH_2CHO
8	nC_3H_7
9	C_4H_7
10	pC_4H_9
11	sC_4H_9

C. QSS species for deriving the 31-species reduced HyChem model for A2

Index	Species name
1	CH_2
2	CH_2*
3	HCO
4	CH_3O
5	C_2H_3
6	C_2H_5
7	HCCO
8	CH_2CHO
9	C_6H_5
10	C_6H_5CO

D. QSS species for deriving the 26-species reduced HyChem model for C1

Index	Species name
1	CH_2
2	CH_2*
3	HCO
4	CH_3O
5	C_2H_3
6	HCCO
7	CH_3CO
8	*i*C_4H_7-1

E. QSS species for deriving the 31-species reduced HyChem model for C5

Index	Species name
1	CH_2
2	CH_2*
3	HCO
4	CH_3O
5	C_2H_3
6	C_2H_5
7	HCCO
8	CH_2CHO
9	C_6H_5
10	C_6H_5CO

F. QSS species for deriving the 35-species universal reduced HyChem model

Index	Species name
1	CH_2
2	CH_2*
3	HCO
4	CH_3O
5	C_2H_3
6	C_2H_5
7	HCCO
8	CH_3CO
9	CH_2CHO
10	iC_3H_7
11	C_6H_5
12	C_6H_5CO
13	iC_4H_7-1

G. QSS species for deriving the 45-species universal reduced HyChem model with NOx

Index	Species name
1	C
2	CH
3	CH_2
4	CH_2*
5	HCO
6	CH_3O
7	C_2H_3
8	HCCO
9	CH_3CO
10	CH_2CHO
11	CH_3CCH2
12	*i*C_3H_7
13	C_6H_5
14	C_6H_5CO
15	*i*C_4H_7-1
16	N
17	NNH
18	H_2CN

H. QSS species for deriving the 86-species reduced model for C_2H_4 with PAH

Index	Species name
1	CH_2OH
2	CH_3O
3	$CH_2(S)$
4	C_2H
5	CH_3CO
6	$C_2H_3O_1$-2
7	NC_3H_7
8	H_2CC
9	$C_5H_5O(2,4)$
10	$A1C_2HC_2H_2$
11	$A1C_2HC_2H_2u$
12	$A1C_2H_4$
13	$A1C_2H_2$